

©2012

Kiran Vyakaranam

ALL RIGHTS RESERVED

**ANALYSIS OF DISPERSIVE MIXING AND BREAKUP OF AIR BUBBLES
DURING CONTINUOUS MIXING OF VISCOUS LIQUIDS USING
EXPERIMENTAL AND NUMERICAL SIMULATION TECHNIQUES**

by

KIRAN VYAKARANAM

A Dissertation submitted to the
Graduate School-New Brunswick
Rutgers, The State University of New Jersey
in partial fulfillment of the requirements

for the degree of

Doctor of Philosophy

Graduate Program in Food Science

written under the direction of

Dr. Jozef L. Kokini

and approved by

New Brunswick, New Jersey

[May, 2012]

ABSTRACT OF THE DISSERTATION

ANALYSIS OF DISPERSIVE MIXING AND BREAKUP OF AIR BUBBLES DURING CONTINUOUS MIXING OF VISCOUS LIQUIDS USING EXPERIMENTAL AND NUMERICAL SIMULATION TECHNIQUES

By KIRAN VYAKARANAM

Dissertation Director:

Dr.Jozef L. Kokini

Air bubble dispersion was studied during continuous mixing of a viscous Newtonian liquid in a Readco[®] 2” twin screw continuous mixer. A detailed review of fundamental bubble and drop breakup theories showed that elongation flows are needed for breakup of drops and bubbles in viscous flows. The velocity profiles and dispersive mixing ability of the twin screw mixer was analyzed using 3D Finite Element Method (FEM) simulations of flow and mixing and air bubble breakup was studied using experimental image analysis methods.

Analysis of the velocity and pressure profiles showed that an introduction of paddle element stagger (forward or reverse) in a limited region of the mixing region caused variations in the local axial velocity. The axial transport happened mostly through the C-shaped region between the paddle elements and the barrel wall in the no stagger configuration and through the intermeshing region between the co-rotating paddle elements in a forward 45° stagger configuration. In case of a reverse 45° stagger

configuration, significant local backflow regions were seen in the intermeshing region. A three region categorization was evident in the distribution of dispersive mixing index, with the highest values (predominantly elongation flow) occurring in the intermeshing region. It is proposed that the elongation flow in the intermeshing region occurred as a result of a squeeze flow created between the moving paddle element surfaces. The introduction of stagger disrupted this effect in and caused elongation flow intensity to be minimal in the intermeshing region.

The measured bubble size distributions showed highest breakup for the no stagger configuration. A maximum stable bubble diameter predicted from local shear rates calculated from the FEM simulations in the mixer correlated well with the experimental mean bubble diameters. Effective shear rates calculated from measured mean bubble diameters were proportional to the mean shear rates calculated by the FEM simulations at various locations in the mixer for all paddle element configurations. This study provides methods to predict the effective shear rate for dispersion of air during continuous mixing of a highly viscous Newtonian liquid that can be applied to complex mixing flows.

ACKNOWLEDGEMENT

I would like to thank my advisor Dr. Jozef Kokini for giving me an opportunity to work in his lab, for his belief in my abilities and for his patience, guidance and support throughout my graduate studies.

I would like to thank Dr. Qingrong Huang, Dr. Michael Rogers and Dr. Alberto Cuitino for being part of my thesis committee.

I would like to extend special thanks to Dr. Kit Yam, Dr. Mukund Karwe, Dr. Richard Ludescher and Dr. Jerry Kukor for guiding me to the finish line.

I would like to thank Dr. Alan Moskowitz and Dr. Navroz Boghani of Kraft Foods for their exceptional support and encouragement through a difficult phase.

I would like to thank all my co-workers and lab mates over the last several years for their support and good times.

Lastly, but definitely not the least, I would like to thank my family and friends who understood me, have stood by me and encouraged me never to give up all along.

TABLE OF CONTENTS

ABSTRACT OF THE DISSERTATION	ii
ACKNOWLEDGEMENT	iv
TABLE OF CONTENTS	v
LIST OF TABLES	vii
LIST OF FIGURES	viii
1. INTRODUCTION	1
1.1 Overview of the research	1
1.2. Hypothesis	3
1.3 Objectives of this research	4
<u>Broad objective:</u>	4
<u>Specific Objectives:</u>	4
2. LITERATURE REVIEW	6
2.1 Origin of the Cellular Structure in Baked and Extruded Foods	6
2.2 Deformation and break up of drops and bubbles in steady flows	19
2.2.1 <i>Governing Equations and Fundamental Theories</i>	20
2.2.2 <i>Measurement of drop deformation</i>	25
2.2.4 <i>Evaluation of drop breakup criteria in steady flows</i>	29
2.3 Deformation and break up of drops and bubbles in complex viscous flows	42
2.4 Numerical Simulation of viscous mixing flows	46
2.4.1 <i>Theoretical measures of mixing</i>	47
2.4.2 <i>Governing equations for calculation of flow</i>	51
2.4.3 <i>Numerical methods for simulation of mixing flows</i>	53
2.5. Recent advances in 3D Numerical simulation of model mixing geometries	57
2.5.1 <i>Stirred tank reactors/batch mixers</i>	58
2.5.2 <i>Dough mixers and kneaders</i>	65
2.5.3 <i>Continuous mixers and extruders</i>	73
3. RESEARCH METHODOLOGY	85
3.1 Experimental materials and methods	85

3.1.1 Readco 2" Continuous Processor	85
3.1.2 Model mixing fluid and material properties	88
3.1.3 Bubble Imaging and Size Measurements	89
3.2 FEM simulation of continuous flow and mixing	92
3.2.1 Construction of the FEM mesh of the Readco mixer for flow simulation	92
3.2.2 FEM flow simulation to obtain flow field and velocities using POLYFLOW	95
3.3 Calculation of dispersion parameters	99
3.3.1 Capillary Numbers (Ca and Ca_{cr})	99
3.3.2 Maximum stable bubble diameters (d_{max})	99
3.3.2 Effective shear rate for dispersion (G_{eff})	100
4. RESULTS AND DISCUSSION	102
4.1 PART I. Evaluation of flow profiles in the Readco continuous mixer	102
4.1.1 Comparison of velocity magnitudes throughout the whole mixer	103
4.1.2 Comparison of local velocity magnitudes over XY planar cross-sections	111
4.2 PART II. Evaluation of dispersive mixing in the Readco continuous mixer	120
4.3 PART III. Evaluation of air bubble dispersion in the Readco continuous mixer	136
4.3.1. Evaluation of local shear rates and capillary number distributions	136
4.3.2 Experimental investigation of bubble breakup	148
4.3.3 Evaluation of maximum stable diameter and effective shear rate for dispersion	154
5. CONCLUSIONS	160
6. REFERENCES	165
APPENDIX	171
VITA	172

LISTS OF TABLES

Table 2.1: Comparison of values of flow type parameter, α and mixing index, λ_{MZ}

Table 3.1: Material properties and operating parameters for air dispersion during mixing in the Readco® continuous processor

Table 4.1 Maximum and minimum values of total velocity magnitude (V) and V_x , V_y and V_z calculated at all points in the entire mixer volume for one complete revolution of the three paddle elements (FLAT, 45F and 45R).

Table 4.2 Average values of shear rate and dispersive mixing index λ_{MZ} , cumulated over nine time steps for the entire mixer volume and specific X-Y cross sectional planes for a screw speed of 100 RPM

Table 4.3 Mean shear rate values calculated over cross-sectional planes at different locations in the mixer for the three paddle element configurations at 100 RPM and 55 RPM

Table 4.4 Distribution parameters for normal distribution fits in Figure 4.26.

LIST OF ILLUSTRATIONS

Figure 2.1: Schematic diagram showing the minimum work required for a bubble to reach a critical size (Blander and Katz, 1975)

Figure 2.2: Wetting angle θ for a gas bubble at the interface of a solid particle during heterogeneous nucleation (Colton and Suh, 1987).

Figure 2.3 Effect of material rheology and vapor pressure on extrudate expansion (Chang, 1992).

Figure 2.4 Effect of melt viscosity and moisture content on extrudate expansion of high amylopectin starch (Chang, 1992).

Figure 2.5: Porosity versus barrel fill for corn starch, as well as native and pregelatinized amylopectin (Cisneros and Kokini, 2002).

Figure 2.6. a.) Porosity and b.) Cell Density of starch extrudates before and after microwave expansion (Cisneros and Kokini, 2002).

Figure 2.7 Disentrainment coefficient k calculated as the negative of the slope of the plot (Campbell and Shah, 1998).

Figure 2.8: Diagram showing the properties of the continuous and discontinuous media and the interface of the drop (Risso, 2000).

Figure 2.9 Measurement of parameters for drop deformation (Bentley and Leal, 1986) .

Figure 2.10 (a) Couette apparatus (Grace, 1982), (b) parallel band apparatus (Rust and Manga, 2002), and (c) Four-roll mill apparatus (Grace, 1982).

Figure 2.11 Streamlines of flow for varying values of α (Bentley and Leal, 1986).

Figure 2.12 C_{acr} as a function of the viscosity ratio, p for rotational and irrotational flows Grace (1982).

Figure 2.13 Experimental measurements of C_{acr} for $\alpha = 0.2, 0.4, 0.6, 0.8$ and 1.0 . open symbols – experiments ; solid lines – small deformation theory; broken lines – large deformation theory (Bentley and Leal, 1986) .

Figure 2.14 Numerical estimates of C_{acr} – comparison with experiments of Bentley and Leal (1986), Khakhar and Ottino (1986). Note: usage of ψ in place of α

Figure 2.15 Numerical estimates of C_{acr} – comparison with experiments of Grace (1982), Khakhar and Ottino (1986). Note: usage of ψ in place of α

Figure 2.17 Comparison of C_{acr} vs p in simple shear and pure elongation flows from experimental and numerical studies (Meijer and Janssen, 1994).

Figure 2.13 (a) Deformation parameter, D and (b) Dimensionless extension ratio, L/a as a function of Ca for air bubbles in simple shear flow (Muller-Fischer et al., 2008).

Figure 2.14 C_{acr} for bubble breakup in simple shear flow obtained in a concentric cylinder device (Muller-Fischer et al., 2008). Data for air bubbles (Muller-Fischer et al., 2008) compared with data for droplets (Grace, 1982).

Figure 2.15 Critical Capillary Number vs viscosity ratio for a non-Newtonian drop in extensional flow (Favelukis et al., 2005).

Figure 2.16 comparison of effective shear rates for drop dispersion at low and high viscosity ratios in a Kenics static mixer (Grace, 1982).

Figure 2.17: Correlation between dimensionless drop diameter and viscosity number for dispersion in SMX static mixer at low Reynolds number flow (Das et al., 2005).

Figure 2.18 Examples of impeller designs in batch mixers (a) Three-Rushton turbine (Zalc et al., 2001) (b) Paravisc impeller (Iranshahi et al., 2006) (c) Rushton turbine with a co-axial anchor (Rivera et al., 2006).

Figure 2.19 Comparison of experimental and simulated results show excellent agreement in revealing the mixing patterns in a three turbine Rushton impeller mixer after 600 revolutions at (a) $Re = 20$ and (b) $Re = 40$ (Zalc et al., 2002).

Figure 2.20 Contour plots of $\ln(\lambda)$ reveal the spatial heterogeneity of stretching at various impeller speeds (a) $Re = 20$ (b) $Re = 40$ (c) $Re = 160$ (Zalc et al., 2002).

Figure 2.21 Intensity of segregation vs. time for different Re and points of injection of the tracer (Iranshahi et al., 2006).

Figure 2.22 Distributive mixing in a rushton turbine impeller with a co-axial anchor (a) co-rotating after 15s (b) co-rotating after 150s (c) counter-rotating after 15s (d) counter-rotating after 150s (Rivera et al., 2006).

Figure 2.23 Dough kneaders of various geometries (a) Farinograph (b) Do-corder (c) Mixograph (d) Spiral mixer (Jongen et al., 2003) .

Figure 2.24 (a) Cumulative distribution of mean flow type parameter, D for various kneader geometries (b) Cumulative distribution of mean flow type parameter, D for a farinograph at different blade configurations and speed (Jongen et al., 2003).

Figure 2.25 Effect of fluid rheology on the velocity profiles in the vertical center plane of the Farinograph(Connelly and Kokini, 2006).

Figure 2.26 Density of probability of the length of stretch, $\ln(\lambda)$ experienced by 10,000 infinitesimal material lines in the farinograph (Connelly and Kokini, 2006).

Figure 2.27 Shear stress (g/cm²) contour maps for fluid with relaxation times (a) 0s and (b) 100s in a 2D single paddle mixer (Connelly and Kokini, 2003).

Figure 2.28. Volumetric distributions of λ MZ and shear stress for (a) conveying elements and (b) shearing discs in a twin screw extruder (Li and Manas - Zloczower, 1994).

Figure 2.29 Distribution of the area stretch in the mixing region of a co-rotating twin-screw extruder for different widths of the kneading discs (Ishikawa et al., 2001).

Figure 2.30 (a) Residence Time Distribution and (b) Mean nearest distance between markers in the mixing region of a co-rotating extruder fitted with three-lobed kneading discs (Yoshinaga et al., 2000).

Figure 2.31 Kneading elements of the Readco ® twin-screw processor (Readco Inc, York, PA) arranged in (a) FLAT (b) 45F and (c) 45R configurations.

Figure 2.32 Mixing Index (λ MZ) contours for the (a) single screw and twin-screw mixers after (b) 45° (c) 67.5° and (d) 90° rotation of the paddles (Connelly and Kokini, 2007).

Figure 2.33 Comparison of cluster distribution index for 10 revolutions of the single screw and twin screw mixers with different location of the initial cluster in the flow domain – b1 (center location) and b2 (leftmost location) in the flow domain (Connelly and Kokini, 2007) .

Figure 2.34 Effect of (a) screw speed and (b) screw configuration on the time-averaged mixing efficiency of the Readco® twin-screw continuous and the Farinograph batch mixers (Ashokan, 2008).

Figure 3.1. The Readco ® 2" Continuous Processor (Twin-screw mixer) fitted with a transparent Plexiglas barrel.

Figure 3.2 Conveying screw elements and mixing paddle elements of the Readco ® twin screw mixer without the barrel.

Figure 3.3 Schematic of sample paddle element configurations in the mixing region of the Readco processor. (a) Flat - all paddle elements parallel to each other, (b) 45F - three centre paddle elements in a forward stagger of 45° (c) 45R - three centre paddle elements in a reverse stagger of 45° .

Figure 3.4 Schematic of arrangement for image capture of bubbles in the mixer against backlighting.

Figure 3.5 (a) 3D single paddle mesh with a total of 432 X 3 mesh elements 3(b) 3D three paddle mesh with a total of 432 X 5 mesh elements (c) Radial mesh of the XY cross-section of the barrel volume with a total of 1072 elements (d) Barrel volume mesh (e) Axial profile of the barrel volume mesh (Vyakaranamet al., 2012).

Fig 3.6 Steps involved in solving a flow simulation task (Polyflow ® User Guide, Fluent Inc., Lebanon, NH).

Figure 3.7 FEM simulation mesh of the mixing region showing the inflow and outflow boundary planes.

Figure 3.8 Angular positions of the mixer paddle elements after, a) 0° rotation, b) 30° rotation, c) 60° rotation.

Fig 3.9 Steps involved in solving a mixing simulation task (Polyflow ® User Guide, Fluent Inc., Lebanon, NH).

Figure 4.1 Experimental mass flow rate of Globe ® Corn Syrup 042110 measured in the Readco® 2” continuous processor as a function of screw speed and paddle element configuration.

Figure 4.2 Velocity vector maps for the FLAT configuration at (a) time step 1, 10° rotation (b) time step 4, 40° rotation and (c) time step 9, 90° rotation.

Figure 4.3 Velocity vector maps for the 45F configuration at (a) time step 1, 10° rotation (b) time step 4, 40° rotation and (c) time step 9, 90° rotation

Figure 4.4 Velocity vector maps for the 45R configuration at (a) time step 1, 10° rotation (b) time step 4, 40° rotation and (c) time step 9, 90° rotation.

Figure 4.5: Pressure contours over $x=0$ and $y=0$ cross-sectional planes in the FLAT configuration at (a) Legend (b) time step 1, (c) time step 4, (d) time step 9, (e) time step 10, (f) 45F configuration at time step 4 and (g) 45R configuration at time step 4.

Figure 4.6 Contour maps of V_x at P4 and time step 4 (a) Legend (b) FLAT (c) 45F and (d) 45R configurations.

Figure 4.7 Contour maps of V_y at P4 and time step 4 for (b) FLAT (c) 45F and (d) 45R configurations.

Figure 4.8: Contour maps of axial velocity (V_z) at P4 in the FLAT configuration (a) time step 1, 10° rotation (b) time step 4, 40° rotation and (c) time step 9, 90° rotation.

Figure 4.9: Contour maps of axial velocity (V_z) at P4 in the 45F configuration (a) time step 1, 10° rotation (b) time step 4, 40° rotation and (c) time step 9, 90° rotation.

Figure 4.10: Contour maps of axial velocity (V_z) at P4 in the 45R configuration (a) time step 1, 10° rotation (b) time step 4, 40° rotation and (c) time step 9, 90° rotation.

Figure 4.11: Axial velocity (V_z) along a line running through the nip region of the mixer (a) FLAT (b) 45F and (c) 45R configuration.

Figure 4.12 Contour maps of shear rate over XY cross-sectional planes at the 4th paddle element (P4) for FLAT configuration at 100 RPM (a) time step 1(b) time step 4 (c) time step 9 (d) Legend.

Figure 4.13 Contour maps of dispersive mixing index λ_{MZ} , over XY cross-sectional planes at the 4th paddle element (P4) for FLAT configuration at 100 RPM (a) time step 1(b) time step 4 (c) time step 9. Legend – yellow to red shades show predominantly elongation flow, green shades are predominantly shear and blue shades are predominantly rotation.

Figure 4.14 Contour maps of dispersive mixing index λ_{MZ} , over three XY cross-sectional planes at time step 4 for FLAT configuration at 100 RPM (a) P1(b) P4 (c) P8 . Legend – yellow to red shades show predominantly elongation flow, green shades are predominantly shear and blue shades are predominantly rotation.

Figure 4.15 Contour maps of dispersive mixing index λ_{MZ} , over three XY cross-sectional planes at time step 4 for 45F configuration at 100 RPM (a) P1(b) P4 (c) P8 . Legend – yellow to red shades show predominantly elongation flow, green shades are predominantly shear and blue shades are predominantly rotation.

Figure 4.16 Contour maps of dispersive mixing index λ_{MZ} , over three XY cross-sectional planes at time step 4 for 45R configuration at 100 RPM (a) P1(b) P4 (c) P8 .Legend – yellow to red shades show predominantly elongation flow, green shades are predominantly shear and blue shades are predominantly rotation.

Figure 4.17 Illustration of ‘Squeeze flow’ in the intermeshing region between the paddle element surfaces and barrel wall surfaces causing a predominantly elongation flow.

Legend – yellow to red shades show predominantly elongation flow, green shades are predominantly shear and blue shades are predominantly rotation.

Figure 4.18 Dispersive mixing in the mixer volume at time step 4 shown by colour coding the velocity vectors with the magnitude of dispersive mixing index λ_{MZ} , at 100 RPM (a) FLAT(b) 45F (c) 45R (d) Legend – yellow to red shades show predominantly elongation flow, green shades are predominantly shear and blue shades are predominantly rotation.

Figure 4.19 Magnitudes of dispersive mixing index λ_{MZ} , along a line connecting P1 (0, 0.8, 0) to P2 (0, 0.8, 13.8) at 100 RPM (a) FLAT (b) 45F (c) 45R

Figure 4.20 Density of elongation flow in the mixer volume as a function of paddle configuration and screw speed.

Figure 4.21 Distribution of local shear rate and dispersive mixing index for the three screw configurations at 100 RPM cumulated over 9 time steps over XY cross-sections (a) FLAT P1 (b) 45F P1 (c) 45R P1 (d) FLAT P4 (e) 45F P4 (f) 45R P4 (g) FLAT P8 (h) 45F P8 (i) 45R P8.

Figure 4.22 Mean Ca calculated for bubble diameters ranging from 100 μm to 1200 μm for the three paddle element configurations compared with the Ca_{cr} values for predominantly shear, predominantly elongation and mixed flows from literature at (a) P1 ($z = 1.27\text{cm}$) (b) P4 ($z = 5.15\text{ cm}$) and (c) P8 ($z = 10.46\text{ cm}$).

Figure 4.23: Distribution of local shear rate and dispersive mixing index for the three screw configurations at 100RPM calculated for points on 100 random particle trajectories at XY cross-sectional planes at P1, P4 and P8 (a) FLAT P1 (b) 45F P1 (c) 45R P1 (d) Distribution of density of points $\lambda_{MZ} > 0.6$ in the three paddle element configurations at

100RPM for points on 100 random particle trajectories at XY cross-sectional planes at P1, P4 and P8.

Figure 4.24 High speed images of bubbles at various locations in the mixer during mixing at (a), (b) 100 RPM and (c), (d) 55 RPM at the P4 and feed screw locations.

Figure 4.25 Bubble images taken along the mixer length for FLAT configuration (a) P4 at 100 RPM (b) P4 at 55 RPM taken while the mixer was running and (c) P1 at 100 RPM (b) P4 at 100 RPM and (c) P8 at 100 RPM taken after the mixer was stopped.

Figure 4.26 Bubble size distributions taken (a) outside the mixer for the three paddle element configurations at 100 RPM; (b) at P1 and P8 inside the mixer at 100 RPM; (c) at P1 and P8 inside the mixer at 55 RPM.

Figure 4.27 Confidence bounds at 95% level for the normal distribution fits outside the mixer for (a) FLAT (b) 45F and (c) 45R paddle element configurations.

Figure 4.27 Confidence bounds at 95% level for the normal distribution fits outside the mixer for (a) FLAT (b) 45F and (c) 45R paddle element configurations.

Figure 4.28 Distribution of theoretical maximum stable diameter, d_{max} over points on trajectories on XY cross-sectional planes at the beginning (P1) and end (P8) of the mixing region for three paddle configurations at 100 RPM

Figure 4.29 Comparison of mean experimental bubble diameters vs. simulated maximum stable bubble diameters for all the paddle configurations as a function of dispersive mixing index.

Figure 4.30 Comparison of effective shear rate vs. simulated mean shear rates for all the paddle configurations as a function of screw speed.

1. INTRODUCTION

1.1 Overview of the research

Air bubbles play a crucial role in several product applications and processes in the food and chemical industry, including multiphase fluid transport and pumping, aerosol and emulsion manufacturing, atomization of liquid, aeration and mixing of viscous fluid materials and extrusion of polymeric materials. Specifically aeration during mixing of dough and extrusion of polymeric materials results in the porous structure of some finished cereal products. For example, the crisp texture of baked and extruded cereal and other starchy foods is a result of their expanded structure, making them more appetizing and palatable, significantly enhancing their value. The expansion of the product is a result of air incorporated and trapped in the starchy polymer dough/melt, and the size distribution of air/gas bubbles and is directly related to the product texture. The mechanisms by which bubbles are entrapped or nucleated and broken up during processing provides the knowledge on how to optimize processing parameters in order to get a desired textural change in the final product. These mechanisms include entrainment, and disentrainment of air, bubble break-up, and coalescence and normal stress compression in viscoelastic materials. While the first two mechanisms determine the total air content in the material, the breakup and coalescence influence the size distribution of the air bubbles (Campbell and Shah, 1988; Campbell et al, 1998; Cisneros and Kokini, 2002). One important application of this research is understanding aeration and

improving the dispersion efficiency during mixing of highly viscous materials undergoing laminar flow.

Flow induced bubble and drop deformation and break up has been well studied in simple model flows with fluids covering a broad range of rheological properties. These studies have correlated the deformation and break up of drops and bubbles in well defined simple flows ranging from simple shear to pure elongation (Acrivos, 1983; Khakhar and Ottino, 1986). In commercial mixing devices, the flow is complex and is often a mixture of various flow types ranging from pure rotation to pure shear to pure elongation. Bubble and drop breakup has also been studied in mixed shear and elongation flows as well as more complex dispersing flows in a static mixer (Grace, 1982; Bentley and Leal, 1986; Das et al., 2005; Megias-Alguacil and Windhab, 2006). For a given dispersion process, knowledge of the dispersed phase size distribution and the dominant flow type (simple shear or pure elongation) leads to estimation of the effective flow strength calculation for of dispersion.

While flow and mixing has been extensively studied in extruders, our group is the first to focus on the analysis of flow or dispersive mixing in continuous mixers. Although similar in design to the twin-screw extruder, the continuous mixer is fundamentally different in terms of (i) larger dimensions and greater barrel and flow channel volume (ii) negligible axial pressure gradient and absence of constrained die at discharge end. Further, no attempts have been made to relate the dispersive mixing ability of a continuous mixer to measured drop or bubble elongation and breakup.

In this study we apply the flow induced bubble break up theories while analyzing the breakup of bubbles during continuous mixing of a medium viscosity Newtonian

liquid consisting of corn syrup. Full 3D finite element method (FEM) simulations will be used to simulate flow in the Readco co-rotating twin-screw mixer which we use as a model for a pilot size mixer and analyze the effect of paddle element stagger on the global and local flow profiles during continuous mixing of a viscous Newtonian corn syrup. FEM simulations are also utilized to analyze the dispersive mixing ability of the continuous twin screw mixer by calculating the local and global distribution of shear rates (flow strength) and the theoretical dispersive mixing index (flow type) as a function of paddle element stagger. Finally, we use the theoretical critical capillary number correlations and the simulated dispersive mixing flow parameters to calculate the maximum stable diameters and effective shear rate for dispersion and compare the predictions with experimentally measured bubble size data in a model Newtonian fluid..

1.2. Hypothesis

- The deformation and breakup of bubbles during continuous mixing of viscous fluids in a twin screw geometry is a function of the distribution of shear and elongational flow.
- The effective flow strength for breakup and the maximum stable bubble diameter that can withstand breakup can be predicted from an analysis of the magnitude and distribution of Mixing Index (flow type) and the Capillary Numbers (flow strength) in the mixer

1.3 Objectives of this research

Broad objective:

The overall objective of the proposed research is to create quantitative predictors for air bubble breakup processes in continuous mixing of viscous fluids by combining the knowledge of fundamental bubble breakup theories and accurate analysis of flow field in the mixer.

Specific Objectives:

1. Evaluate local velocity profiles during mixing of a viscous Newtonian liquid in the Readco[®] co-rotating twin screw continuous mixer as a function of paddle element stagger using 3D finite element method numerical simulations.
2. Evaluate local shear rates and dispersive mixing profiles during mixing of a viscous Newtonian liquid in the Readco[®] co-rotating twin screw continuous mixer as a function of paddle element stagger using 3D finite element method numerical simulations and predict local maximum stable diameters from theoretical critical Capillary Numbers and simulated local shear rates and dispersive mixing indices
3. Demonstrate experimentally using flow imaging techniques and measurements of size distribution obtained through controlled experiments the elongation and breakup of bubbles in the twin screw mixer of a viscous Newtonian liquid. Correlate the predicted maximum stable bubble diameters obtained using numerical simulation with measurements of bubble size distributions and calculate an effective shear rate for the dispersion of air bubbles during continuous mixing of a Newtonian liquid.

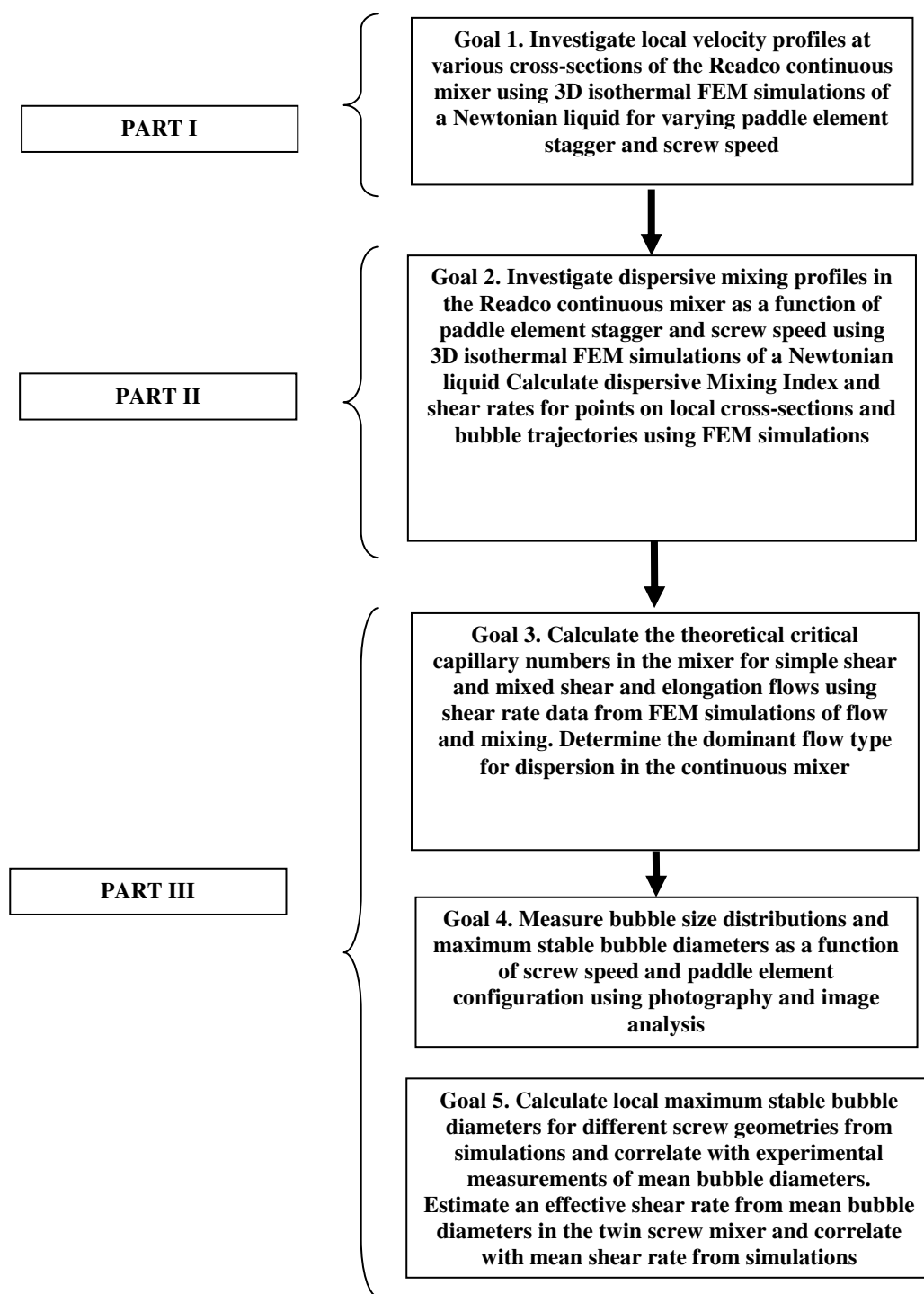


Figure 1.1 Research strategy

2. LITERATURE REVIEW

2.1 Origin of the Cellular Structure in Baked and Extruded Foods

The number and size distribution of air cells in solid food foams such as baked and extruded foods are a critical component of the perceived texture. Air incorporation and dispersion during mixing of dough results in formation of air bubbles that act as nuclei for air cells that are formed during dough fermentation and leavening (Bloksma, 1990; Eliasson and Larsson, 1993; Hosney, 1985; MacRitchie, et al., 1986). Gas bubbles also act as nucleating sites for air cells during direct and indirect expansion of extruded foods. The presence and size distribution of these bubbles in the polymer melt is determined by the conditions of the mixing or forming operation (Cisneros and Kokini, 2002). While the growth and coalescence of the bubbles is highly dependent on the rheological properties and moisture content of the food matrix, the number of cells is strongly dependent on bubble nucleation and bubble fragmentation.

Air nucleation during extrusion of biopolymer-water mixtures can be either homogeneous or heterogeneous. Homogeneous nucleation is the process of vapor evaporation and formation of critical ‘embryos’ or ‘nuclei’ from the liquid water which is superheated to a meta-stable equilibrium state. There is a minimum energy that is required for the embryos or nuclei to reach a critical size in order to develop into stable bubbles (Cisneros, 1998) (Figure 2.1).

In polymers the presence of free volume may lower the required free energy for homogeneous nucleation which is affected by temperature, pressure and concentration of dissolved air or other solutes in the matrix (Colton and Suh, 1987).

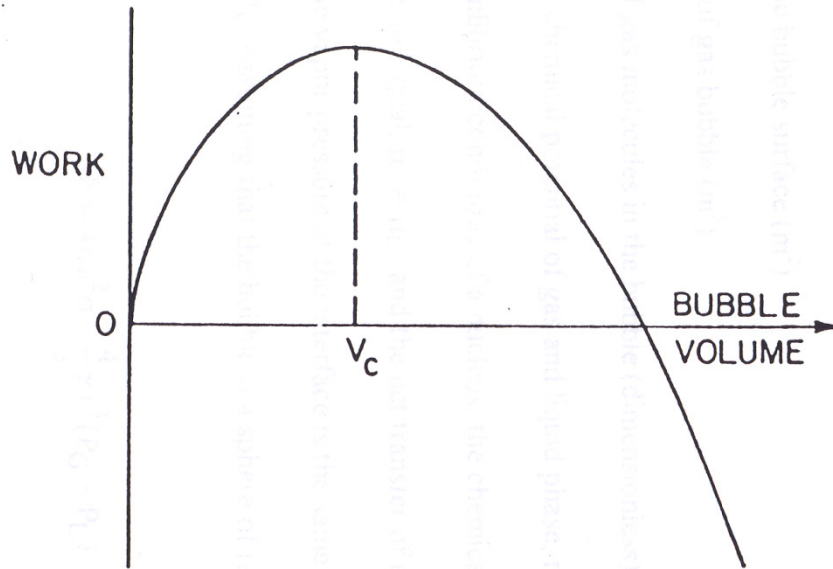


Figure 2.1: Schematic diagram showing the minimum work required for a bubble to reach a critical size (Blander and Katz, 1975)

The free energy required to create a stable bubble (ΔF) is a function of the bubble size (radius, r_c , or volume, V_c) and has a maximum value at the critical bubble size. The magnitude of this free energy for homogenous nucleation is given by

$$\Delta F_{\text{hom}} = \frac{4}{3} \pi r_c^2 \sigma = \frac{16}{3} \frac{\pi \sigma^3}{(P_G - P_L)^2} \quad (2.1)$$

where

r_c = critical radius of the bubble (m)

σ = surface tension of the surrounding liquid (Nm^{-1})

P_G = pressure of the gas phase (Pa)

P_L = pressure of the liquid phase (Pa)

The number density of the nuclei that can overcome the free energy barrier is calculated by the expression

$$N(r_c) = N \exp\left[\frac{-\Delta F(r_c)}{kT}\right] \quad (2.2)$$

where

N = constant approximately equal to the number density of volatile molecules in the metastable liquid

k = Boltzmann constant

T = absolute temperature of the gas phase

The steady rate of nucleation per unit volume (J) is estimated as the product of the number density ($N(r_c)$) and the collision frequency, λ :

$$J_{\text{hom}} = \lambda N(r_c) = \lambda N \exp\left[\frac{-\Delta F_{\text{hom}}}{kT}\right] \quad (2.3)$$

In heterogeneous nucleation vapor is generated in pre-existing nuclei caused by entrapped gas bubbles, suspended solids and other non-wetting surfaces which reduce the activation energy for the formation of nuclei of critical size. The free energy required for the formation of a bubble nucleus of critical size in this case is governed by :

$$\Delta F_{\text{het}} = \frac{16\pi\sigma_{VL}^3}{3\Delta P^2} S(\theta) \quad (2.4)$$

where

$$S(\theta) = \left(\frac{1}{4}\right)(2 + \cos\theta)(1 - \cos\theta)^2 \quad (2.5)$$

where θ is the wetting angle of the interface as shown in figure 2.2,

σ_{VL} is the interfacial tension at the vapor/liquid interface,

and ΔP is the pressure differential at the interface ($P_G - P_L$)

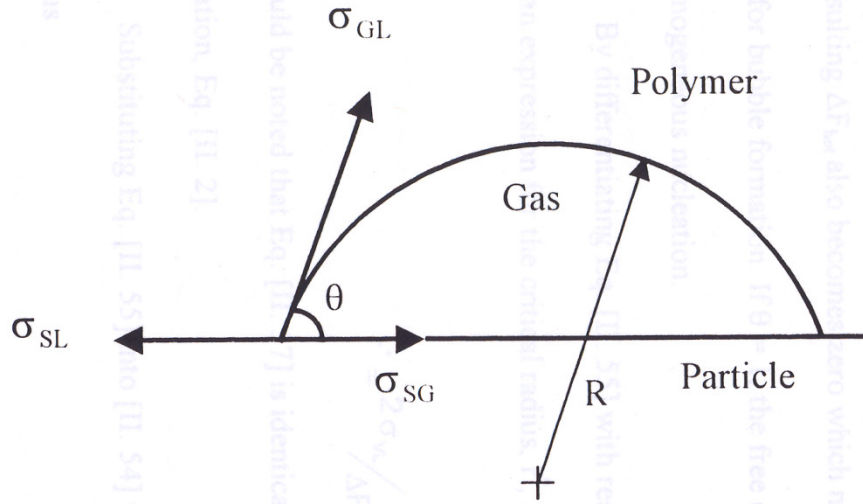


Figure 2.2: Wetting angle θ for a gas bubble at the interface of a solid particle during heterogeneous nucleation (Colton and Suh, 1987).

The heterogeneous nucleation rate is then given as :

$$J_{het} = \lambda N_1 \exp \left[\frac{-\Delta F_{het}}{kT} \right] \quad (2.6)$$

Where, N_1 is the number of heterogeneous nucleation sites

From the above equations it is observed that the free energy for homogeneous nucleation is greater than that for heterogeneous nucleation ($\Delta F_{hom} > \Delta F_{het}$). However since the number density of volatile compounds (N_0) in homogenous nucleation is usually greater than that of heterogeneous nucleation sites (N_1), the nucleation rate is lower during

heterogenous nucleation. Pre-existing gas bubbles if not already stable, will need a reduced amount of energy to grow into stable nuclei and will increase nucleation rates (Cisneros, 1998).

Extruded product texture and the number of gas cells found in expanded extrudates, have been shown to be a function of melt viscosity, die pressure and temperature. This suggests that heterogeneous nucleation is more predominant than homogeneous nucleation (Guy and Horne, 1988). Chang and Kokini (1992) used a single screw extruder to perform experiments with three different starchy biopolymers with low moisture contents: 98 % amylopectin starch at 20-35 % moisture, 70 % amylose corn starch at 19.2-30 % moisture and corn meal at 16-26 % moisture. The overall extrudate expansion resulted from structural order-disorder transitions induced by temperature and moisture, as well as nucleation of bubbles, extrudate swell, bubble growth and collapse. Extrudate expansion in low moisture content starchy biopolymer samples was found to be mainly controlled by the rate of bubble growth. Simplified mathematical models were developed to predict extrudate expansion at low moisture content:

$$\frac{\dot{R}}{R} = \frac{\Delta P}{4\eta} \text{ for Newtonian material surrounding the air cell} \quad (2.7)$$

$$\frac{\dot{R}}{R} = \left(\frac{\Delta P}{4m} \right)^{\frac{1}{n}} \text{ for non-Newtonian material surrounding the air cell} \quad (2.8)$$

where $\frac{\dot{R}}{R}$ is the rate of bubble growth, ΔP is the water vapor pressure at the dough temperature (T), η is the shear viscosity of the material and m and n are the power law parameters of the material.

Figure 2.3 shows schematically the effect of melt viscosity on the resulting pressure profile in the extruder die and on the expansion process. The pressure inside the die is a function of the die opening, flow rate and the material viscosity. In order for vapor bubbles to form, the pressure inside the die needs to be greater than the saturated water vapor pressure at the extrusion temperature. Figure 2.4 shows the effect of shear viscosity and moisture content on expansion. The specific volume is inversely proportional to the shear viscosity at any given moisture content while the moisture content is inversely proportional to the expansion at a given viscosity. The high melt viscosity at lower moisture contents prevents the bubble from collapsing after the expansion.

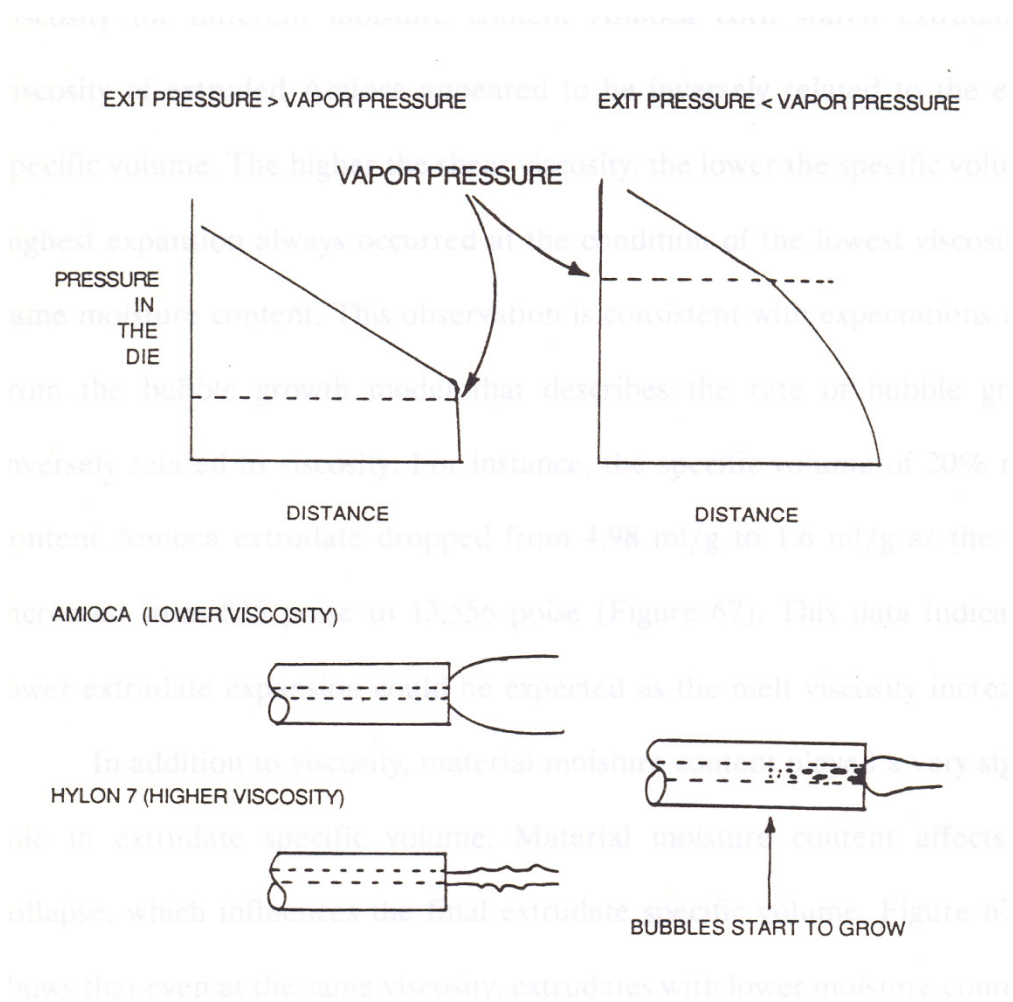


Figure 2.3 Effect of material rheology and vapor pressure on extrudate expansion (Chang, 1992).

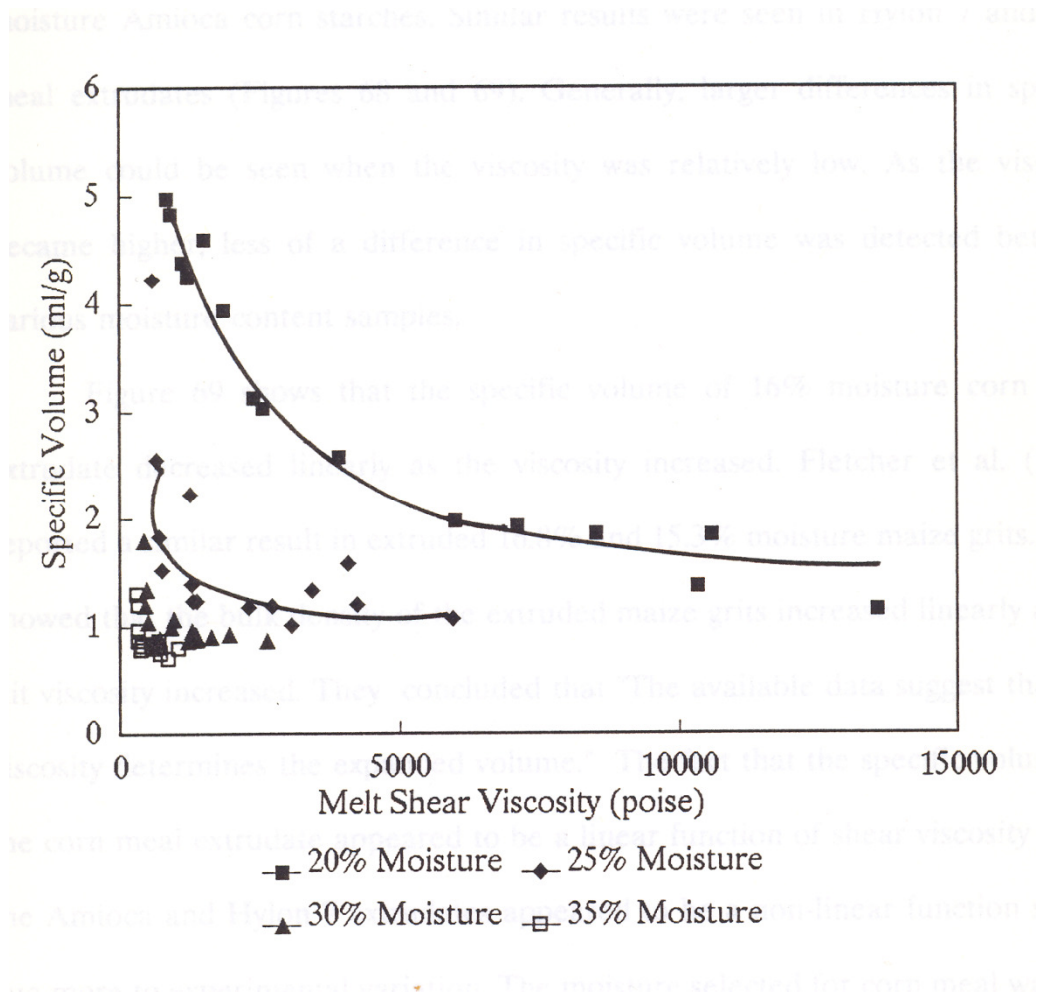


Figure 2.4 Effect of melt viscosity and moisture content on extrudate expansion of high amylopectin starch (Chang, 1992).

Specifically in baked and extruded products, emulsions, frozen dough products, cereal products, the number and size distribution of air cells influence the texture of the product (Barrett and Peleg, 1992; Dogan and Kokini, 2006). Cisneros & Kokini (2002) studied the effect of extrusion parameters and type of the starch on air entrapment and formation of nuclei during starch extrusion. The porosity of extruded products was found to be related to the barrel fill length where melting occurred and higher densities of bubbles in the unexpanded extrudate resulted in a finer cell structure after heat expansion.

A critical barrel fill length was also identified, above which the sample porosities were high (Figure 2.5). It was proposed that air bubbles formed out of the trapped air pockets in the granular feed material during the melting stage and the presence of a mass-filled section between the feeder port and the melting region prevented the escape of these air bubbles, resulting in higher porosities (Cisneros and Kokini, 2002).

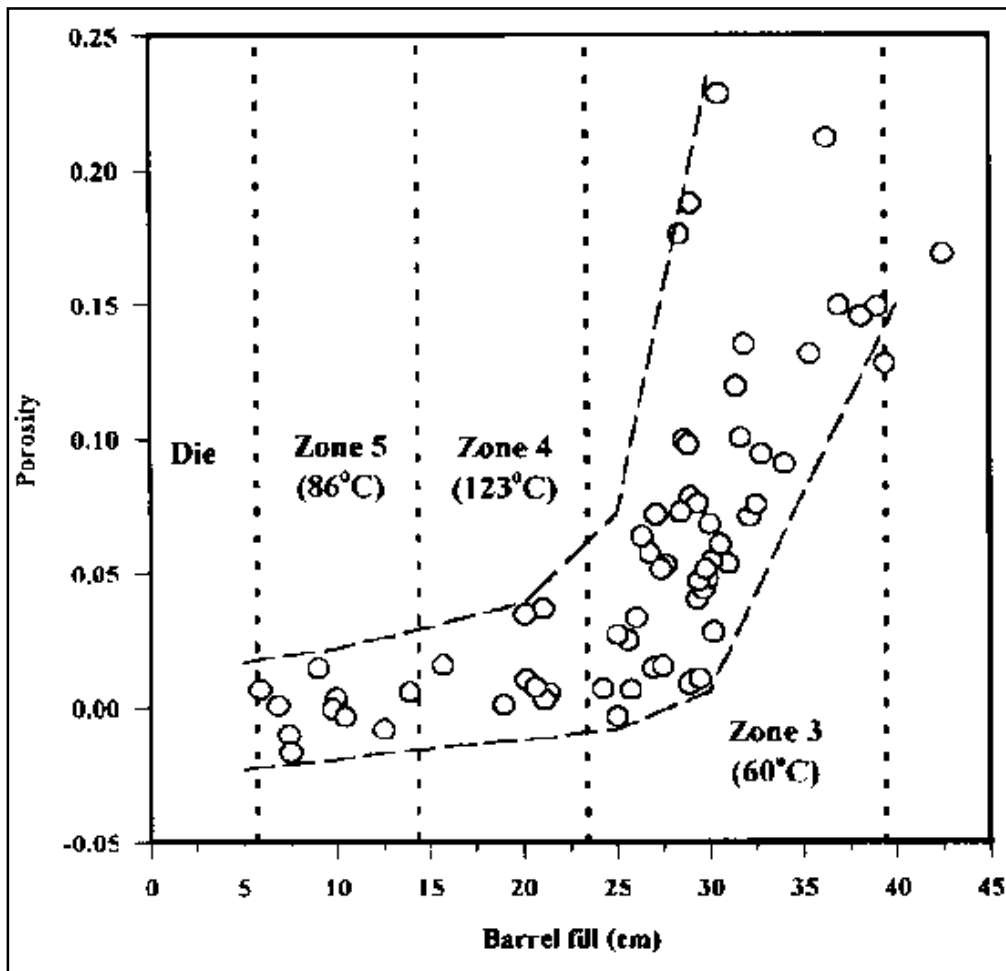
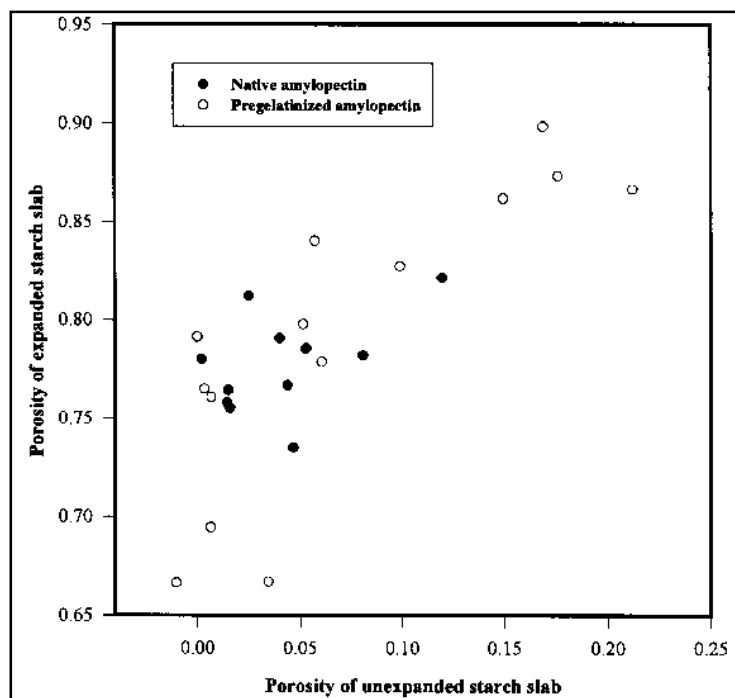
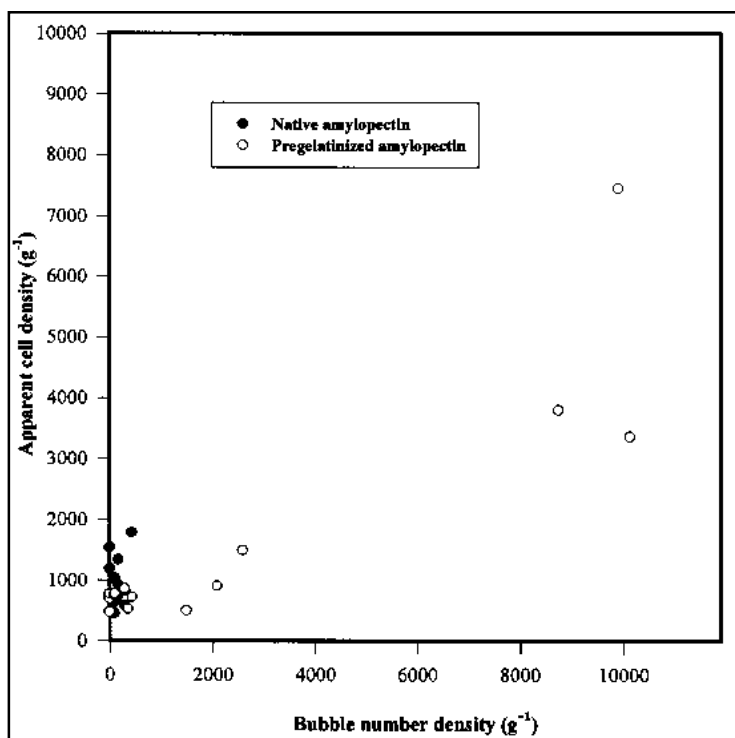


Figure 2.5: Porosity versus barrel fill for corn starch, as well as native and pregelatinized amylopectin (Cisneros and Kokini, 2002).

The porosity of the unexpanded extrudates and the bubble number density decreased with increasing screw speed (Cisneros and Kokini, 2002). It was proposed that this decrease in the number of air bubbles entrapped was a result of a corresponding decrease in the barrel fill length when the screw speed increased. The size of the bubbles decreased due to breakup into smaller bubbles, some of which were so small that they either dissolved or could not be detected. A direct relationship was found between porosity of the unexpanded and microwave expanded products, while the bubble number density before expansion correlated well with the expanded product cell structure as shown in Figure 2.6 (Cisneros and Kokini, 2002)



(a)



(b)

Figure 2.6. **a.)** Porosity and **b.)** Cell Density of starch extrudates before and after microwave expansion (Cisneros and Kokini, 2002).

Aeration of dough during mixing is also a critical step that defines the final product texture. For example the aeration during mixing of dough defines the quality of the baked loaf (Bloksma, 1990; Campbell and Shah, 1998; Eliasson and Larsson, 1993; Hosney, 1985; MacRitchie, 1986). The mechanisms that govern aeration during dough mixing include entrainment of air, disentrainment, bubble break-up, coalescence, and normal stress compression in viscoelastic materials. While the first two mechanisms determine the total air content in the dough, the breakup and coalescence influence the size distribution of the air bubbles. Campbell and Shah (1998) modeled the entrainment and disentrainment of air with changes in pressure during dough mixing in two kinds of Tweedy mixers. They proposed an exponential decay model for air disentrainment given by:

$$\frac{V_a(t) - V_{a_\infty}}{V_{a_0} - V_{a_\infty}} = V_a^*(t) = e^{-kt} \quad (2.9)$$

where V_{a0} and V_{a_∞} are the initial and final steady state air contents in the dough at the new pressure respectively. The disentrainment parameter k is estimated from a graph of $\ln(V_a)$ vs t as shown in the figure 2.7

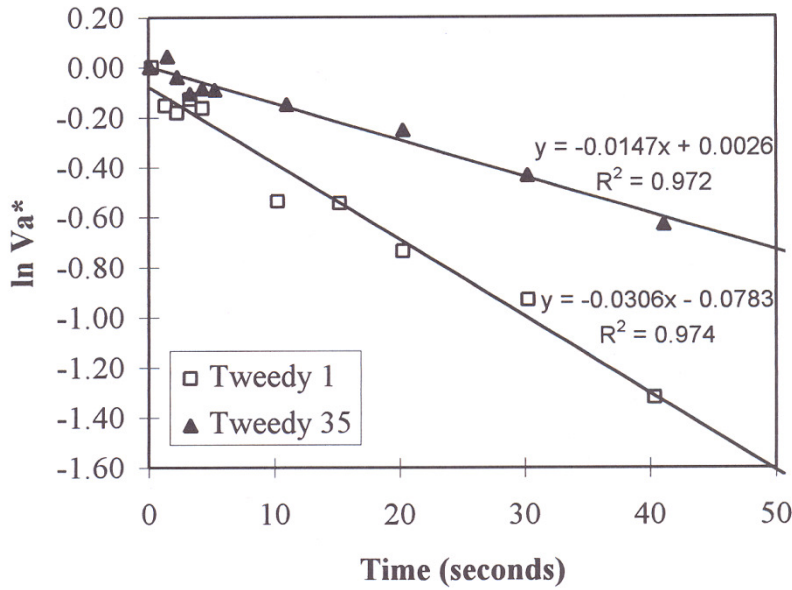


Figure 2.7 Disentrainment coefficient k calculated as the negative of the slope of the plot (Campbell and Shah ,1998).

Air bubbles incorporated during mixing of dough act as nuclei for CO_2 induced expansion of the dough. The bubbles grow due to the pressure difference between inside and outside of the bubble caused due the CO_2 released by the yeast (Kokini, et al.,1992; Campbell et al, 1998; Moraru and Kokini, 2003). Huang and Kokini,(1998) developed a gas cell growth model based on the biaxial extensional viscosity to predict the dough volume and concluded that in addition to the pressure difference across the gas cell, the gas cell expansion is also influenced by the biaxial rheological properties of the dough:

$$\left(\frac{1}{R_f}\right)^{\frac{3}{n}} - \left(\frac{1}{R_i}\right)^{\frac{3}{n}} = -\frac{3}{n} \cdot \left(\frac{2\pi}{KV^*}\right)^{\frac{1}{n0}} \cdot \Delta P^{\frac{1}{n}} \cdot (t_f - t_i). \quad (2.10)$$

where n and K are the power-law parameters of the biaxial viscosity η_B and extension rate $\dot{\epsilon}$ and ΔP is the pressure difference across the gas cell wall.

It was noted that the time scale for change in the overall air content was different from the time scale for changes in the bubble size distributions because of varying removal rates for bubbles of different sizes. The time to move a bubble a distance x toward the free surface under an imposed pressure gradient can be roughly estimated by:

$$t_p = \frac{12\mu x}{d^2(dP/dx)} \quad (2.11)$$

where μ is the local viscosity, d is the bubble diameter and P is the pressure (Foster and Lindt, 1990). Therefore, the larger bubbles move faster and the time can be shortened by applying of a vacuum.

While the final product texture is directly related to the growth of bubble nuclei, the size distribution of these bubble nuclei is affected by the flow and mixing processes that occur in a mixer or extruder. In order to investigate the effect of process parameters on bubble breakup, it is necessary to first understand the fundamentals of bubble breakup phenomena in controlled steady flows.

2.2 Deformation and break up of drops and bubbles in steady flows

The mechanism of breakup in drops and bubbles plays a crucial role in several unit operations in the food and chemical industry. Some examples include multiphase fluid transport, aerosol and emulsion manufacturing, atomization of liquid, aeration and mixing of fluids. Drops or bubbles undergoing shear deform and under sufficiently large local shear rate conditions, they break up. There is a significant body of literature available on fundamental theories aimed at quantifying the strength and type of flow required to cause break up of bubbles and drops in viscous flows, and the number of

droplets resulting from the breakup. Taylor (1934) was the first among a series of researchers to study deformation and breakup of droplets under viscous stresses. Several of the fundamental concepts discussed below can be found in Hinch and Acrivos (1979, 1980), Acrivos and Lo (1978), Barthes-Biesel and Acrivos (1980), Grace (1982), Acrivos (1983) and Bentley and Leal (1986).

2.2.1 Governing Equations and Fundamental Theories

Consider a drop of fluid with an equivalent radius a ($2a = d$) immersed in a surrounding fluid under motion. Assuming the drop size is considerably small compared to the scale of variation of the overall flow in the surrounding liquid, the undisturbed flow around the drop at a distance \mathbf{x} from the drop center can be written as follows, in a frame of reference in which the drop center is always at rest:

$$\mathbf{U} = \mathbf{x} \cdot \nabla \mathbf{U} \quad (2.12)$$

Equation (2.12) assumes that the drop is in a linear shear field causing point symmetric drop shapes and neglects the effect of gravity so that the drop deformation and breakup is caused solely due to the local velocity gradient. The assumptions include incompressible flow of a Newtonian fluid at constant temperature and negligible mass transfer between the two phases.

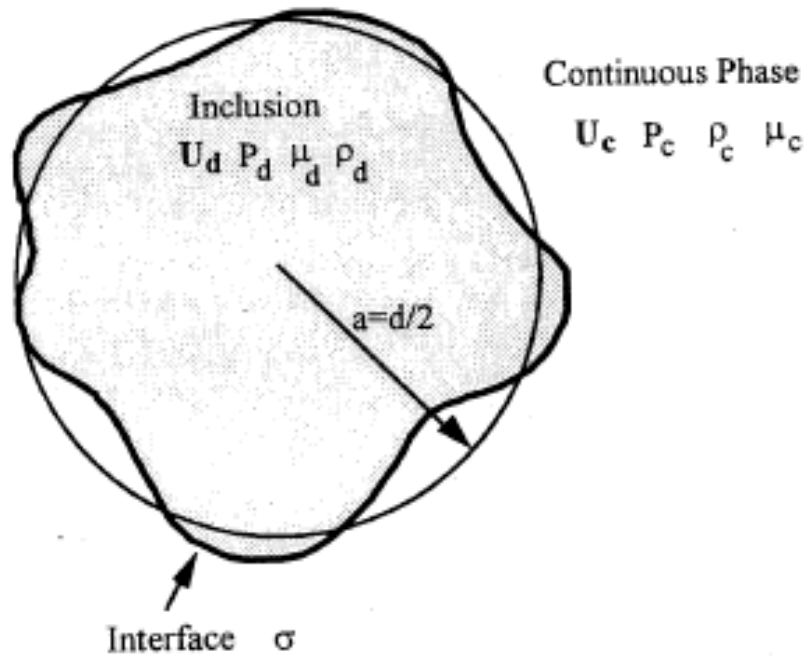


Figure 2.8: Diagram showing the properties of the continuous and discontinuous media and the interface of the drop (Risso, 2000).

Defining each phase with the subscript k , the properties are denoted as density ρ_k , dynamic viscosity μ_k , the pressure and velocity fields by P_k and U_k respectively, the viscosity ratio p is a useful parameter in the analysis defined as

$$p = \frac{\mu_d}{\mu_c} \quad (2.13)$$

where $p \rightarrow 0$ corresponds to a bubble and $p \rightarrow \infty$ corresponds to a highly viscous drop.

The local mass and momentum conservation for each phase governed by:

$$\nabla \cdot (\rho_k \mathbf{U}) = 0 \quad (2.14)$$

and,

$$\rho_k \left(\frac{\partial \mathbf{U}_k}{\partial t} + (\mathbf{U}_k \cdot \nabla) \mathbf{U}_k \right) = \nabla \cdot \left(-P_k \mathbf{I} + \mu_k (\nabla \mathbf{U}_k + (\nabla \mathbf{U}_k)^T) \right) + \rho_k \mathbf{g} \quad (2.15)$$

where \mathbf{g} is the acceleration due to gravity

The Reynolds number, Re_k , for flow inside and outside the drop is different and is defined with respect to the drop radius is:

$$Re_k = \frac{\rho_k G a^2}{\mu_k} \quad (2.16)$$

where G is the local outer fluid flow strength. In simple shear flow this quantity would be equal to the local shear rate. For $Re_k \ll 1$, in very slow flows such as in the case of an air bubble in a highly viscous surrounding fluid, inertia and effect of gravity can be neglected and equations (2.14) and (2.15) can be simplified as:

$$\nabla \cdot \mathbf{U} = 0 \quad (2.17)$$

And,

$$\nabla \cdot \left(-P_k \mathbf{I} + \mu_k (\nabla \mathbf{U} + (\nabla \mathbf{U})^T) \right) = 0 \quad (2.18)$$

The appropriate boundary conditions are:

$$\mathbf{U} = \mathbf{x} \cdot \nabla \mathbf{U} = G(\mathbf{e} + \boldsymbol{\omega})\mathbf{x}, \text{ for } |\mathbf{x}| \rightarrow \infty \quad (2.19)$$

where \mathbf{e} is the dimensionless rate of deformation or rate of strain tensor and $\boldsymbol{\omega}$ is the dimensionless rate of rotation or the vorticity tensor.

The interface conditions defining the continuity of velocity and stress at the interface surface, S , of each bubble or droplet are given by the equations:

$$[\mathbf{U}]_s = 0$$

and

$$\left[\left(-P_k \mathbf{I} + \mu_k (\nabla \mathbf{U} + (\nabla \mathbf{U})^T) \right) \mathbf{n} \right]_s = 2H\sigma \mathbf{n} = \sigma \nabla \cdot \mathbf{n} \quad (2.20)$$

where σ is the interfacial tension between the two fluids and H is defined as the mean curvature measured on the normal \mathbf{n} at the interface and is equal to the divergence of \mathbf{n} (i.e., $\nabla \cdot \mathbf{n}$). For example, $H = 'a'$ for a spherical particle with \mathbf{n} directed outwards. $[\]_s$ denotes the change in the bracketed quantity across the interface S .

Finally, the kinematic condition for change in drop shape at surface S is symbolically given as:

$$dS/dt = \mathbf{U} \cdot \mathbf{n} \quad (\text{for all points on the surface } S) \quad (2.21)$$

For a situation where $p \ll 1$ and when the surface tension rather than the flow dominates the drop shape, the scaling is done for the lengths by radius a , and times by the surface tension relaxation time, $\mu a / \sigma$. Thus the velocities are scaled by σ / μ and the pressure by σ / a . The dimensionless form of the boundary condition equations of (2.19) and (2.20) would be:

$$\mathbf{U} = Ca(\mathbf{e} + \boldsymbol{\omega})\mathbf{x} \quad \text{for } |\mathbf{x}| \rightarrow \infty \quad (2.22)$$

and,

$$[\mathbf{U}]_s = 0, \quad \left[\left(-P_k \mathbf{I} + \mu_k (\nabla \mathbf{U} + (\nabla \mathbf{U})^T) \right) \mathbf{n} \right]_s = \mathbf{n} \nabla \cdot \mathbf{n} \quad (2.23)$$

where Ca is the dimensionless Capillary Number defined as:

$$Ca = \frac{\mu G a}{\sigma} \quad (2.24)$$

The Capillary number, Ca , can be physically interpreted as the dimensionless ratio of the deforming viscous stress (of the order μG) to the resisting interfacial stress (of the order σ/a).

From the creeping flow analysis of drop deformation in flow, it can be concluded that the dimensionless parameters that govern the drop deformation and burst are:

1. p , the viscosity ratio between the discontinuous phase (drop or bubble) and the continuous phase (surrounding viscous liquid)
2. Ca , the dimensionless Capillary number which is a ratio of flow stress to the surface stress
3. The tensorial character of the velocity gradient tensor, or the flow type, which is defined by the relative magnitudes of \mathbf{e} and $\mathbf{\omega}$

Equation (2.24) implies that Ca increases with drop diameter. It would be expected that there is a maximum stable drop diameter d_{max} beyond which the drops cannot withstand breakup due to the external flow. Increasing the Ca would result in steady deformation of the drop until the drop can no longer sustain a steady deformation and breaks. A critical Ca can be found beyond which the drop is expected to break. In this case the Ca and the Capillary number at breakup is called the critical Capillary number denoted by Ca_{cr} .

2.2.2 Measurement of drop deformation

During experimental and theoretical investigations of drop breakup, the deformation of the drop is quantified using the deformation parameter, D_f , defined in terms of the long and short semi-axes of the drop cross section. This parameter is usually applicable for small deformations where the shape of the drop can be approximated by an ellipsoid (Figure 2). The limits of D_f are zero for a spherical drop shape and one for infinitely extended drops. At very large deformations, the change in D_f is small with any further increases deformation of the drop. In this scenario, L/a , is used in this case where a is the radius of the un-deformed spherical drop of the same volume.

$$D_f = \frac{L - B}{L + B} \quad (2.25)$$

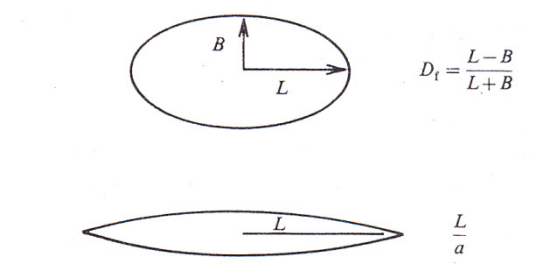


Figure 2.9 Measurement of parameters for drop deformation (Bentley and Leal, 1986) .

2.2.3 Characterization of flow type

Since the work of Taylor (1934), various researchers have experimentally studied drop breakup dynamics in linear two-dimensional flows created with a great deal of control. The simplest of these were simple shear and plane hyperbolic (uniaxial extension)

flows (Grace, 1982; Taylor, 1934). Simple shear flow can be defined by the velocity profile given by:

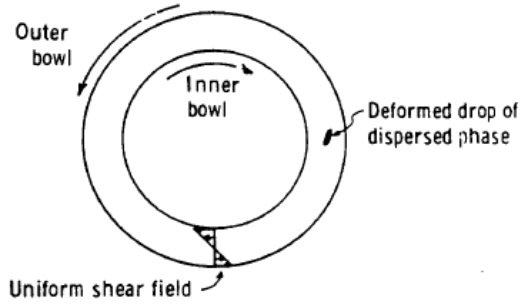
$$\mathbf{U} = (Gy, 0, 0) \text{ with } \mathbf{e} = \frac{1}{2} \begin{pmatrix} 0 & 1 & 0 \\ 1 & 0 & 0 \\ 0 & 0 & 0 \end{pmatrix} \text{ and } \mathbf{\omega} = \frac{1}{2} \begin{pmatrix} 0 & 1 & 0 \\ -1 & 0 & 0 \\ 0 & 0 & 0 \end{pmatrix} \quad (2.26)$$

Thus, simple shear is a flow type that has equal parts of rate of strain and vorticity. This type of flow was achieved using a couette or a parallel band apparatus as shown in Figure 2.10a and 2.10b.

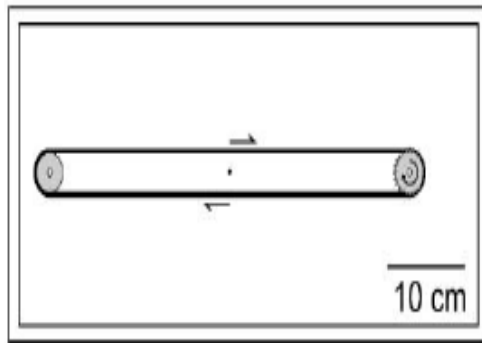
Plane hyperbolic flow has a velocity profile given by:

$$\mathbf{U} = G(x, -y, 0) \text{ with } \mathbf{e} = \begin{pmatrix} 1 & 0 & 0 \\ 0 & -1 & 0 \\ 0 & 0 & 0 \end{pmatrix} \text{ and } \mathbf{\omega} = \mathbf{0} \quad (2.27)$$

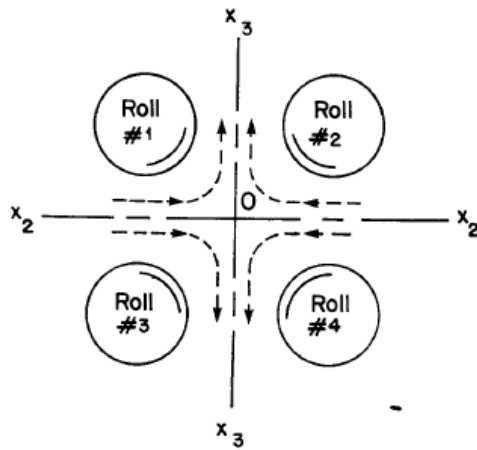
It can be seen from equation 2.27 that plane hyperbolic or uniaxial flow has no contribution from vorticity and thus is a pure straining flow. This type of flow was achieved using a four-roll mill (Figure 2.10c) where the rotation of the four rolls with equal velocities created a stagnation point in the centre region around which the flow could be approximated to uniaxial extension.



(a)



(b)



(c)

Figure 2.10 (a) Couette apparatus (Grace, 1982), (b) parallel band apparatus (Rust and Manga, 2002), and (c) Four-roll mill apparatus (Grace, 1982).

In general, planar flows can be characterized by a flow type parameter ' α ' where the dimensionless rate of strain and vorticity tensors are defined as

$$\mathbf{e} = \frac{1}{2}(1+\alpha) \begin{pmatrix} 1 & 0 & 0 \\ 0 & -1 & 0 \\ 0 & 0 & 0 \end{pmatrix} \text{ and } \mathbf{\omega} = \frac{1}{2}(1-\alpha) \begin{pmatrix} 0 & 1 & 0 \\ -1 & 0 & 0 \\ 0 & 0 & 0 \end{pmatrix}, \text{ where } -1 \leq \alpha \leq 1 \quad (2.28)$$

Equation 2.28 represents a full range of flows with $\alpha = -1$ for pure rotation, $\alpha = 0$ for simple shear and $\alpha = 1$ for pure elongation flows. Figure 2.11 illustrates the streamlines for a range of flows between simple shear and pure elongation (Bentley and Leal, 1986).

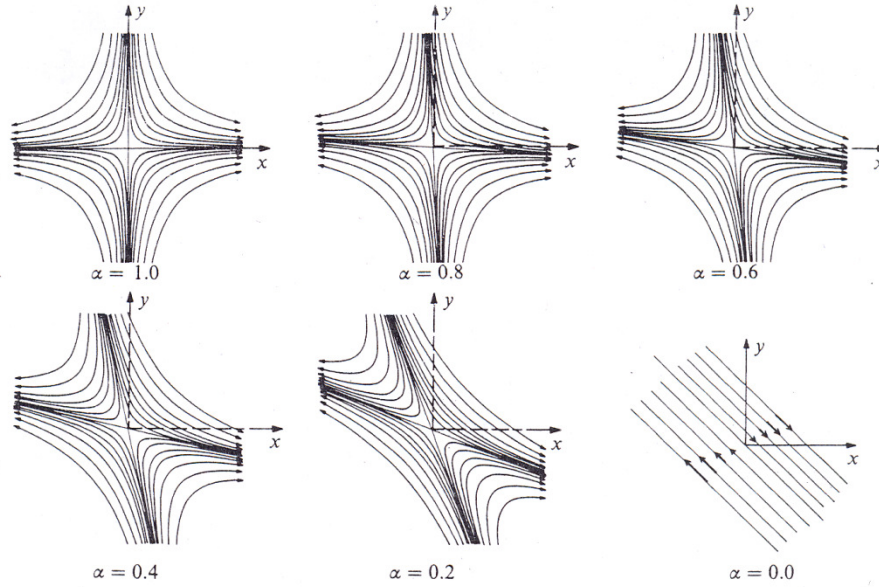


Figure 2.11 Streamlines of flow for varying values of α (Bentley and Leal, 1986).

The relative strength of deformation to rotation in such flows is given by”

$$\frac{\text{magnitude of strain rate}}{\text{magnitude of vorticity}} = \frac{1+\alpha}{1-\alpha} \quad (2.29)$$

In flows with non-zero vorticity the bubble/drop would experience rotation and align with the linear exit streamline which is at an angle θ with the x-axis and would vary with the flow type as:

$$\sin(2\theta) = \frac{\alpha - 1}{\alpha + 1} \quad (2.30)$$

2.2.4 Evaluation of drop breakup criteria in steady flows

The equilibrium deformation, D_f , and orientation, θ , of drops are functions of the capillary number (Ca), the viscosity ratios (p) and the flow type (α) (Bentley and Leal, 1986):

$$D_f = D_f(Ca; p, \alpha), \text{ or } L/a = L/a(Ca; p, \alpha) \text{ and } \theta = \theta(Ca; p, \alpha) \quad (2.31)$$

The critical capillary Number, Ca_{cr} , for drop breakup is a function of p and α (Bentley and Leal, 1986):

$$Ca_{cr} = Ca_{cr}(p, \alpha) \quad (2.32)$$

The maximum stable deformation, D_{fc} , and the orientation at breakup just before Ca_{cr} , are also functions of p and α (Bentley and Leal, 1986):

$$D_{fc} = D_{fc}(p; \alpha), \text{ and } \theta_c = \theta_c(p; \alpha) \quad (2.33)$$

Experimental investigations of drop deformation and breakup were done by Taylor (1934), Grace(1982), Bentley and Leal(1986), while Taylor (1934; 1964), Acrivos and Lo (1978), Hinch and Acrivos (1980) and Khakhar and Ottino (1986) developed theoretical correlations for drop breakup that was correlated with experimental data. Taylor (1934), conducted experiments on drop deformation and breakup in two flow

types, simple shear ($\alpha = 0$) and pure extension ($\alpha = 1$), as they were achievable through relatively simple apparatus. The deformation of initially spherical immiscible drops in response to external flow was measured in systems with viscosity ratio as low as 0.0003. Experiments were performed with a four-roll apparatus (for extensional flow) and a parallel band apparatus (for simple shear flow) shown in figure 2.10. For fixed values of the viscosity ratio, p , the deformation, D_f , increased linearly with Ca , for small deformations. This study was the first to show that the critical Ca needed for drop breakup was of the order of 10^3 higher in simple shear flow compared to extensional flow.

Grace (1982) extended the analysis to a broader range of fluid systems that had a viscosity ratio, p , ranging from 10^{-6} to 950 and Re ranging from 10^{-6} to 10^{-2} . Specifically, breakup criteria for drops in simple shear (couette-flow) and irrotational flows (four-roll mill flow) and breakup of immiscible jet stream in laminar flow were correlated to drop dispersion efficiency of a Kenics static mixer. Figure 2.12 shows the Ca_{cr} as a function of the viscosity ratio, p , for both rotational and irrotational shear flow types which confirm the results of Taylor (1934).

Bentley and Leal (1986) further extended the experimental analysis to a range of flow types between simple shear and extension flow using a computer controlled four-roll mill. By varying the rotational speeds of each of the four rolls, they were able to attain flow types that included $\alpha = 0.2, 0.4, 0.6, 0.8$ and 1.0 .

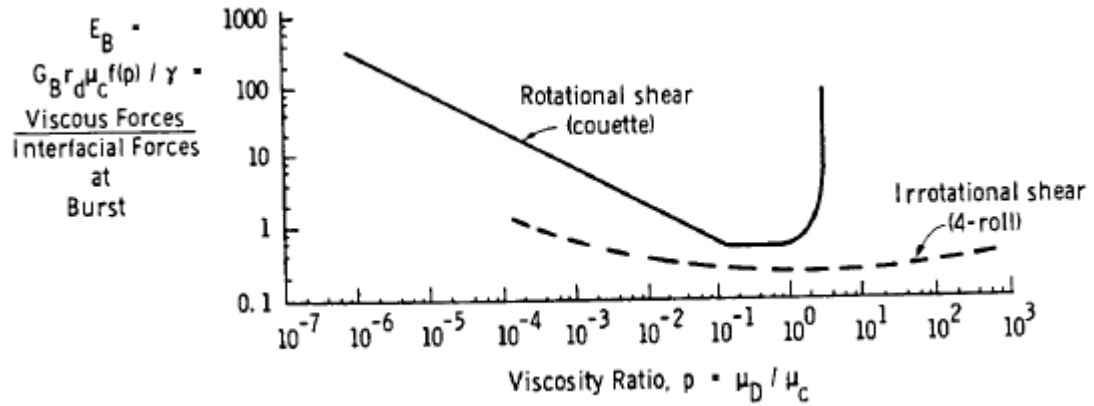


Figure 2.12 Ca_{cr} as a function of the viscosity ratio, p for rotational and irrotational flows Grace (1982).

The work of Taylor (1934) was also instrumental in classifying the drop deformation into ‘small’ and ‘large’ based on the flow strength (shear and extensional rate) and viscosity ratio. At low flow strengths ($Ca \ll 1$), the drops of all viscosity ratios would form slightly deformed shapes (ellipsoidal) and at higher flow strengths they would tend to form highly elongated slender shapes. This distinction in the drop shapes attained prior to breakup led to the branching of theoretical analysis of drop breakup into ‘small-deformation theory’ (Barthes-Biesel and Acrivos, 1973; Taylor, 1964) and ‘large – deformation’ theory or ‘slender body analysis’ (Acrivos and Lo, 1978; Khakhar and Ottino, 1986). The small deformation theory assumes that the drop is only slightly deformed and solves for the velocity fields inside and outside the drop and the drop shape. This analysis is applicable when the flow strength is weak ($Ca \ll 1$) or when the viscosity ratio is large ($p \gg 1$). It does not accurately predict breakup criteria when large drop deformations are seen, particularly for $p < 0.05$.

Acrivos and Lo (1978) developed a criterion for breakup of drop of low but finite viscosity in axisymmetric extensional flow defined in rotational co-ordinates x , r and θ , by:

$$\begin{aligned} u_x &= Gx, \\ u_r &= -\frac{1}{2}Gr, \\ u_\theta &= 0 \end{aligned} \tag{2.34}$$

In such a flow the drop cross-section at any point along the elongated slender elliptic shape would be circular and the drop centerline would be aligned along the x -axis, making the analysis simpler. The shape of the slender drop is then given as:

$$r = \varepsilon R(x), \tag{2.35}$$

where ε is called the slenderness ratio, which is assumed to be small because of the large drop deformation, and is defined by:

$$\varepsilon = \frac{\sigma}{G\mu_c L}, \tag{2.36}$$

An analysis of the creeping flow equations for the case $p \ll O(\varepsilon^2)$ gave the drop shape equation:

$$R(x) = \frac{1}{8} \left[1 + \left(1 - \frac{64}{K^2} \right)^{\frac{1}{2}} \right] (1 - x^2), \tag{2.37}$$

where $K^2 = \varepsilon^2 / p$. They found that equation (2.37) was stable only for $K^2 < 576/5$. By applying condition of volume conservation to equation (2.37) they obtained the following relation for drop deformation:

$$Ca \cdot p^{\frac{1}{6}} = \left(\frac{1}{20} \right)^{\frac{1}{2}} \frac{\xi^{\frac{1}{2}}}{1 + \frac{4}{5}\xi^3}, \tag{2.38}$$

where ξ is the dimensionless length defined as

$$\xi \equiv \frac{L \cdot p^{\frac{1}{3}}}{a} \quad (2.39)$$

From a plot of the above deformation curve they found the critical capillary number for uniaxial extension as:

$$Ca_{cr} = 0.148 p^{-\frac{1}{6}} \quad (2.40)$$

Hinch and Acrivos (1979) extended this analysis to two-dimensional planar extension ($\alpha = 1$). In this case, the drop cross-section would not be circular when compared to axisymmetric extension. They found that the critical capillary number differed only slightly in the constant value (0.148 vs. 0.145) and concluded that the cross-sectional area, which remained the same in two-dimensional straining flow, rather than the shape, governed the drop deformation and burst:

$$Ca_{cr} = 0.145 p^{-\frac{1}{6}} \quad (2.41)$$

Hinch and Acrivos (1980) studied the case of simple shear ($\alpha = 0$) and found:

$$Ca_{cr} = 0.0541 p^{-\frac{2}{3}} \quad (2.42)$$

Bentley and Leal (1986) predicted and experimentally verified the Ca_{cr} for mixed simple shear and pure extension ($\alpha = 0.2, 0.4, 0.6, 0.8$ and 1.0) as:

$$Ca_{cr} = \frac{0.145 p^{-\frac{1}{6}}}{\alpha^{\frac{1}{2}}} \quad (2.43)$$

Though their experiments included p values up to a lower limit of 10^{-3} , they predicted the correlation to be better for even lower values of the viscosity ratios.

Khakhar and Ottino (1986) confirmed (2.41) and (2.42) through numerical analysis. Figures 2.13 to 2.15 show their correlations in comparison with the experimental work of Grace (1982) and Bentley and Leal (1986).

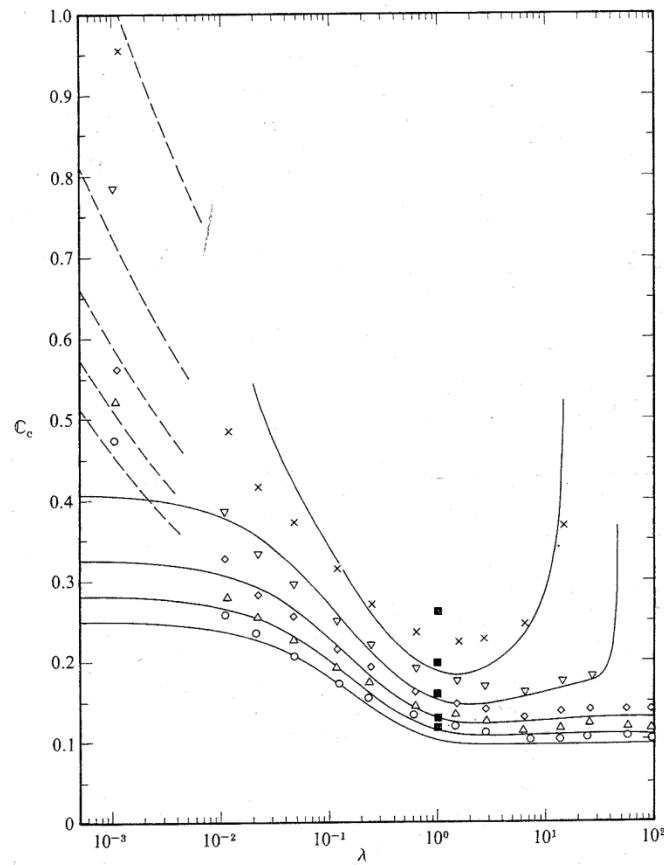


Figure 2.13 Experimental measurements of Ca_{cr} for $\alpha = 0.2, 0.4, 0.6, 0.8$ and 1.0 . open symbols – experiments ; solid lines – small deformation theory; broken lines – large deformation theory (Bentley and Leal, 1986) .

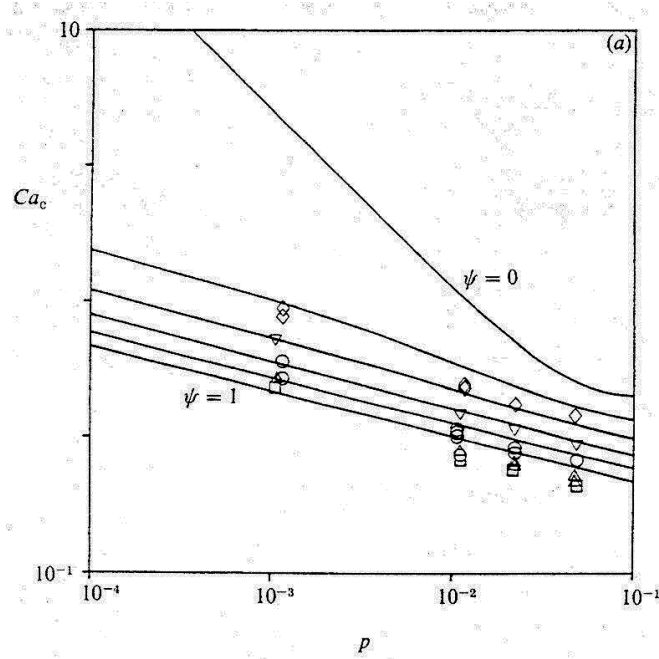


Figure 2.14 Numerical estimates of Ca_{cr} – comparison with experiments of Bentley and Leal (1986), Khakhar and Ottino (1986). Note: usage of ψ in place of α

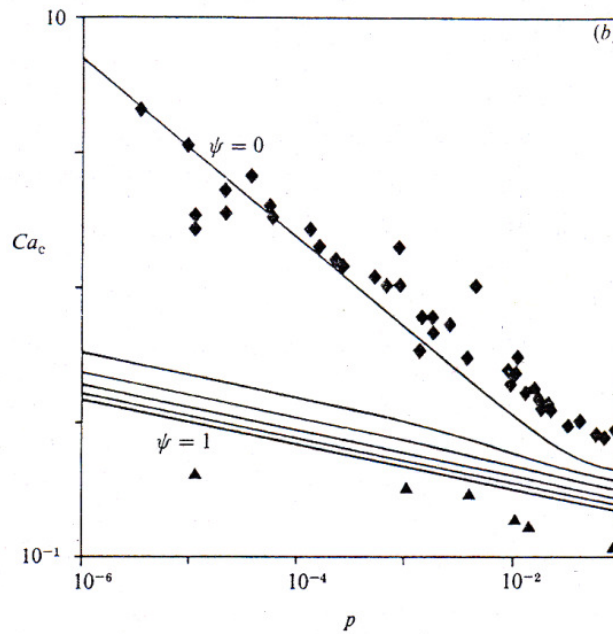


Figure 2.15 Numerical estimates of Ca_{cr} – comparison with experiments of Grace (1982), Khakhar and Ottino (1986). Note: usage of ψ in place of α

Figure 2.16 shows a condensed graph for all the types of flow which predicts for $p \sim 10^{-6}$, the jump in Ca_{cr} to be in the order of 10^3 for a shift in the flow type from $\alpha = 0.2$ to 0 (Meijer and Janssen, 1994). Thus the available drop breakup theories provide a foundation to predict low Re drop and bubble breakup in highly viscous mixing flows based on an analysis of the flow type. The results suggest that at comparable shear rates, bubbles and low viscosity drops ($p \rightarrow 0$) would breakup in mixing flows with greater incidence of extensional flow character ($\alpha > 0.2$) compared to simple shear ($\alpha = 0$).

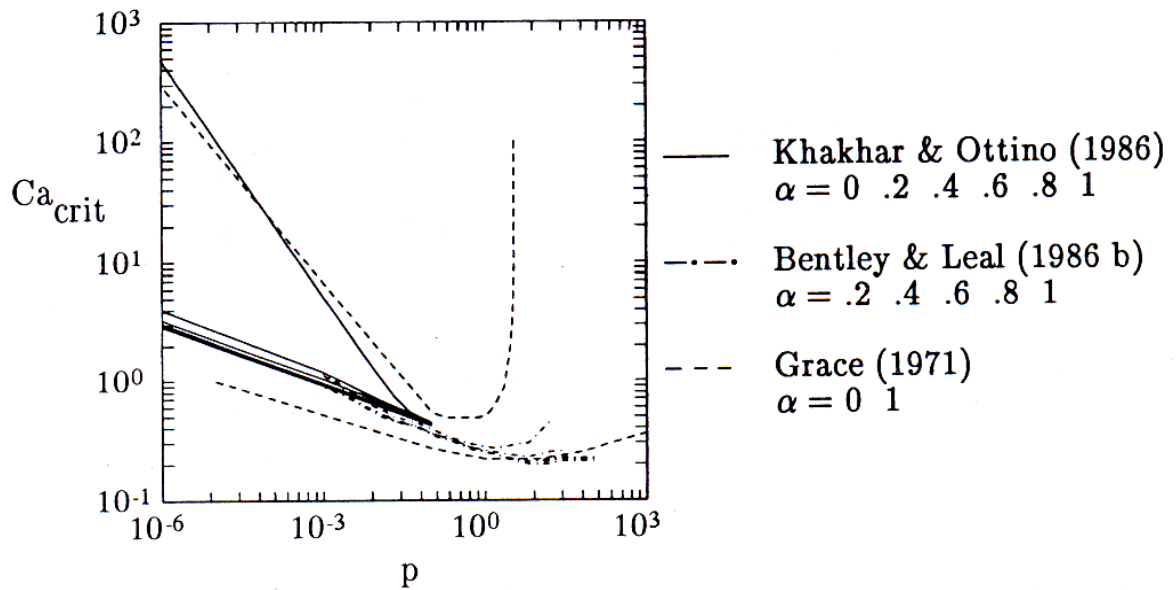


Figure 2.17 Comparison of Ca_{cr} vs p in simple shear and pure elongation flows from experimental and numerical studies (Meijer and Janssen, 1994).

When the viscosity of the drop is taken as identically equal to zero (i.e., for the case of an inviscid drop ($p = 0$) in zero-Reynolds number axisymmetric extensional flow) the deformation relation obtained would be given by the equation:

$$\frac{L}{a} = \left(\frac{G\mu a}{\sigma} \right)^2 \quad (2.44)$$

Equation 2.44 suggests that a stable drop shape can exist for all values of the flow strength G , when the viscosity ratio, p , is equal to 0. Thus, a gas bubble in a zero-Reynolds number flow would attain highly elongated shapes that are stable. This is because with a proper choice of the cross-sectional radius, it is always possible for the external normal stress deforming the bubble to balance the capillary force. If the viscosity ratio $p \ll 1$ but non-zero, the deformation relationship changes to the form in equation 2.31, in which case a critical breakup point can be found using the creeping flow assumption as given in equation 2.16 (Acrivos, 1983; Acrivos and Lo, 1978). However for highly elongated bubble shapes, the Reynolds number based on the half-length of the drop may not be negligible and the inertial effects on drop deformation and breakup must be considered. The breakup criterion for an inviscid drop ($p = 0$) considering the external flow inertia was obtained by Acrivos and Lo (1978) in axisymmetric extensional flow as

$$Ca_{cr} = 0.284 \left(\frac{\rho a \sigma}{\mu^2} \right)^{-1/5} \quad (2.45)$$

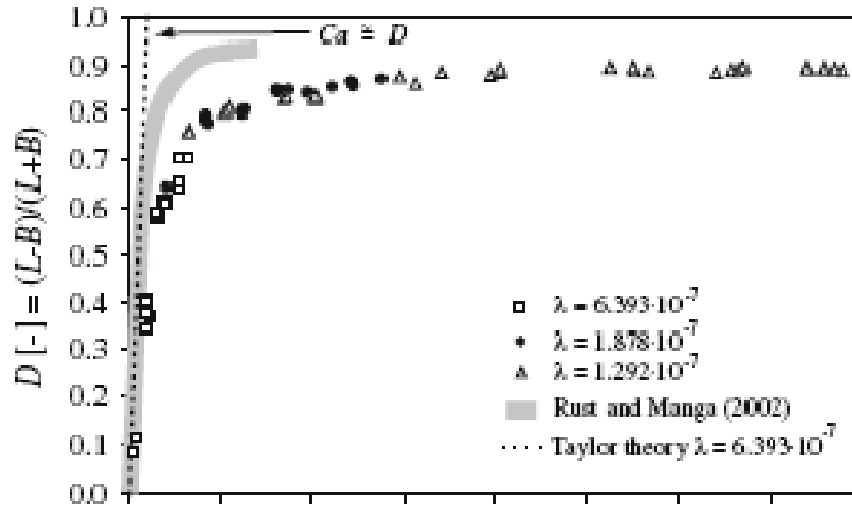
This relationship was found to be unchanged for a hyperbolic flow (Hinch and Acrivos, 1979).

Canedo et al., (1993) studied the deformation of air bubbles in Newtonian polyisobutenes under simple shear flows using a couette apparatus. The viscosities of the continuous media were 25.0 Pa.s and 85.4 Pa.s and the highest shear rates reached were 20 s^{-1} . In the range of Capillary Numbers investigated ($3 < Ca < 48$), the bubbles reached

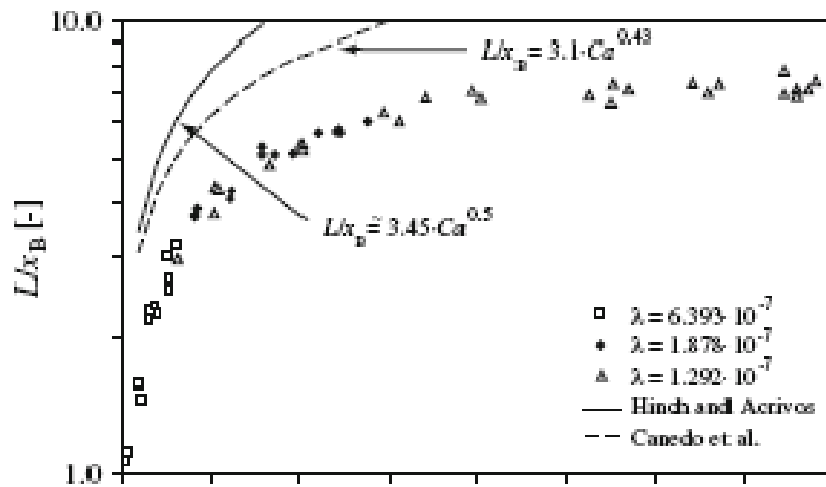
highly elongated stable shapes with no breakup occurring. Rust and Manga (2002) used a parallel band apparatus to create a simple shear flow profile in a corn syrup with a viscosity 118 Pa.s. In the range of shear rates between 0.00921 s^{-1} and 1.77 s^{-1} and Ca between 0.02 and 7.1, the bubble deformations reached $D = 0.94$ ($L/a = 32$) without any breakup even after the flow was stopped. Figures 2.13 (a) and (b) show the correlations between the deformation and Ca . For small deformations or small Ca , the deformation parameter D was proportional to Ca , while at larger deformations, the data of Rust and Manga (2002) fitted very well with the deformation equation developed by Hinch and Acrivos (1980) (equation 2.46) while the data of Canedo et al (1993) underestimates the correlation.

$$\frac{L}{a} = 3.45Ca^{0.45} \quad (2.46)$$

More recently Muller-Fischer et al (2008) studied the deformation of air bubbles in simple shear flow obtained in a concentric cylinder device and a parallel band device and found the deformation in simple shear flow to be in qualitative agreement with the experimental data Rust and Manga (2002) and Candeo et al (1993) and the analytical equation of Hinch and Acrivos (1980) (Figure 2.13).



(a)



(b)

Figure 2.13 (a) Deformation parameter, D and (b) Dimensionless extension ratio, L/a as a function of Ca for air bubbles in simple shear flow (Muller-Fischer et al., 2008).

Muller-Fischer et al. (2008) also estimated the Ca_{cr} for bubble breakup in Newtonian simple shear flow ($p \sim 3.09 \times 10^{-7}$) using a parallel band apparatus. The Ca_{cr} was lower than that predicted for drops previously and tip streaming was observed defined as the formation of small bubbles at both tips and ends of the elongated bubble (Figure 2.14).

This happened at lower than critical values of Ca . However they noted that no clear distinction between fracture and tip streaming could be observed for bubble breakup.

Their correlation for Ca_{cr} in simple shear flow for bubbles was:

$$Ca_{cr} = 2.465 p^{-0.171} \quad (2.47)$$

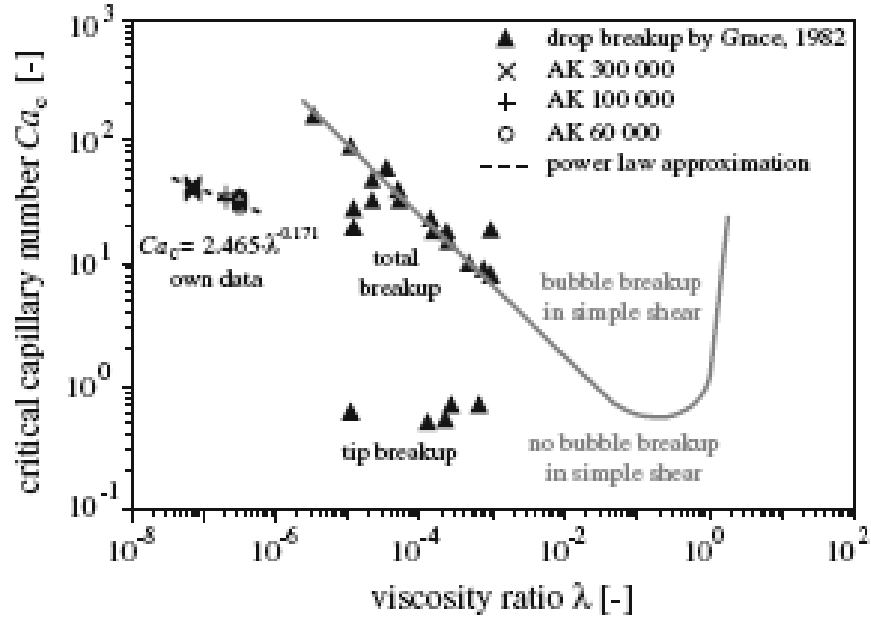


Figure 2.14 Ca_{cr} for bubble breakup in simple shear flow obtained in a concentric cylinder device (Muller-Fischer et al., 2008). Data for air bubbles (Muller-Fischer et al., 2008) compared with data for droplets (Grace, 1982).

Favelukis et al. (2005), studied the deformation and breakup of a slender non-Newtonian drop in extensional and creeping flow. They used a power-law fluid with viscosity ratio given by:

$$p = \frac{mG^n}{\mu_c} \quad (2.48)$$

where m and n are the power-law parameters of the dispersed phase.

The breakup criterion was obtained as:

$$Ca_{cr} = f_{\max} \cdot p^{-1/[3(1+n)]} \quad (2.49)$$

where:

$$f_{\max} = 0.148 + 0.0454(1 - n) \quad (2.50)$$

It was found that at a given viscosity ratio p , the Ca_{cr} for drop breakup increases with increasing value of n (Figure 2.15).

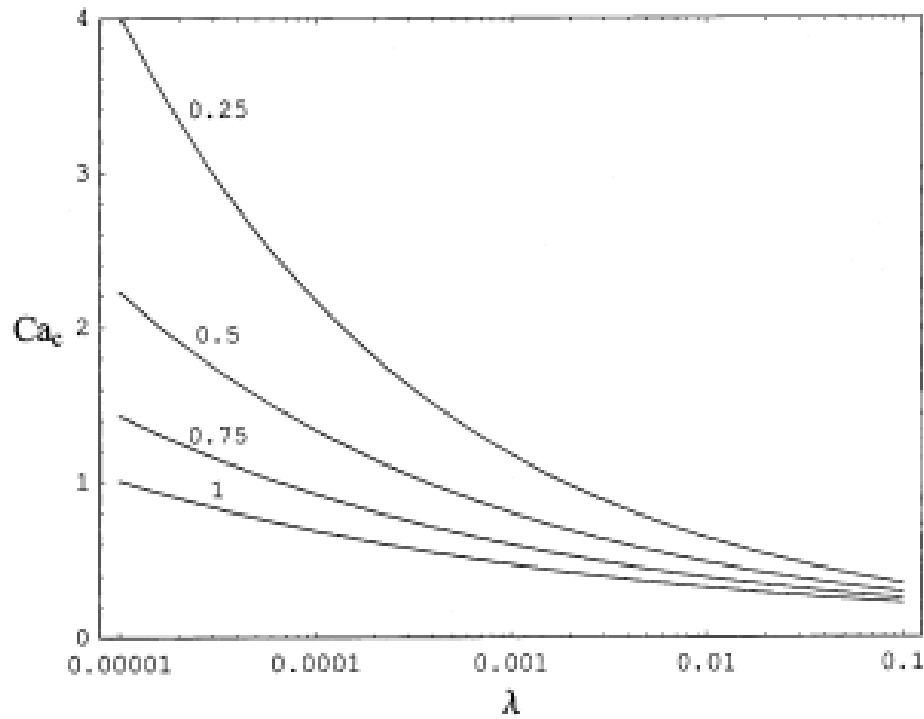


Figure 2.15 Critical Capillary Number vs viscosity ratio for a non-Newtonian drop in extensional flow (Favelukis et al., 2005).

2.3 Deformation and break up of drops and bubbles in complex viscous flows

While these correlations for bubble and drop breakup have been developed considering simple steady flows, it would be important to see if they hold in real process operations. For example, in mixing devices, the flow is complex and is often a mixture of shear, extension and possibly rotation.

For a given dispersion process, a knowledge of the dispersed phase size distribution and the flow type (shear and/or extension) is needed to characterize the flow during the bubble break up processes. Grace (1982), studied the dispersion of droplets in a Kenics static mixer. The measured average droplet size was used to back calculate an 'effective' shear rate for the dispersion process using the basic correlations of drop breakup in rotational (simple shear) and irrotational shear fields (pure elongation) (equations 2.40 to 2.43). For the case where the viscosity ratio was less than 1.0, the effective shear rate was calculated from shear correlations while for viscosity ratios greater than 4.0, it was calculated from the correlations for pure extension. This was because it was assumed that droplet breakup for systems with viscosity ratio $p > 4.0$ was possible only in extensional flow as was shown in figure 2.12. Figure 2.16 shows the comparison of the effective shear rate in both the cases. While the effective rotational shear rate was directly proportional to the nominal wall shear rate, the effective irrotational shear rate was found to be proportional to the square root of the nominal wall shear rate. The overall effective shear rate G_{eff} was calculated as:

$$G_{eff} = \frac{Ca_{cr} \cdot \sigma}{\mu \cdot r} \quad (2.51)$$

Bigio et al. (1998), experimentally studied drop breakup of Newtonian fluids in a supercritical couette shear flow apparatus and found the mean droplet size to be of the order of the maximum stable drop diameters predicted as:

$$d_{max} = \frac{2\sigma Ca_{cr}}{\mu G} \quad (2.52)$$

Drop breakup times (t) were measured for a range of viscosity ratios between 0.03 and 3. The drop breakup time was reduced to a dimensionless form using the shear rate (G) calculated analytically and was found to relate to the viscosity ratio p as:

$$tG = 26p + 25 \quad (2.53)$$

The measured drop breakup times were compared against an estimated stream time in a two dimensional cavity flow and a single screw extruder flow. Simple shear flow was assumed in both cases and the stream times were calculated from analytically estimated velocities. The aspect ratio and/or the screw helix angle affected the reduced stream times in the cavity. Goodbille and Picot (2000) studied breakup of viscoelastic and Newtonian drops in a convergent-divergent cell that provided a mixture of simple shear and elongation flow. Smaller drops deformed according to the Capillary number while drops greater than a certain size showed tail forming and tip streaming, leading to smaller droplets. Only qualitative analysis of drop deformation and mode of breakup was provided.

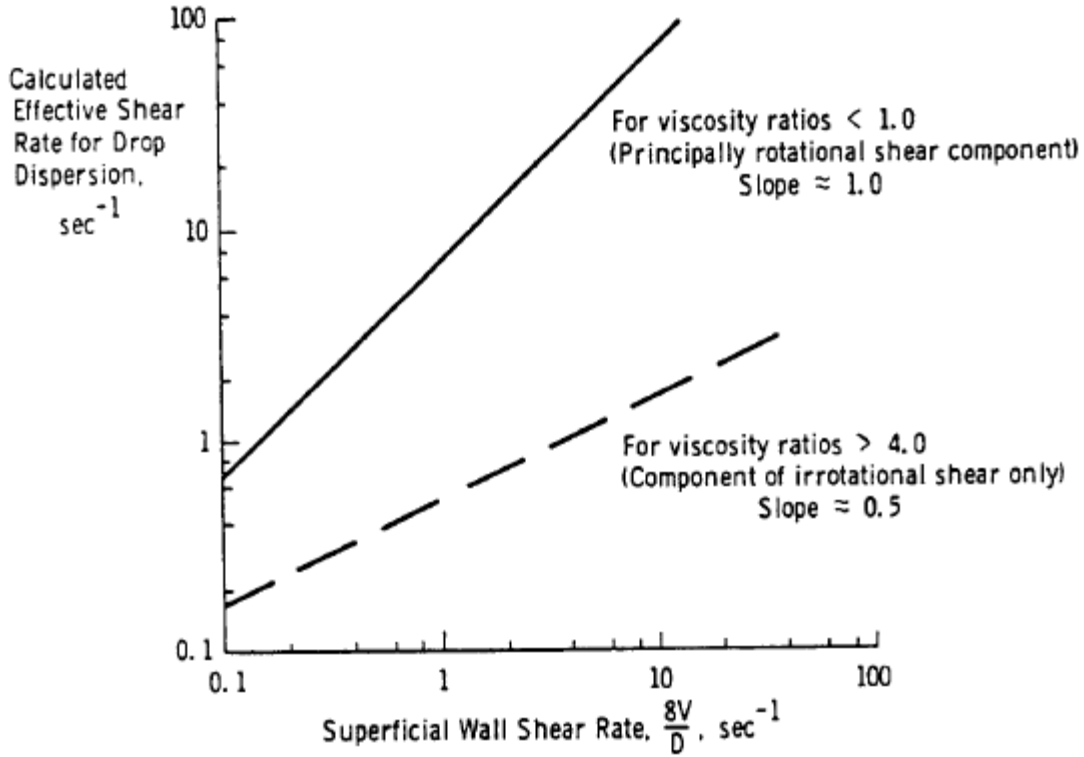


Figure 2.16 comparison of effective shear rates for drop dispersion at low and high viscosity ratios in a Kenics static mixer (Grace, 1982).

Das et al. (2005), modeled the maximum stable drop diameter for a dispersion process in an SMX static mixer which consists of mixing elements arranged in a tubular housing perpendicular to each other and the flow axis. The flow in the mixer was assumed to be analogous to flow in a set of parallel pores of diameter d_p with a stream velocity of U_p with the characteristic shear rate given by $4U_p/d$. The maximum stable diameter is then given by:

$$d_m = \frac{2\alpha d_p Ca_{crit}}{\mu_e U_p} \quad (2.54)$$

where σ is the surface tension and μ_e is the effective viscosity of the continuous phase. This equation is made dimensionless by introducing a pore viscosity number, Vi_p ($=\mu_e U_p/\sigma$). The correlation obtained from experimentally measured drop diameters and Vi_p (Figure 2.17) was used to predict a Ca_{crit} :

$$\ln\left(\frac{d_m}{d_p}\right) = \ln(2Ca_{crit}) - k \ln(Vi_p) \quad (2.55)$$

where Ca_{crit} and k were found to be 0.383 and 0.913 respectively, with the Ca_{crit} consistent with value obtained by Grace (1982). In both the cases (Das et al., 2005; Grace, 1982) the critical breakup condition was back calculated experimentally without prior knowledge of contribution of the flow type parameter α .

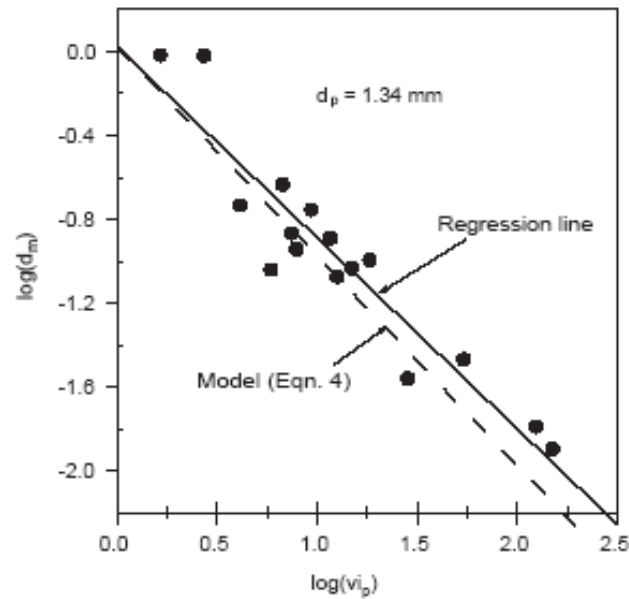


Figure 2.17: Correlation between dimensionless drop diameter and viscosity number for dispersion in SMX static mixer at low Reynolds number flow (Das et al., 2005).

2.4 Numerical Simulation of viscous mixing flows

Understanding and quantitatively characterizing flow profiles and mixing efficiencies (which lead to an initial understanding of the type of flows) is of fundamental importance to understand bubble deformation and break up phenomena in mixers and also have proven to be important for scale up and optimization of mixing equipment. Mixing flows have been studied numerically and experimentally in batch and continuous mixers of various geometries relevant to food processing such as the Banbury mixer, Brabender Farinograph (Connelly and Kokini, 2006a, 2006b; Prakash, 1996; Prakash, Karwe and Kokini, 1999 ; Prakash and Kokini, 1999; Prakash and Kokini, 2000), single (Connelly and Kokini, 2003; Connelly and Kokini, 2004; Dhanasekharan and Kokini, 2003; Dhanasekharan and Kokini, 2000) and twin-screw extruders (Cheng and Manas - Zloczower, 1997; Connelly and Kokini, 2007; Li and Manas - Zloczower, 1994; Li and Manas - Zloczower, 1995).

The mixing mechanisms occurring in food and polymer processing equipment can be broadly characterized into ‘dispersive’ and ‘non-dispersive’ (or extensive) (Wang and Manas - Zloczower, 2001). Dispersive mixing is defined as the reduction in size of a cohesive component within a continuous fluid. Examples include dis-agglomeration of solid particles and breakup of immiscible droplets and gas bubbles dispersed in a continuous fluid. Dispersion of agglomerates and drops in flow will require the application of enough viscous forces to overcome the interfacial forces holding the particles together. Non-dispersive or extensive mixing can be further categorized as ‘distributive’ or ‘laminar’. Distributive mixing is the process of material rearrangement

and is related to the material residence time distribution; whereas laminar mixing deals with the affine stretching and folding of material elements and is characterized by the strain distribution and length of stretch functions.

A review of the theoretical measures of viscous fluid mixing, the governing equations of viscous fluid flow and the numerical methods for simulating viscous fluid mixing flows is presented in this section (Vyakaranam and Kokini, 2011).

2.4.1 Theoretical measures of mixing

There are several measures to quantify distributive and dispersive mixing which are relevant to the characterization of flow types of relevance to bubble break up phenomena, as well as laminar stretching and folding of the material. During mixing of two components (distributive mixing) the homogeneity of the mixture can be quantified through the scale of segregation ($S(t)$) which is a measure of the binomial distribution of the components and is calculated as:

$$S(t) = \int_0^{\xi} R(r, t) dr \quad (2.56)$$

where $R(|r|)$ is a correlation coefficient that gives the probability of ' M ' pairs of material points in the mixer separated by a distance $|r|$ having the same concentration:

$$R(|r|) = \frac{\sum_{j=1}^M (c_j' - \bar{c}) \cdot (c_j'' - \bar{c})}{MS^2} \quad (2.57)$$

The parameter $S(t)$ gives an indication of the average size of the segregated regions but cannot detect local defects in flow.

When a cluster of material points is distributed, the difference between the actual distribution and the ideal distribution of the material points is called the “pairwise distribution index” or the “cluster distribution index”, ε and is calculated as

$$\varepsilon = \frac{\int_0^{\infty} [c(r) - c(r)_{ideal}]^2 dr}{\int_0^{\infty} [c(r)_{ideal}]^2 dr}, \quad (2.58)$$

where $c(r)$ is the coefficient of the probability density function and the value of the index ε varies from 0 (ideal distribution) to 1 (no distribution) (Connelly and Kokini, 2007).

The efficiency of a mixing flow to stretch and fold the material can be studied by using a kinematic approach wherein the deformation of infinitesimal material lines and surface elements is tracked (Ottino 1989). If the motion of the fluid is described by $\mathbf{x} = \chi(\mathbf{X}, t)$, and the deformation of an infinitesimal material line given by $d\mathbf{x} = \mathbf{F} \cdot d\mathbf{X}$ then the length of stretch, λ can be defined in terms of the strain as:

$$\lambda = \lim_{|d\mathbf{X}| \rightarrow 0} \frac{|d\mathbf{x}|}{|d\mathbf{X}|} \quad (2.59)$$

and a local instantaneous efficiency of mixing is given by:

$$e_{\lambda}(\mathbf{X}, \mathbf{M}, t) = \frac{D \ln \lambda / Dt}{(\mathbf{D} : \mathbf{D})^{\frac{1}{2}}} \quad (2.60)$$

where $\mathbf{M} = \frac{d\mathbf{X}}{|d\mathbf{X}|}$ and \mathbf{D} is the rate of strain tensor with a scalar magnitude of $(\mathbf{D} : \mathbf{D})^{1/2}$. If the material is an incompressible Newtonian fluid, then the local instantaneous efficiency is the fraction of dissipated energy that is used to stretch the material and has a range

between -1 and 1. The time averaged efficiency $\langle e_\lambda \rangle$ given in equation 2.61 gives information on the nature of reorientation (stretching and folding) of the flow. Flows with no reorientation will have $\langle e_\lambda \rangle$ decaying with time as t^{-1} , whereas $\langle e_\lambda \rangle$ tending to a constant value would indicate a flow with strong reorientation (Ottino, 1989).

$$\langle e_\lambda \rangle(\mathbf{X}, \mathbf{M}, t) = \frac{1}{t} \int_0^t e_\lambda(\mathbf{X}, \mathbf{M}, t') dt' \quad (2.61)$$

Similar efficiency for stretching of an infinitesimal area element can also be evaluated. In a chaotic time periodic flow, the arithmetic and geometric means of length of stretch grow exponentially and can be represented as:

$$\bar{\lambda} \approx \alpha \cdot e^{\Theta n}, \quad \langle \lambda \rangle \approx \alpha \cdot e^{\Lambda n} \quad (2.62)$$

where n is the number of periods of revolutions and Θ and Λ are the topological entropy exponent and the Lyapunov exponent respectively. While topological entropy is a measure of the mixing rate in chaotic regions of flow, the Lyapunov exponent gives a measure of the rate of elongation or stretching (Muzzio, et al., 2000; Zalc, et al., 2002).

Dispersive mixing involves breakup of agglomerates and drops in flow and is caused by stresses that are large enough to overcome the cohesive or interfacial forces that tend to keep the agglomerate or the drop intact. The viscous forces required for breakup depends on the type of flow, with elongational flows being more effective than flows with a rotational/shear component (Grace, 1982; Bentley and Leal, 1986).

Understanding and quantifying shear and elongational flows during mixing is non trivial. One method which offers some predictive ability is the dispersive ‘mixing index’, λ_{MZ} which quantifies the relative strength of the elongational flow component and can be defined as:

$$\lambda_{MZ} = \frac{|\mathbf{D}|}{|\mathbf{D}| + |\mathbf{\Omega}|} \quad (2.63)$$

where \mathbf{D} and $\mathbf{\Omega}$ are the rate of deformation and vorticity tensors respectively (Yang and Manas-Zloczower, 1992). λ_{MZ} ranges from 0 for pure rotation to 0.5 for simple shear to 1.0 for pure elongation. The Manas-Zloczower mixing index defined above is not frame invariant. However, several other flow type parameters that are frame invariant were found to be computationally difficult to evaluate due to the requirement of higher mesh densities in the simulation while providing similar information as the non-frame invariant index (Wang and Manas-Zloczower, 2001; Connelly, 2004). The relationship between the flow type parameter, α and mixing index, λ_{MZ} , can be deduced from equations (2.29) and (2.63) as follows:

$$\lambda_{MZ} = \frac{1 + \alpha}{2} \quad (2.64)$$

The range of values of λ_{MZ} and α for corresponding flow types are shown in table 2.1

Flow Type	α	λ_{MZ}
Pure Rotation $ \mathbf{D} = 0$	-1	0
Simple Shear $ \mathbf{D} = \mathbf{\Omega} $	0	0.5
Pure Extension $ \mathbf{\Omega} = 0$	1	1

Table 2.1: Comparison of values of flow type parameter, α and mixing index, λ_{MZ}

2.4.2 Governing equations for calculation of flow

The velocity and pressure distributions for an incompressible and isothermal fluid flow are calculated from the Navier-Stokes equations of mass and momentum conservation:

$$\nabla \cdot \mathbf{v} = 0 \quad (2.65)$$

$$\nabla \cdot \boldsymbol{\sigma} + \rho \mathbf{f} = \rho \left(\frac{\partial \mathbf{v}}{\partial t} + \mathbf{v} \cdot \nabla \mathbf{v} \right) \quad (2.66)$$

where ρ is the fluid density and \mathbf{f} is the external body force per unit mass.

The stress tensor $\boldsymbol{\sigma}$ given in equation 2.65 incorporates the isotropic pressure (P) and the extra stress tensor (\mathbf{T}) and can be defined as:

$$\boldsymbol{\sigma} = -P\mathbf{I} + \mathbf{T} \quad (2.67)$$

An additional energy conservation equation has to be solved in the case of a non-isothermal flow to obtain the temperature distribution:

$$\rho C(T) \cdot \left(\frac{\partial T}{\partial t} + \mathbf{v} \cdot \nabla T \right) = \mathbf{T} : \nabla \mathbf{v} + r - \nabla \cdot \mathbf{q} \quad (2.68)$$

where $C(T)$ is the dependence of heat capacity on temperature, T , r is the volumetric heat source, \mathbf{q} is the heat flux and $\mathbf{T} : \nabla \mathbf{v}$ represents viscous heating.

The extra stress tensor of equation 2.66 for a generalized Newtonian fluid in an isothermal flow is given by:

$$\mathbf{T} = 2\mu \mathbf{D} \quad (2.69)$$

where \mathbf{D} is the rate of deformation tensor and μ is the viscosity of the fluid. In a complex flow, the local shear rate, $\dot{\gamma}$ is calculated as:

$$\dot{\gamma} = \sqrt{2II_D} \quad (2.70)$$

where II_D is the second invariant of the rate of deformation tensor \mathbf{D} calculated as:

$$II_D = \text{tr}(\mathbf{D}^2) \quad (2.71)$$

The extension rate, $\dot{\epsilon}$ is derived from the second and third invariants of the rate of deformation tensor as:

$$\dot{\epsilon} = 6 \cdot \frac{III_D}{II_D} \quad (2.72)$$

The third invariant of the rate of deformation tensor III_D is calculated as:

$$III_D = \det(\mathbf{D}) \quad (2.73)$$

The simplest form of the viscosity function is for a Newtonian fluid, when it reduces to a constant value μ_0 , called the Newtonian or zero-shear-rate viscosity.

For viscoelastic fluids, the extra stress tensor \mathbf{T} is divided into a viscoelastic (\mathbf{T}_1) and a purely viscous (\mathbf{T}_2) given by:

$$A(\mathbf{T}_1, \lambda_t) \cdot \mathbf{T}_1 + \lambda_t \frac{\delta \mathbf{T}_1}{\delta t} = 2\eta_1 \mathbf{D}, \quad \mathbf{T}_2 = 2\eta_2 \mathbf{D} \quad (2.74)$$

where the relaxation time λ_t , the viscosity factor η_1 and the function $A(\mathbf{T}_1, \lambda_t)$ depend on the specific viscoelastic model used.

The common differential viscoelastic models used to describe polymeric food materials are Oldroyd-B, Maxwell, White-Metzner, Phan-Thien-Tanner and the Giesekus models (Connelly, 2004).

2.4.3 Numerical methods for simulation of mixing flows

For a given system of fluid and a mixing geometry, the solution of the above set of equations consisting of the conservation of mass and momentum, the energy equation (for non-isothermal problems) and the appropriate constitutive equation can be obtained by several numerical techniques. The Finite Element Method (FEM) has been the most commonly used technique to approach numerical simulation of viscous mixing flows, even though other methods such as the Finite Difference Method and the Finite Volume Method have been used. (Dhanasekharan and Kokini, 2003; Connelly and Kokini 2003; Heniche and Tanguy, 2008)

Solving a mixing flow using the FEM technique involves three main steps:

- construction of the flow volume (or the domain of the problem) into a mesh made up of several finite elements or sub domains;
- derivation of algebraic equations relating the physical quantities between the element nodes;
- solving for the whole flow domain by assembling the equation parts using continuity and/or balance of physical quantities across the elements (Reddy, 2006).

The mesh generation step requires the construction of mesh in the mixing flow domain geometry using a network of linear triangular and quadrilateral elements (2D) or hexahedral, prism, tetrahedron and wedge elements (3D). Several Computational Fluid Dynamics (CFD) software suites include mesh generation software, for example, the Gambit (Ansys Inc., Lebanon, NH) mesh generator. While maintaining the coarseness of the mesh is important to keep the computational costs low, a higher density of finer mesh

elements is needed in areas involving high gradients of flow properties. Hence, it is important to strike a balance with the coarseness/fineness of the mesh depending on the available computational capabilities. Additionally, for a higher accuracy and quicker convergence of the solution, the transition from coarser to finer mesh element regions has to be smooth and the individual elements have to be as close as possible to ideal shapes (Connelly, 2004; Heniche and Tanguy, 2008). In the next step, the governing equations of motion are discretized using a weighted residual method and approximation of the flow variables for each element. For a generalized Newtonian fluid, the velocity, pressure and stress fields (in case of viscoelastic flows) are approximated using the equations:

$$\mathbf{v}^h = \sum \mathbf{V}^i \psi_i \quad (2.75)$$

$$p^h = \sum p^i \pi_i \quad (2.76)$$

$$\mathbf{T}^h = \sum \mathbf{T}^i \phi_i \quad (2.77)$$

where ψ_i , π_i and ϕ_i are called the finite element basis functions and V_i , p_i and T_i are nodal variables.

There are several methods to discretize the governing equations, for example the Galerkin method, the Pressure Stabilized Petrov Galerkin method and the Galerkin Least-square method. In the Galerkin method, assuming the inertia terms to be negligible, the set of finite element equations in the flow domain, Ω are formulated as:

$$\int_{\Omega} \pi_k [\nabla \cdot \mathbf{v}^a] d\Omega = 0 \quad (2.78)$$

$$\int_{\Omega} \{ \psi_j \rho \left[\frac{D\mathbf{v}^a}{Dt} - \mathbf{f} \right] + \nabla \psi_j^T \cdot [-p^a \mathbf{I} + 2\eta^2 \mathbf{D}^a + \mathbf{T}_1^a] \} d\Omega = \int_{\Omega} \psi_j \boldsymbol{\sigma} \cdot \mathbf{n} ds \quad (2.79)$$

$$\int_{\Omega} \phi_i [g(\mathbf{T}_1) \cdot \mathbf{T}_1^a + \lambda \frac{\partial \mathbf{T}_1}{\partial t} - 2\eta_1 \mathbf{D}^a] d\Omega = 0 \quad (2.80)$$

For differential viscoelastic models, this system of equations can be solved by using a coupled method where the extra stress tensor is the primary variable along the pressure and velocity fields and the Newton-Raphson technique can be used to solve for the variables. In this method, one usually encounters large number of unknowns and high computational costs. Another method often used is the decoupled method where the viscoelastic stress tensor is computed separately from the flow kinematics which is iterated using the Picard's scheme. The accuracy and stability of the Galerkin formulations deteriorates in viscoelastic flow problems as the elasticity number increases and further stabilization techniques such as the Streamlined Upwind (SU) and the Elastic-Viscous-Stress Splitting (EVSS) are needed. The reader is directed to Connelly (2004) and the references therein for a detailed review of these techniques.

Several commercial FEM simulation packages are available, such as FIDAP (Ansys, Inc.), AcuSolve (Acusim Software), Polyflow (Ansys) and Poly3D (Rheosoft). In particular, the Polyflow suite, which includes a mesh generator (Gambit), an FEM solver (Polyflow) and a post-processor (FLPost/Fieldview/CFX Post) has been extensively used by our group to simulate viscous and viscoelastic flows in mixers and extruders. A typical flow problem would include the following steps: building the mixer geometry and converting it into an FEM mesh using the mesh generator, Gambit; defining the flow boundaries, material properties, numerical parameters and operating conditions using the Polydata interface; solving for velocity profiles using the FEM solver, Polyflow; calculating the various mixing measures from the velocity data using a post processor, FLPost/Fieldview.

Simulation of mixers with geometry varying continuously with time, as in the case of moving impellers or screw/paddle elements, requires special meshing techniques. One approach that can be applied to a single impeller or a single screw mixer is the ‘rotating reference frame technique’ in which the impeller/screw is taken as the fixed reference frame with the barrel rotating around it. This enables the flow domain mesh to be fixed in time. The velocities are then transformed back to the inertial reference frame. In case of asymmetrical mixer geometries such as in the case of an eccentrically placed impeller or a twin screw continuous mixer design, a ‘mesh superposition technique’ (MST) can be used in which the impeller or the screw/paddle elements are meshed separately from the flow domain and then superimposed (Connelly and Kokini, 2006). In such a case, the equation of motion is modified by the introduction of a penalty term H to distinguish the solid (impeller or paddle) mesh elements from the fluid elements:

$$H(\mathbf{v} - \bar{\mathbf{v}}) + (1 - H)(-\nabla P + \nabla T + \rho \mathbf{g} - \rho \mathbf{a}) = 0 \quad (2.81)$$

The penalty term H is essentially a step function and is set to a value of 1 for all nodes on solid moving parts and a value of 0 for all nodes in the fluid volume. The continuity equation is also modified with a relative compression factor β in order to account for conservation of mass in the regions of flow domain covered by the moving solid elements

$$\nabla \cdot \mathbf{v} + \frac{\beta}{\mu} \Delta P = 0 \quad (2.82)$$

2.5. Recent advances in 3D Numerical simulation of model mixing geometries

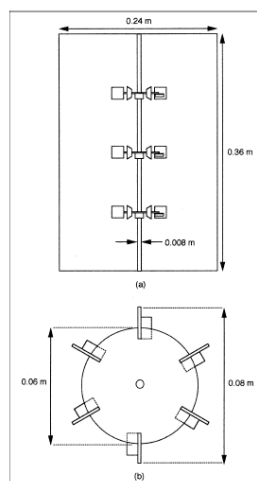
In this section, a review of the application of numerical simulation techniques in evaluating the efficiency of distributive and dispersive mixing in model batch and continuous mixing geometries involving viscous liquids is presented. The subject of these studies was to study the effect of the mixer operating parameters like screw design, screw speed and material rheology on the variations in flow and mixing profiles and efficiencies. These studies give us useful information related to the type of flows that are observed in various mixer geometries. These types of flows, in turn, would have different propensity to deform and break bubbles.

Recent studies in the area of numerical simulation and computational fluid dynamics of mixing processes can be broadly classified based on the mixing geometries investigated : stirred tank reactors (Zalc, et al., 2001; Alvarez-Hernández et al., 2002; Zalc et al., 2002; Rivera et al., 2004; Barailler et al., 2006; Iranshahi et al., 2006; Rivera et al., 2006; Iranshahi et al., 2007), Dough kneaders (Jongen 2000; Jongen et al., 2003; Connelly and Kokini, 2004; Connelly and Kokini, 2006; Connelly and Kokini, 2007), static mixers (Rauline et al., 2000; Zalc et al., 2002; Zalc et al., 2003; Heniche et al., 2005) and continuous mixers/extruders (Dhanasekharan and Kokini, 2000; Wang and Manas-Zloczower, 2001; Dhanasekharan and Kokini, 2003). These studies have been reviewed in detailed by Vyakaranam and Kokini (2011).

2.5.1 Stirred tank reactors/batch mixers

Mixing of viscous liquids in stirred tank reactors and impeller based batch mixers is widely employed in many process industries where effective distribution of additives is of great importance. Impeller design and the speed of the impeller (as quantified by the Reynold's number, Re) can be varied to attain optimum mixing conditions and power efficiency. Figure 2.18 shows a few of the impeller designs used in stirred tank reactor and impeller based mixers. The geometrically simple and symmetric construction of the impellers coupled with a relatively large flow volume in the reactor/vessel (usually cylindrical) makes these mixers an excellent subject for use of computational fluid dynamics in the calculation and visualization of the various mixing measures as well as their validation using imaging techniques like the particle image velocimetry (PIV). (Zalc et al., (2001) and Zalc et al., (2002) used the ORAC CFD package (Dantec Dynamics, Mahwah, NJ) to study the laminar mixing in a three-Rushton turbine stirred tank reactor (Figure 2.18a) and validated the flow measurements with PIV experiments using planar laser induced fluorescence. Figure 2.19 shows the simulation results to be in excellent agreement with the experiments in revealing the size and location of poorly mixed regions in the mixer. Local mixing efficiency can be quantified and visualized by computing the stretching value, λ . The stretching value is calculated from deformation of infinitesimal vectors in the flow which usually takes place at an exponential rate in chaotic flow regions as compared to a linear rate in non-chaotic flows. The contour maps of the logarithm of stretching shown in Figure 2.20 reveal the spatial heterogeneity of stretching for mixing at various impeller speeds after 20 revolutions. Knowledge of the

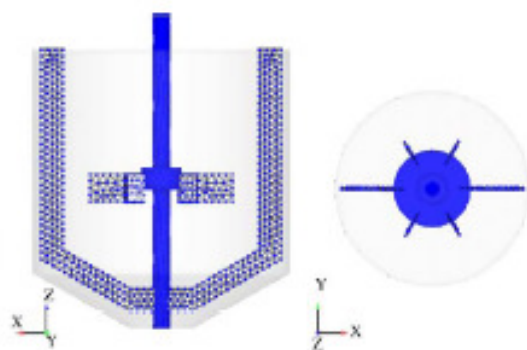
distribution patterns of stretching could be valuable in deciding the injection point for additives for optimal distribution (Zalc et al., 2002).



(a)



(b)



(c)

Figure 2.18 Examples of impeller designs in batch mixers (a) Three-Rushton turbine (Zalc et al., 2001) (b) Paravisc impeller (Iranshahi et al., 2006) (c) Rushton turbine with a co-axial anchor (Rivera et al., 2006).

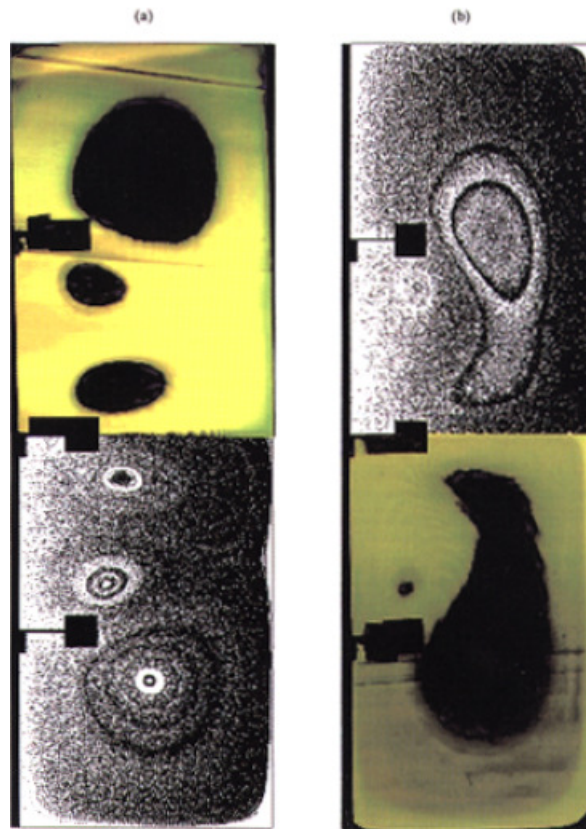


Figure 2.19 Comparison of experimental and simulated results show excellent agreement in revealing the mixing patterns in a three turbine Rushton impeller mixer after 600 revolutions at (a) $Re = 20$ and (b) $Re = 40$ (Zalc et al., 2002).

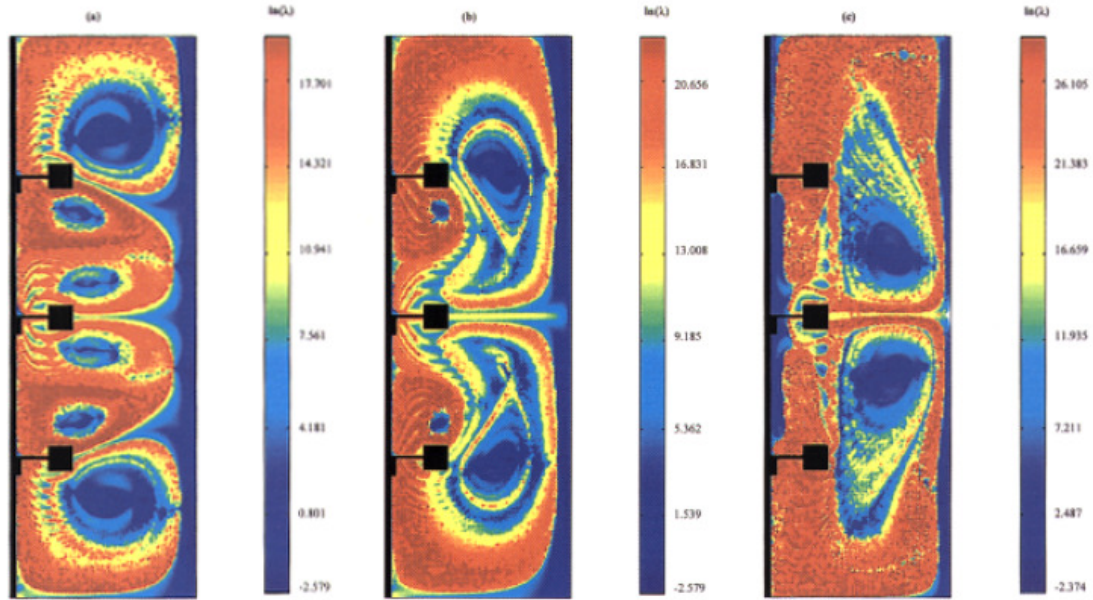


Figure 2.20 Contour plots of $\ln(\lambda)$ reveal the spatial heterogeneity of stretching at various impeller speeds (a) $Re = 20$ (b) $Re = 40$ (c) $Re = 160$ (Zalc et al., 2002).

In order for a mixing process to deliver optimum distributive and dispersive mixing, the full set of operating conditions needs to be considered. These include impeller design, impeller speed, fluid rheology and the injection point for additives. While comparing the mixing performance of an Ekato Paravisc impeller with a Double Helical Ribbon (DHR) impeller (Figure 2.18 (b)), Iranshahi et al., (2006) showed that the Paravisc impeller was more sensitive to the choice of an injection point for the tracer in the effective distribution of the tracer particles in a Newtonian fluid (Figure 2.21).

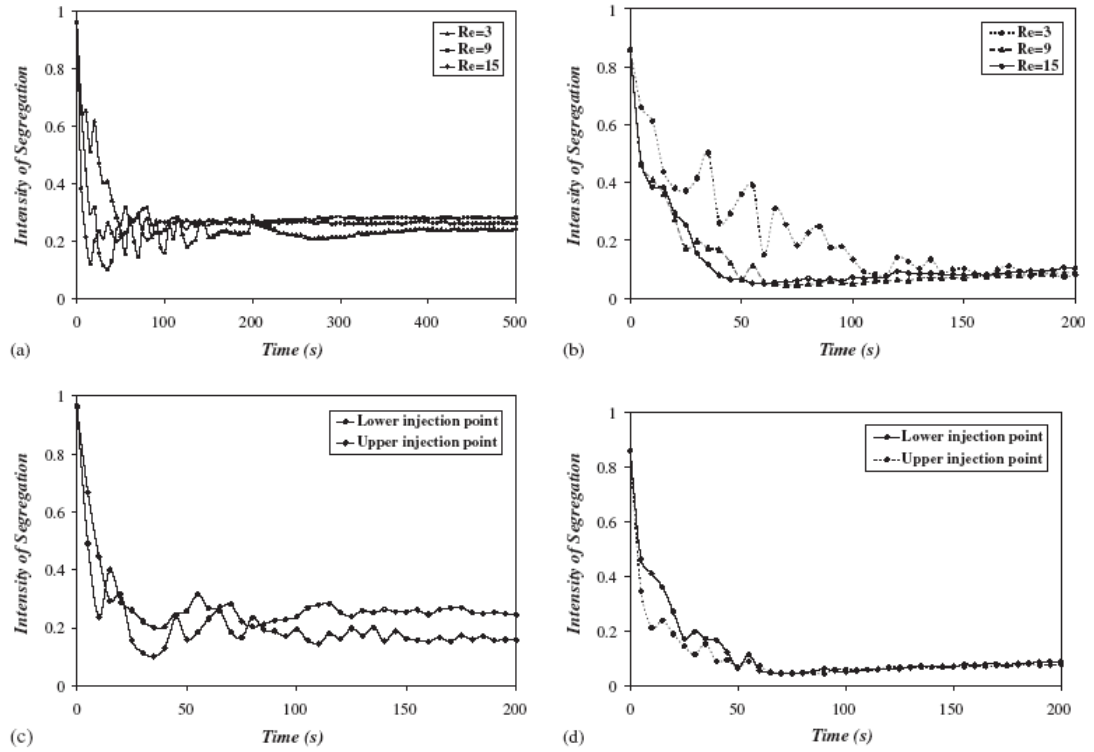


Figure 2.21 Intensity of segregation vs. time for different Re and points of injection of the tracer (Iranshahi et al., 2006).

An important criterion for many mixing processes is the balance between distributive and dispersive mixing. Rivera et al. (2006), defined a parameter that is a ratio between two dimensionless quantities, the ‘head number’ N_h , (representing the shearing ability of the impeller) and the ‘flow number’ N_q (representing the pumping ability of the impeller). The effect of an anchor co-rotating and counter-rotating with a Rushton turbine (Figure 2.18 (c)) was studied for a Newtonian and a non-Newtonian fluid by simulating the flow and mixing using the POLY3DTM(Rheosoft, Inc.) finite element software. It can be seen from Table 2.1 that the co-rotating anchor was more effective in combined distribution and dispersion while the counter-rotating anchor was poor at distribution. The poor distributive mixing by the counter-rotating mode can be visualized in Figure

2.22 which shows the intensity of segregation of tracer particles (a measure of the homogeneity of the mixing) at two different mixing times. The authors (Rivera, Foucault et al. 2006) refer to this figure as ‘tracer dispersion’, whereas the actual process measured by the intensity of segregation is distributive mixing. Dispersive mixing in our definition relates to the breakup (for example, of tracer drops) caused by the shearing action of the impellers. The rheology of the fluid also affected the efficiency of the mixing process in that the shear thinning of the viscosity resulted in smaller well-mixed areas.

Operating conditions	N_q	N_h	N_h/N_q
Co-rotating Newtonian fluid	0.917	1.546	1.685
Rushton impeller only Newtonian fluid	0.658	1.474	2.477
Counter-rotating Newtonian fluid	0.756	1.631	1.948
Co-rotating non-Newtonian fluid	0.761	0.865	1.136
Rushton impeller only non-Newtonian fluid	0.452	1.082	3.222
Counter-rotating non-Newtonian fluid	0.608	1.457	1.778

Table 2.1 Comparison of the shearing and pumping abilities of the co-axial mixer for different rotating modes and fluid rheology (Rivera et al., 2006).

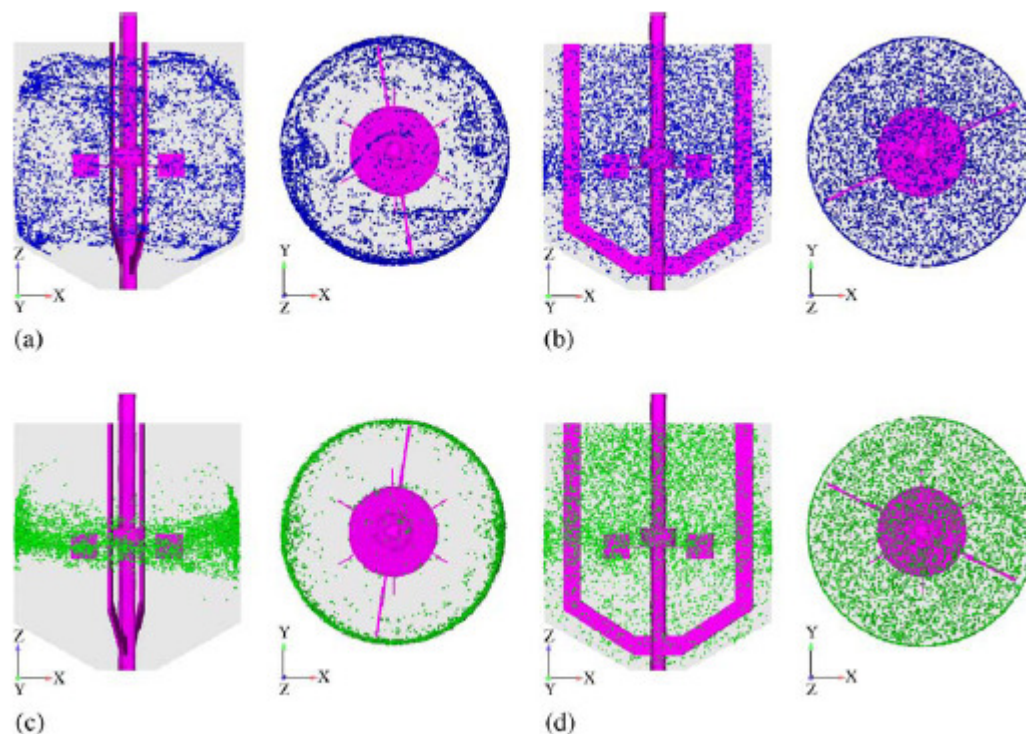


Figure 2.22 Distributive mixing in a rushton turbine impeller with a co-axial anchor (a) co-rotating after 15s (b) co-rotating after 150s (c) counter-rotating after 15s (d) counter-rotating after 150s (Rivera et al., 2006).

2.5.2 Dough mixers and kneaders

Dough kneaders and mixers are designed for highly viscous doughs and batters that require actions that include pushing portions of the material through other portions, elevating, dropping and rotating the material and cutting or dividing the material (Connelly, 2004). Most dough mixers are built to operate horizontally and typically use co-rotating twin blades or arms such as rollerbar, single and twin sigma blade, open paddle-4 way, double arm and spindle geometries. However, several smaller batch dough

kneaders with Z blades, sigma blades or rotating arms are used for empirical dough testing in laboratories. Examples include the plastograph (also known as the farinograph) which has two counter-rotating, but non-intermeshing blades inside a closed cavity, the do-corder which has two intermeshing blades co-rotating in a bowl with a low clearance with the wall, the planetary mixer (or the mixograph) in which the mixing is caused by the planetary motion of a rotating arm attached with a pair of vertical pins on either end and an Eberhart spiral mixer with a spiral rod rotating in a bowl (Jongen et al., 2003) (Figure 2.23).

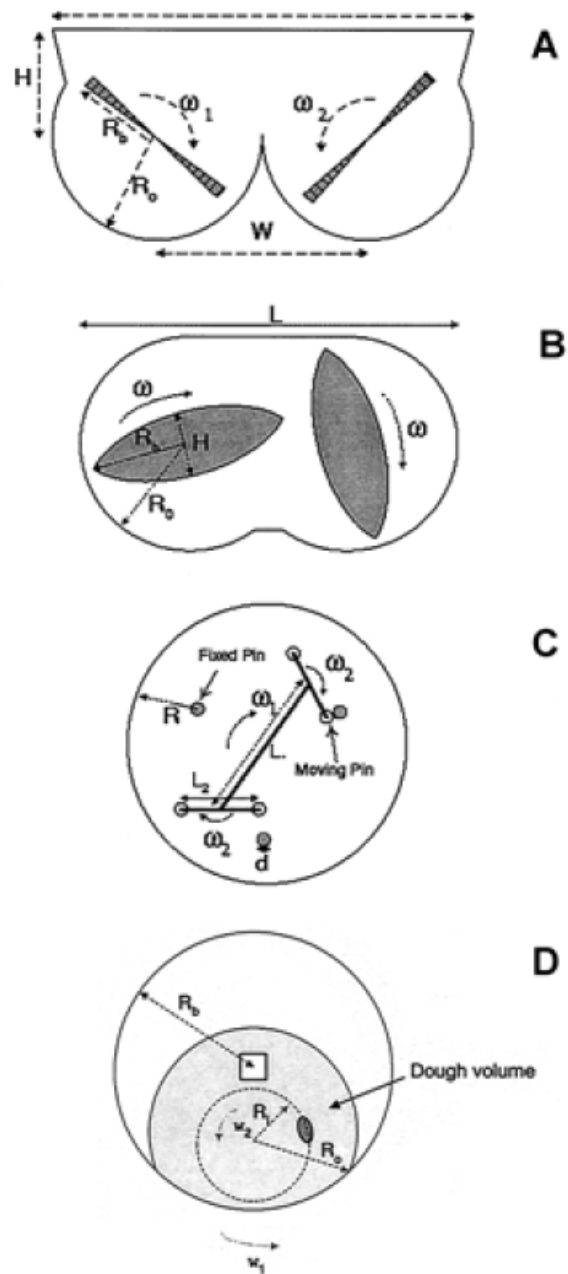
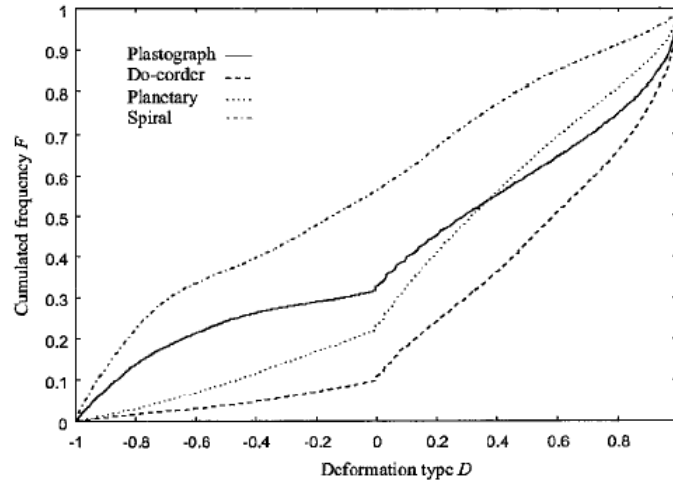


Figure 2.23 Dough kneaders of various geometries (a) Farinograph (b) Do-corder (c) Mixograph (d) Spiral mixer (Jongen et al., 2003) .

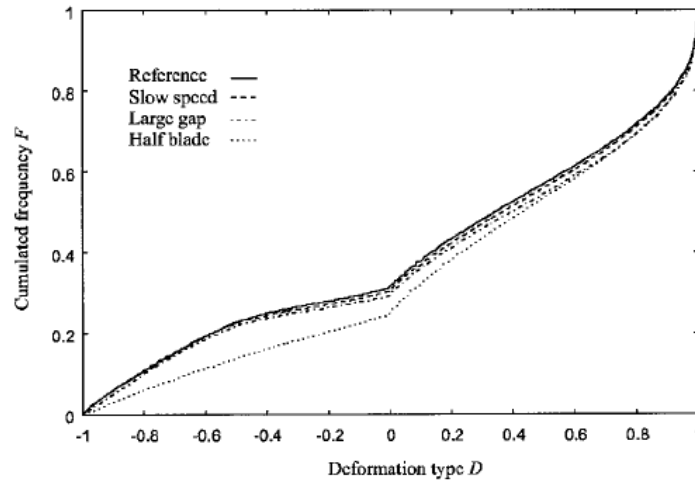
Research aimed at optimizing batch kneaders involves experimental methods relating the operating parameters to dough development, rheology and sensory quality of the product. Only a few studies were able to gather specific information on the flow profiles and mixing parameters due to the inherent experimental difficulties (Prakash et al., 1999; Prakash and Kokini, 2000). However, due to the recent advances in the design and simulation capabilities of various CFD software specifically aimed at viscous and viscoelastic flows, it is now possible to obtain detailed information of flow and mixing parameters that include distribution, dispersion and laminar stretching in dough mixing. Jongen et al. (2003), used a finite element simulation method to study the deformation of viscous pastes in four different batch mixing geometries (Figure 2.23). The technique involved superimposing the moving elements on the flow domain FEM mesh with the FIDAP (Fluent Inc., Lebanon, NH) FEM software. In order to quantify the deformation of the material a flow parameter R^2 was defined as the ratio of the second invariants of the shear rate and vorticity rate tensors. The normalized value of R^2 was calculated as:

$$D = \frac{1 - R^2}{1 + R^2} \quad (2.83)$$

A comparison of the cumulative time-averaged frequency function for the three types of the mixers (Figure 2.24) showed the spiral mixer to have the most rotational flow, the do-corder with the most elongational flow character, the planetary mixer and the plastograph provided approximately highest shear to the material. An investigation of the same parameter at different operating conditions of the plastograph shows that while rotational speed of the blades and gap clearance do not affect the type of deformation (the value of D), a change on the blade design does help in reducing the rotational character of the mixing profile.



(a)



(b)

Figure 2.24 (a) Cumulative distribution of mean flow type parameter, D for various kneader geometries (b) Cumulative distribution of mean flow type parameter, D for a farinograph at different blade configurations and speed (Jongen et al., 2003).

A more in-depth and detailed analysis of the 3D flow and mixing profiles in the Brabender® farinograph was performed by Connelly and Kokini (2006) using a mesh-superposition technique (MST) in which the moving sigma blades and the barrel volume

were separately meshed and superimposed. A finite element method (FEM) along with the MST was implemented in the Polyflow® computational fluid dynamics software (Fluent Inc., Lebanon, NH). Figure 2.25 shows the effect of fluid rheology on the velocity contour maps on the vertical center plane between the two blades. Increased shear thinning of the fluid caused a decrease in the velocity of the fluid right above the blades. The dispersive mixing ability was calculated as defined by Equation 2.63. A histogram of the distribution of the dispersive mixing index λ in the central planes between the farinograph blades for the three fluids shows decrease in elongation flow regions decreases with increasing shear thinning. The paths of material points can be calculated from the velocity profiles which can then be used to evaluate the distributive and stretching efficiency parameters such as the cluster distribution index, scale of segregation and the mean length of stretch. The density of probability of the length of stretch experienced by 10,000 infinitesimal material lines in the farinograph (Figure 2.26) for three revolutions of the blades showed a gradual and steady increase in the amount of material undergoing effective stretching over time.

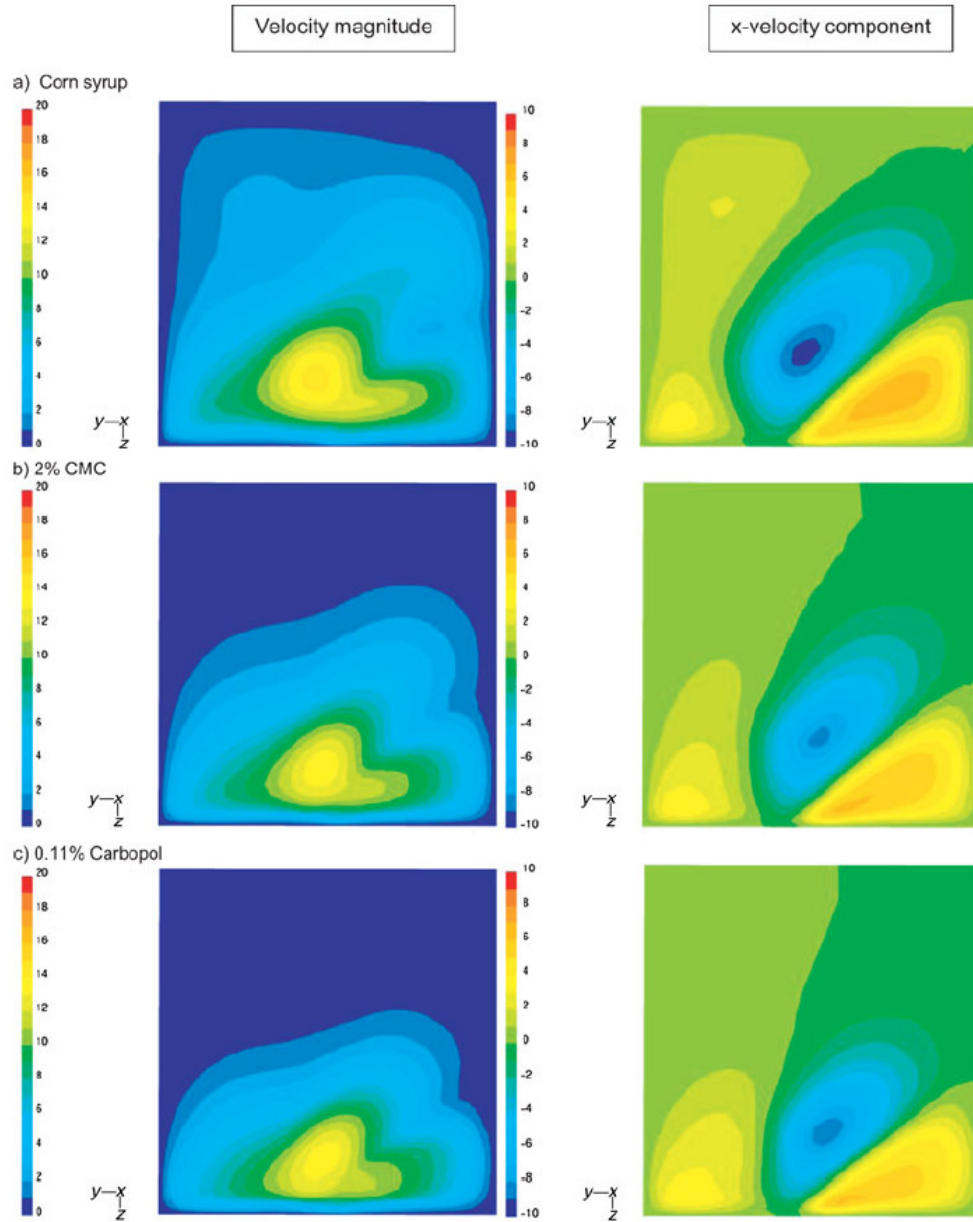


Figure 2.25 Effect of fluid rheology on the velocity profiles in the vertical center plane of the Farinograph(Connelly and Kokini, 2006).

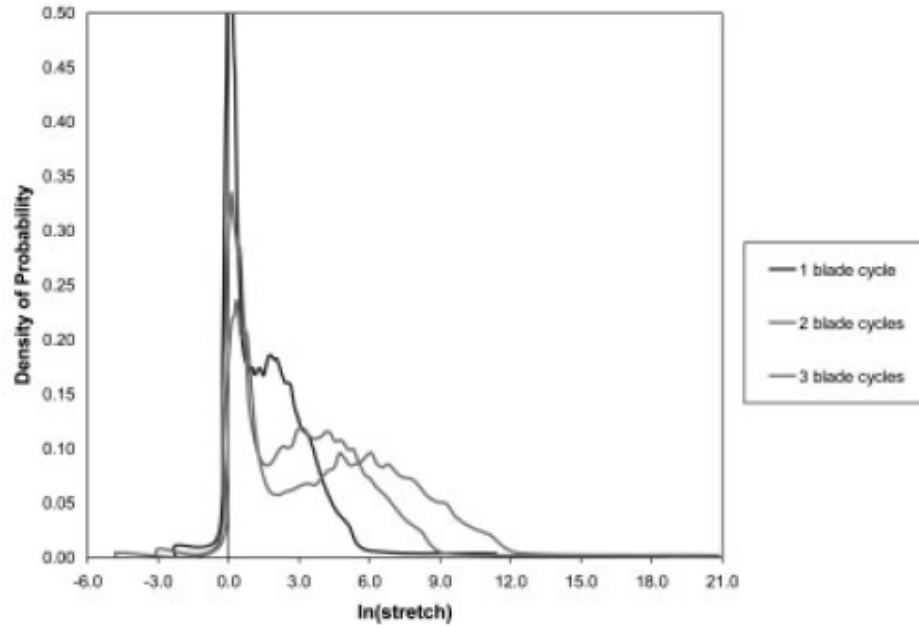


Figure 2.26 Density of probability of the length of stretch, $\ln(\lambda)$ experienced by 10,000 infinitesimal material lines in the farinograph (Connelly and Kokini, 2006).

Limited work has been done towards studying the effect of viscoelasticity of the fluid on the flow and mixing profiles. Connelly and Kokini (2003), simulated the flow of a Phan-Thien Tanner fluid model in a 2D single screw mixer using a rotating reference frame technique and compared different methods of handling the instabilities in dealing with a differential viscoelastic fluid model. It was found that the effect of viscoelasticity (increase in the relaxation times) was to create asymmetry in the velocity and pressure profiles and reducing the effects of shear thinning on the pressure and stresses (Figure 2.27).

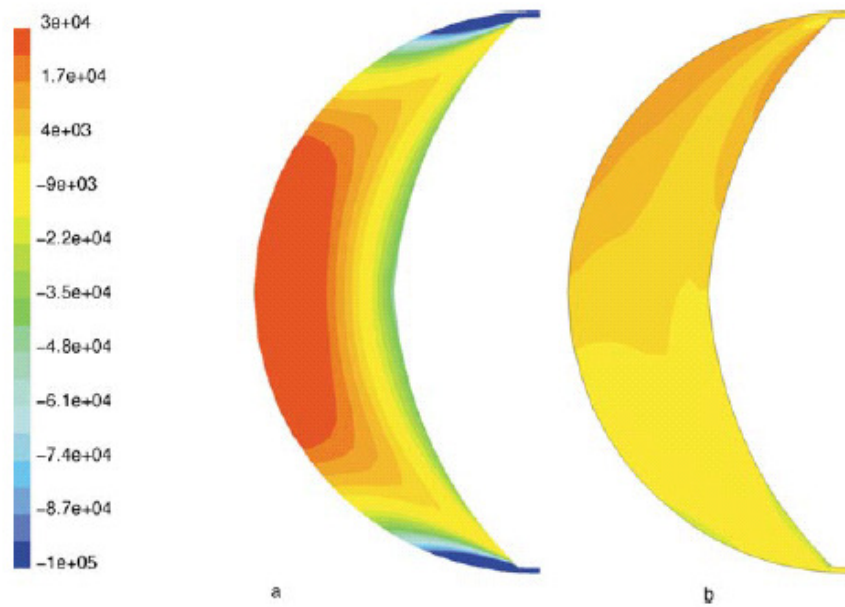


Figure 2.27 Shear stress (g/cm^2) contour maps for fluid with relaxation times (a) 0s and (b) 100s in a 2D single paddle mixer (Connelly and Kokini, 2003).

2.5.3 Continuous mixers and extruders

FEM simulations of viscous flow have been used to study effect of screw and mixing element geometry on local velocities and dispersive mixing efficiency in the mixing region of twin screw extruders. The use of 30° reverse staggered (left-handed) kneading blocks in a co-rotating twin screw extruder increased the ratio of local backflow to forward flow fivefold when compared to a 30° forward staggered (right-handed) configuration. The small back flow in the forward configuration was attributed to a block up action caused by the adjacent kneading block while this effect was greatly enhanced in the reverse stagger due to the formation of a reverse flow channel on the surface (Gotsis

et al., 1990; Lawal and Kalyon, 1995). This was an initial attempt to use FEM to simulate velocity profiles in a twin screw mixer. The study stopped at measuring velocity values and reported only velocity contours. With developments such as mesh superposition and more powerful numerical techniques it is appropriate to revisit the prediction of flow profiles and mixing efficiencies amongst kneading elements as a function of stagger angle. Yang and Manas-Zloczower (1992), calculated the velocity profiles for a power law fluid in the kneading section of a ZSK-30 twin-screw intermeshing continuous extruder using the FIDAP finite element package. In order to account for the moving elements, separate barrel volume meshes were created for every 15° rotation of the kneading discs. Given the symmetry of the rotors, analysis of the first six steps of this sequence was deemed sufficient to represent one full rotation of the kneading discs.

The dispersive mixing efficiency was evaluated in terms of the shear stresses generated and a dispersive mixing parameter, λ_{MZ} which quantifies the ratio of elongation flow to the shear flow as defined in equation 2.63. The value of λ_{MZ} ranges from 0 for pure rotation to 0.5 for simple shear to 1.0 for pure elongation. It was found that the average value of the shear stresses and λ_{MZ} in the overall kneading block region were not significantly affected by the stagger angle in the kneading elements, with most of the flow showing a simple shear character.

Local variations in the dispersive mixing efficiency within the kneading block region were not reported. More work is needed in this area because variations caused in the flow profiles and dispersive mixing indices as a function of the relative position of the kneading discs has not been addressed and is likely to affect the dispersion of particles travelling through the mixer volume.

A comparison of flow profiles, dispersive mixing index and shear stresses in the conveying screw and the kneading block regions were reported for an LSM30.34 twin screw extruder operating in the co-rotating and counter-rotating modes at different screw rotation speeds (Li and Manas-Zloczower, 1994). It was concluded that shearing discs did not provide a significant improvement in dispersive mixing, which could be improved by introduction of kneading or mixing elements (Figure 2.28).

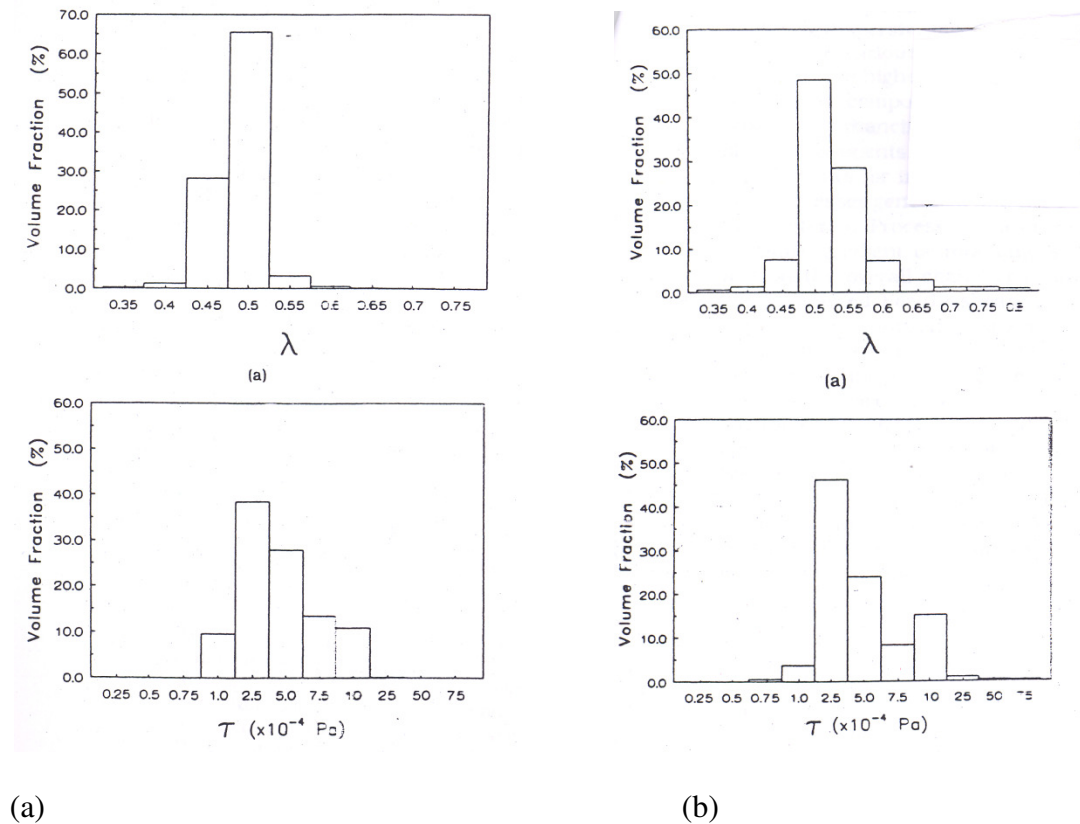


Figure 2.28. Volumetric distributions of λ_{MZ} and shear stress for (a) conveying elements and (b) shearing discs in a twin screw extruder (Li and Manas - Zloczower, 1994).

Yao and Manas-Zloczower (1998) analyzed the effect of screw configuration on the flow profile and dispersive mixing in an LCMAX 40 axial discharge continuous

mixer using the FIDAP CFD analysis package. A series of ‘pushing’ and ‘counter-pushing’ units, that had screw design that was a hybrid between kneading blocks and fully-flighted conveying screws, were arranged in series to create various configurations. Higher average values of shear stress were reported for configurations which had two counter pushing units while the cross-section plane between a pushing and a counter-pushing unit showed significantly higher values of both shear stresses and λ_{MZ} , especially in the intermeshing region. The study on the effect of design of the individual kneading discs in a 5 element kneading block on the dispersive mixing efficiency of a twin extruder showed that the three-lobe discs of a ZSK-53 extruder produced higher values of shear stresses and dispersive mixing index compared to the two-lobed discs of the ZSK-30 extruder. While the former had the three-lobed discs staggered at an angle of 30° , the latter had the two-lobed discs staggered at a forward 45° angle (Cheng and Manas-Zloczower, 1997).

The mixing efficiency is also affected by the individual paddle element width and the increase in the number of gaps between the elements, as a result of increasing the number of elements. Figure 5.29 shows the area stretch (as a measure of distributive mixing) for different kneading element widths of 2-lobe kneading elements. The smaller the disc width, the better was the area stretch and it was hypothesized that the increase in the number of gaps caused an increase in the area stretch (Ishikawa et al., 2001). Yoshinaga et al. (2000), studied isothermal flow of a Carreau model non-Newtonian fluid in the kneading section of twin-screw extruder using FEM simulations. The shafts were fitted with five pairs of three-lobed mixing elements configured at different stagger angles. Distributive mixing was measured by residence time distributions and the

minimum distance between mass-less particle markers after a give time of mixing. The simulations were performed as a quasi-steady state wherein the velocity profiles were calculated for every three degree rotation of the screw elements. Both the residence time distributions and the mean nearest distance between the markers showed the neutral stagger configuration to be the most beneficial for distributive mixing.

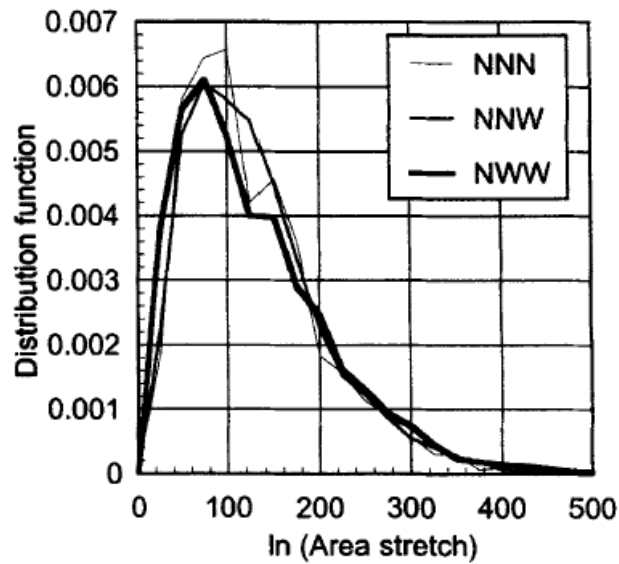
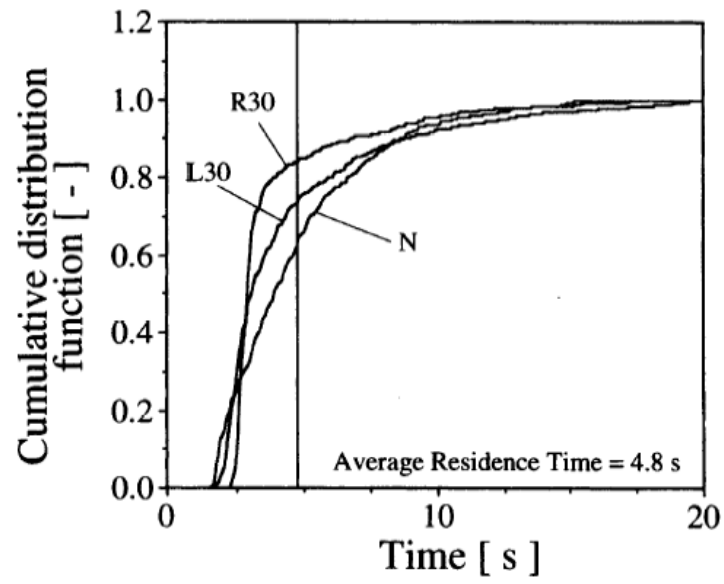
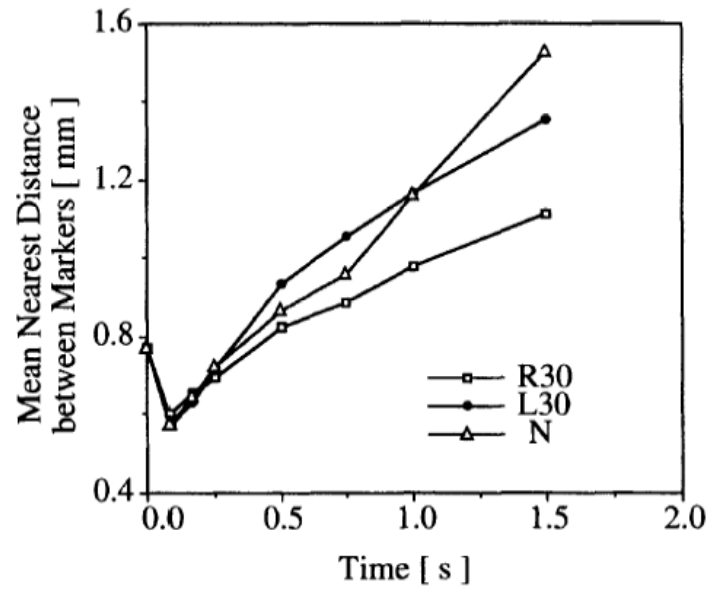


Figure 2.29 Distribution of the area stretch in the mixing region of a co-rotating twin-screw extruder for different widths of the kneading discs (Ishikawa et al., 2001).



(a)



(b)

Figure 2.30 (a) Residence Time Distribution and (b) Mean nearest distance between markers in the mixing region of a co-rotating extruder fitted with three-lobed kneading discs (Yoshinaga et al., 2000).

More recently, Ishikawa and Amano (2002) and Bravo et al. (2004), characterized the dispersive mixing efficiency solely in terms of the magnitudes of stress and strain respectively, ignoring the flow type. A quasi-steady step technique was used to solve the FEM simulations, similar to that of Yang and Manas-Zloczower (1992). The stress magnitude distribution of 1778 marker particles in a novel screw mixing element (SME) was compared to that in a conventional fully -flighted screw element and a kneading block with a 45° stagger angle. The SME consisted of a standard screw profile with slots cut across the flight tip to increase leakage flow. The stress magnitude showed a tri-modal distribution with each peak corresponding to the low stress regions in the flow channel, high-stress regions in the tip and intermeshing regions and a third intermediate stress region. While the fully-flighted screw element showed peaks at all the three regions, only the medium and high stress regions were seen in the kneading block and the SME (Ishikawa and Amano, 2002).

Limited published work is available on the analysis of viscous flow in continuous mixers with moving elements like the Readco co-rotating continuous mixer. Although similar in design to the twin-screw extruder, the Readco Continuous mixer is significantly different in terms of (i) larger dimensions and greater barrel and flow channel volume; (ii) Negligible to no axial pressure gradient and absence of constrained die at discharge end. The mixer design includes a pair of co-rotating shafts fitted with a series of conveying screws and a mixing region consisting of two or three lobed kneading blocks that can be staggered (Figure 2.31) followed by discharge screw elements.

As a first step to studying the twin-screw continuous mixer design, Connelly and Kokini (2007) used numerical simulations to compare mixing of a Carreau model fluid in a 2D single paddle mixer with a 2D twin-paddle mixer. The presence of a second paddle element in the twin screw geometry significantly improved both dispersive and distributive mixing. Figures 2.32 and 2.33 show the dispersive mixing index and the cluster distribution index in both mixers. While the twin screw geometry shows an increase in the area and magnitude of elongation flow the single screw geometry showed a cyclic cluster distribution index suggesting that the material points were unable to leave the streamlines and remain in clusters leading to poor distributive mixing.

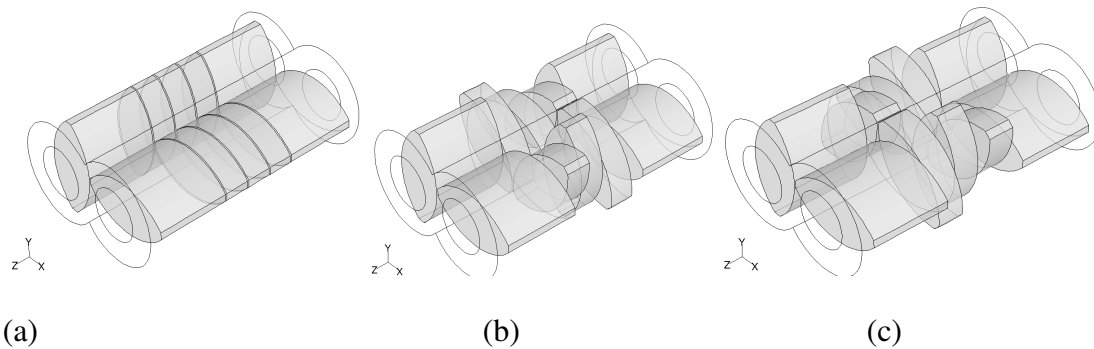


Figure 2.31 Kneading elements of the Readco ® twin-screw processor (Readco Inc, York, PA) arranged in (a) FLAT (b) 45F and (c) 45R configurations.

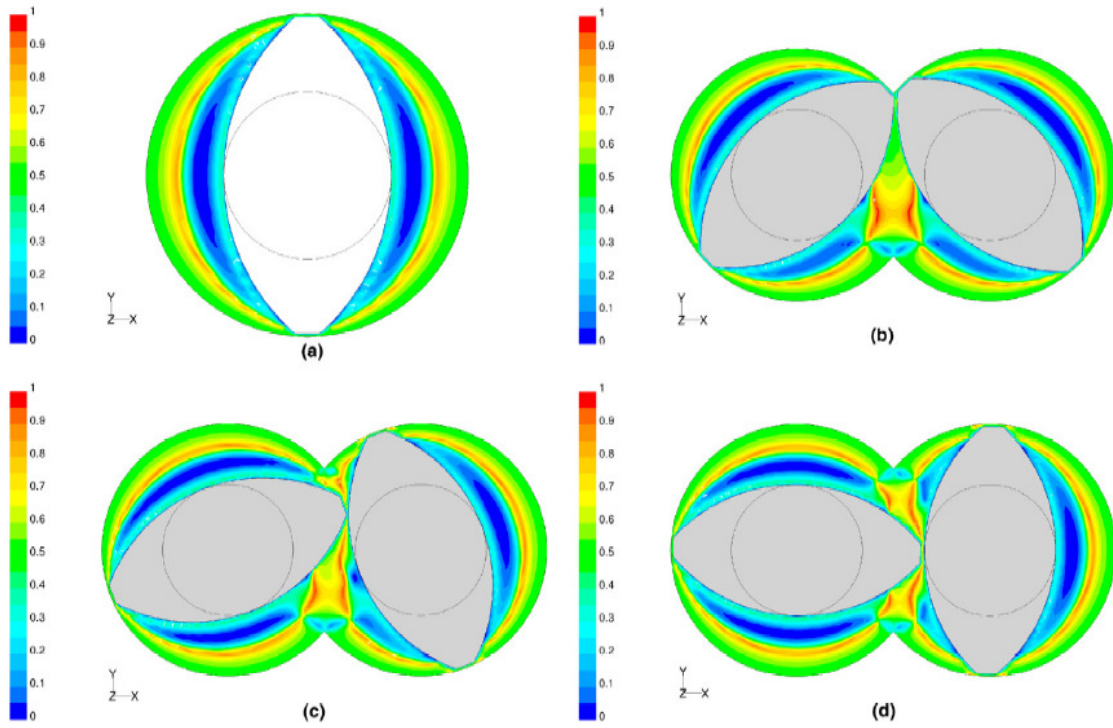


Figure 2.32 Mixing Index (λ_{MZ}) contours for the (a) single screw and twin-screw mixers after (b) 45° (c) 67.5° and (d) 90° rotation of the paddles (Connelly and Kokini, 2007).

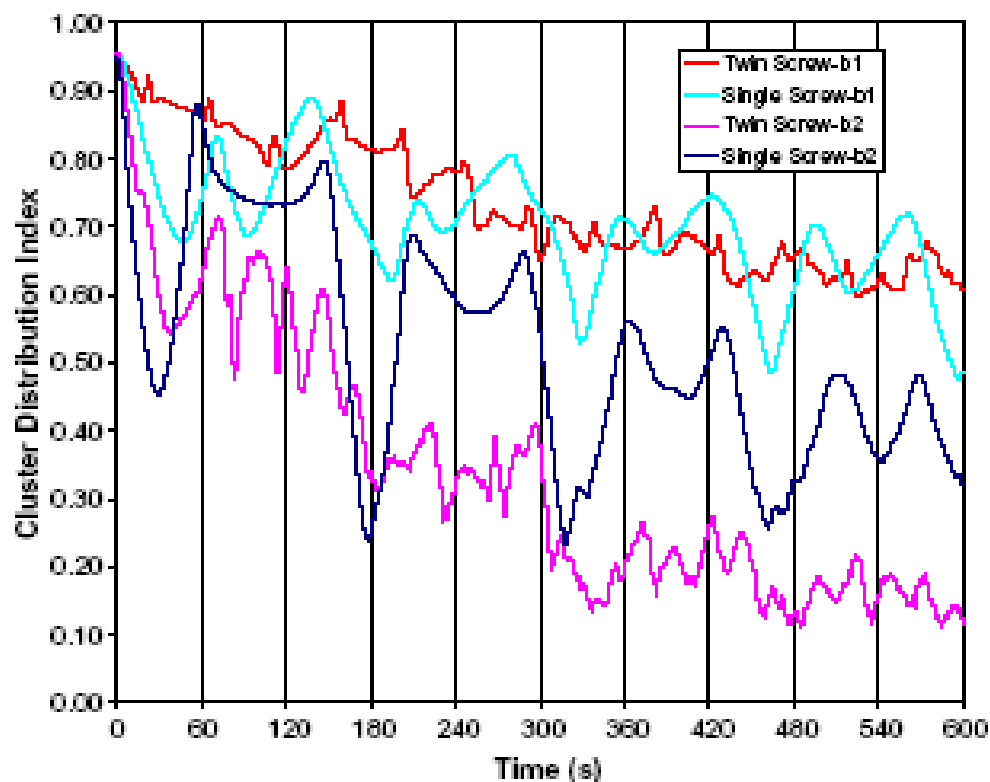
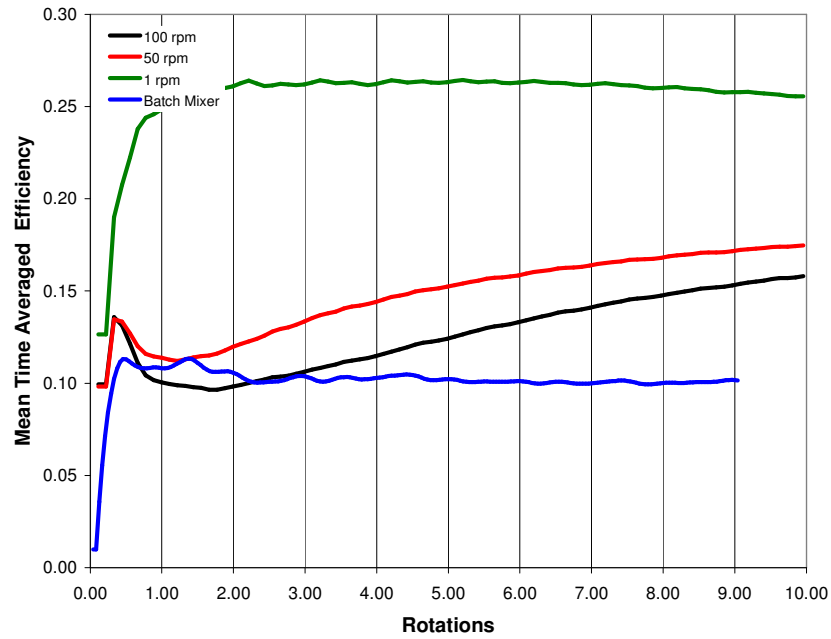


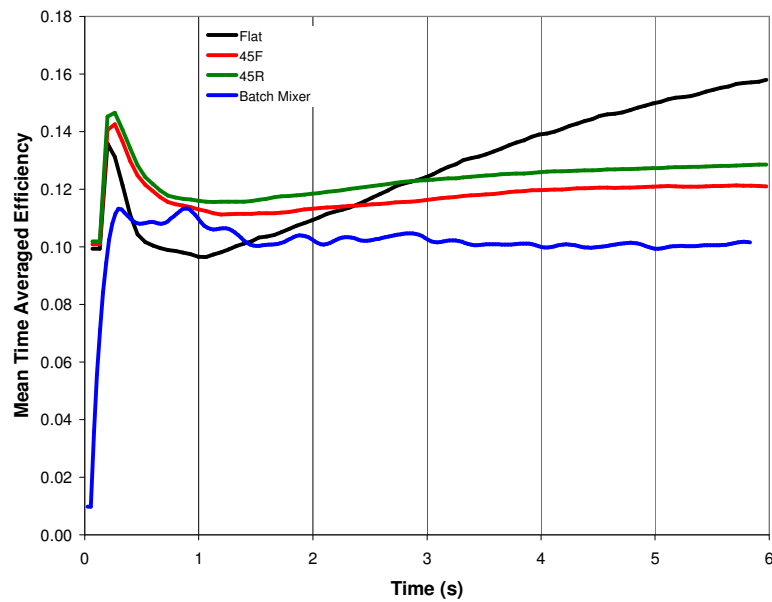
Figure 2.33 Comparison of cluster distribution index for 10 revolutions of the single screw and twin screw mixers with different location of the initial cluster in the flow domain – b1 (center location) and b2 (leftmost location) in the flow domain (Connelly and Kokini, 2007) .

While these simulations were useful in showing the positive effect of a twin-paddle element on the mixing effectiveness, 3D simulations of the full length mixer are needed for a realistic simulation of the continuous mixing that involves axial flow. The study of continuous mixers is mainly focused on evaluating the effect of screw speed, the stagger angle and the thickness of the paddle elements on the dispersive and distributive mixing measures and comparing the performance to a batch mixer. For example, consider the 3D numerical simulation of the mixing of a generalized Newtonian fluid in a full length kneading section of the Readco® continuous processor with nine paddle pairs. The

flow data was evaluated for every 10° movement of the paddles for 10 rotations at three different screw speeds (1 RPM, 50 RPM and 100 RPM) and then the various distributive and dispersive mixing measures were evaluated. The paddle elements were staggered forward and reverse at an angle of 45 degrees (Figure 2.31). Figures 2.34 shows the effect of screw speed and the stagger angle on the time-averaged efficiencies of the three continuous mixer geometries in comparison with the Farinograph. The time averaged instantaneous mixing efficiency decreased with increasing screw speed with highest efficiency at the lowest screw speed of 1 RPM which has been attributed to the higher material residence time at the lower screw speed resulting in greater stretching and folding of the material. The FLAT (or neutral) configuration showed the highest efficiency (Ashokan, 2008).



(a)



(b)

Figure 2.34 Effect of (a) screw speed and (b) screw configuration on the time-averaged mixing efficiency of the Readco® twin-screw continuous and the Farinograph batch mixers (Ashokan, 2008).

3. RESEARCH METHODOLOGY

3.1 Experimental materials and methods

3.1.1 Readco 2" Continuous Processor

The Readco 2" continuous processor (Readco, Inc., York, PA), a co-rotating twin-screw continuous mixer (Figure 3.1) was used as the model continuous mixer in this research. The mixer consists of a 17" long, jacketed mixing chamber with three liquid injection or temperature probe ports. The mixer has two horizontal co-rotating shafts that can be fitted with screw (conveying) elements and nine pairs of paddle (mixing) elements that can be arranged in various configurations to achieve different kinds of flow. The rotating shafts with the screw and paddle elements are enclosed in a horizontal '8' shaped barrel with a feed hopper at one end and an adjustable discharge gate at the other end. The conventional metal barrel was replaced with a custom made transparent Plexiglas barrel to allow for optical observation and recording of the bubbles. The barrel has several ports to allow for air injection during mixing.

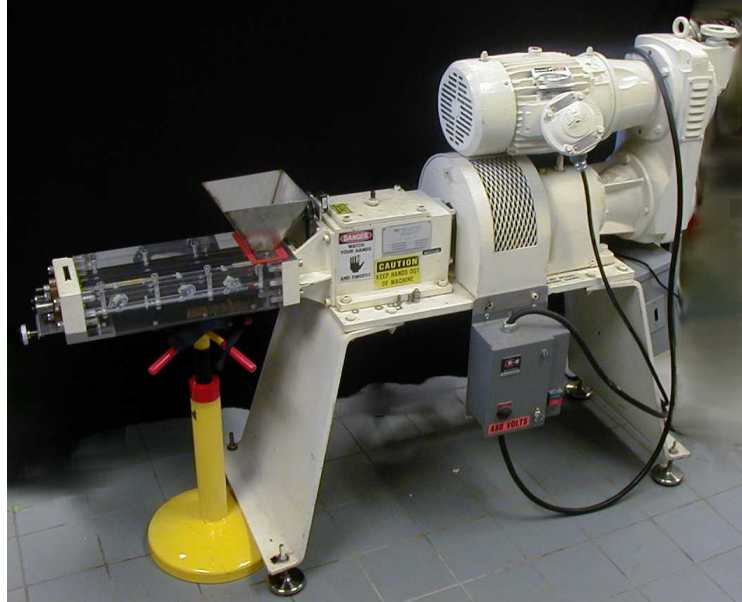


Figure 3.1. The Readco ® 2" Continuous Processor (Twin-screw mixer) fitted with a transparent Plexiglas barrel.

The mixer elements include 1/2" wide lens-shaped, self-wiping flat mixing paddles and 4" long conveying screw elements usually used at the feed and discharge points. Each screw configuration used for the study consists of two pairs of conveying screws in the feed region, followed by 9 pairs of flat mixing paddles and another pair of conveying screws in the discharge region (Figure 3.2). The co-ordinate system is defined in the 9 paddle element mixing region with the axial material flow direction as the direction of +Z, and the +Y axis coming out of the image plane. The shafts rotate in a clockwise direction when looking into the direction of flow, or + Z. The nine mixing elements were named P1, P2,..., P9 with the numbers increasing in the +Z direction. The locations of P1, P4 and P9 are represented by the mid=point of the respective paddle elements along the + Z axis at $z = 1.27$ cm, $z = 5.15$ cm and $z = 10.46$ cm, respectively.

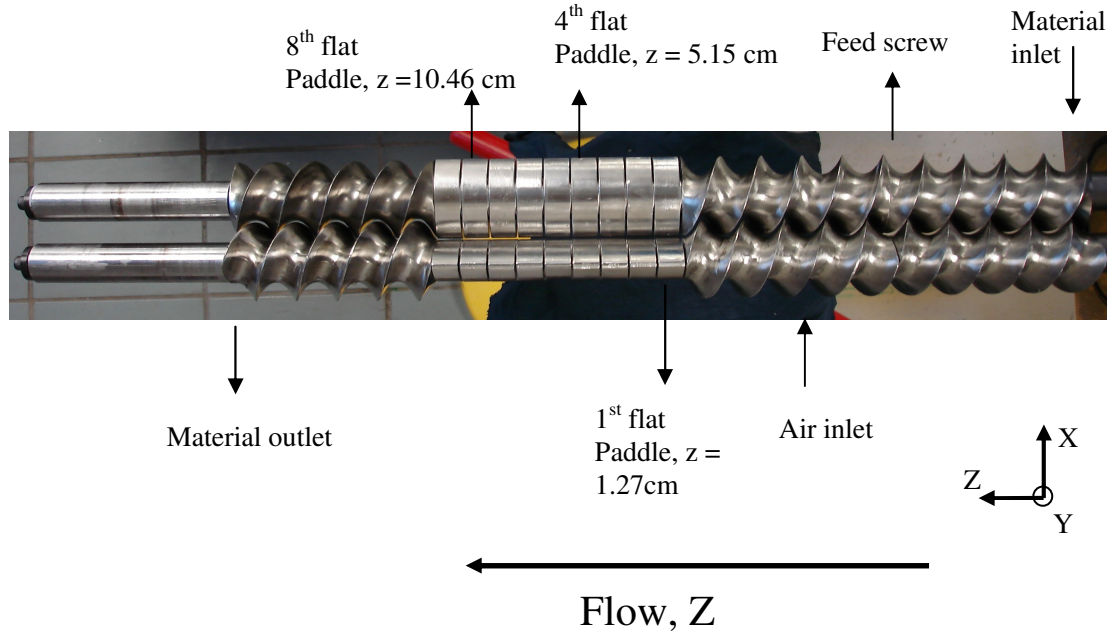


Figure 3.2 Conveying screw elements and mixing paddle elements of the Readco ® twin screw mixer without the barrel.

In this study the flow type distribution in the mixer was varied by changing the stagger angle in the paddle elements. Figure 3.3 illustrates the three different screw configurations used. The first of the three configurations (FLAT) had no stagger and was fully aligned with all the nine paddle elements configured parallel to each other. In the second configuration (45F), the first and the last three pairs of the paddle elements were kept same as the FLAT configuration while the center three elements were staggered at a clockwise/forward angle of 45° relative to the parallel elements in the direction of flow. Finally a third configuration (45R) was created similar to the 45F configuration except that the center three paddle elements were staggered 45° counterclockwise/reverse. The Polyflow FEM simulation software allowed for a total of 10 moving pairs at any given time. Hence the experimental design with only three staggered paddle elements was

chosen so that the first and the last three parallel paddle elements could be fused together as one paddle element.

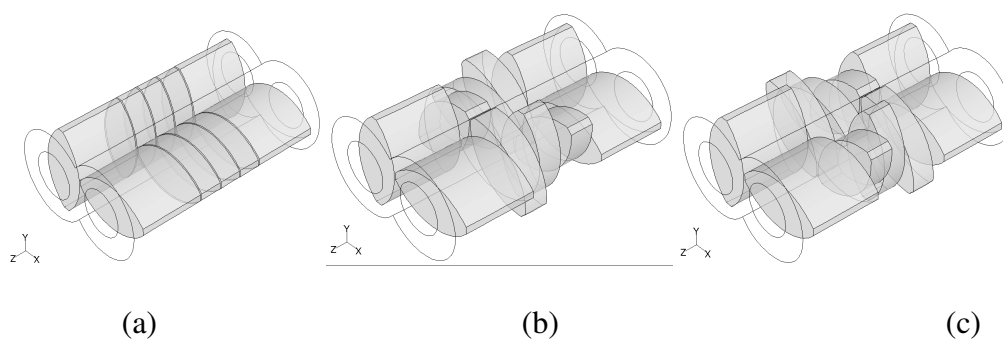


Figure 3.3 Schematic of sample paddle element configurations in the mixing region of the Readco processor. (a) Flat - all paddle elements parallel to each other, (b) 45F - three centre paddle elements in a forward stagger of 45° (c) 45R - three centre paddle elements in a reverse stagger of 45° .

3.1.2 Model mixing fluid and material properties

Newtonian high fructose corn syrup (HFCS) (Globe® Corn Syrup, Corn Products USA) was used as the model fluid, due to its transparency, allowing for optical observation and imaging of the bubbles. The rheology of the corn syrup was measured by a steady shear rate ramp experiment using a parallel plate rheometer (ARES, Rheometrics Scientific, NJ). The temperature dependence of density of the corn syrup was provided in the specifications sheet from the company. The mass flow rate of the corn syrup was measured with the three paddle elements at three screw speeds of 55, 75 and 100 RPM. Mass flow rate was experimentally measured as a function of screw speed for each

paddle configuration in the mixer. Corn syrup stored at 22 °C was allowed to fill the mixer barrel completely before starting the mixer. About 2 minutes of fully filled flow was allowed through the mixer in order for the flow to reach steady state. The barrel was kept fully-filled throughout the run thus keeping the inflow rate constant. The time taken to collect approximately 400-500 g of the material was used to calculate the mass flow rate and was converted into the volumetric flow rate using the density of the corn syrup. The surface tension of the corn syrup was obtained from Bohran and Pallinti (1986).

3.1.3 Bubble Imaging and Size Measurements

A Redlake MotionScope® M1 series high speed camera (DEL Imaging, CT, USA) with a 90 mm microscopic lens was used to capture the images of bubbles at various positions along the mixer barrel length with diffuse backlighting illuminating the subject area. The camera was fitted onto a motorized traverse system, enabling it to be moved in the three Cartesian co-ordinate directions precise to up to 0.1 mm. Thus it is possible to capture images of bubbles at precise positions along the mixer length. Figure 3.4 shows a schematic of the camera and light setup around the mixer barrel.

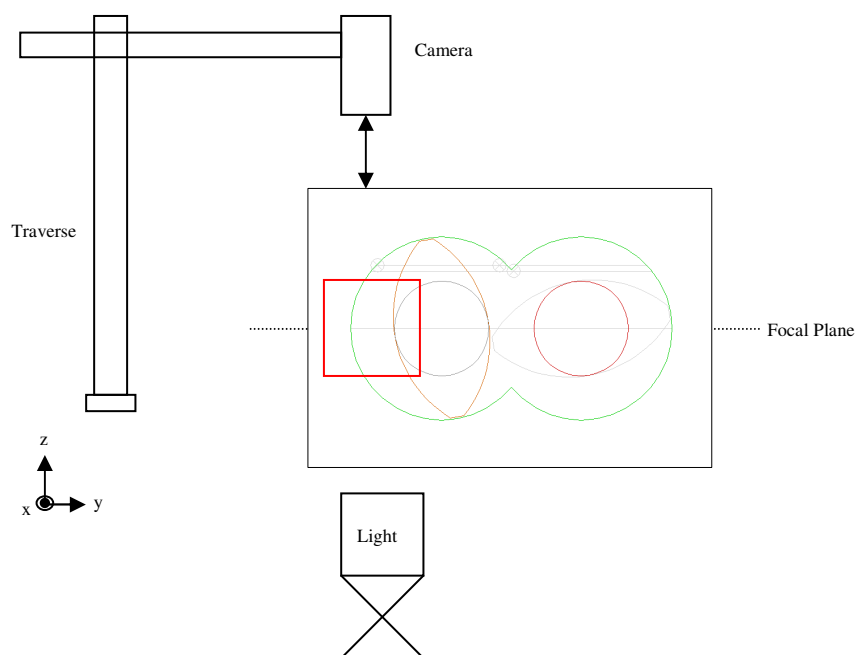


Figure 3.4 Schematic of arrangement for image capture of bubbles in the mixer against backlighting.

For each paddle element configuration, the model fluid was run through the mixer at two different screw speeds of 55 and 100 RPM, with air introduced at a constant flow rate in the feed screw region using a gas flow meter. Table 3.1 shows the material and operating parameters. In order to measure the local size distributions of the bubbles for the evaluation of bubble break up, the mixer was run until the flow reached a fully developed state (with the barrel fully filled), after which the mixer was momentarily stopped to capture images of the spherical bubbles at the different locations in the mixer. Bubble images were taken at various positions along the mixer length, e.g., in the feed screw region (FS), at the beginning of the mixing region (1st flat paddle, P1), in the middle (4th flat paddle, P4) and at the end (8th flat paddle, P8) of the mixing region. All the images inside the mixer were obtained from the region between the paddle and the barrel marked by the box in the figure 3.4. The camera was focused such that each frame

had a field of view equal to the width of a single paddle element, 1.54 cm (2"), which was used as the reference length for the image analysis. 3 to 5 images were taken at each location with 20-70 bubbles counted in each image.

High speed images captured at a frame rate of 1000 frames/sec were used to make qualitative observations of the highly elongated shapes of the bubbles. A further set of images obtained from material that has completely passed through the mixer was analyzed to test for the reproducibility of the aeration process and compare the effect of paddle element stagger on the overall breakup process in the mixer. The corn syrup was collected in a transparent petri dish for three different runs with each paddle configuration and about 70-100 bubbles were counted for each run. The captured images were analyzed using the VisiSize Solo® (Oxford Lasers, MA, USA) image analysis software for diameter data which was then fit to normal distributions using the statistics toolbox in MATLAB (The Mathworks Inc., Natick, MA, USA).

In order to test for reproducibility of the distributions, bubble images were obtained from three different sets run on different days with each set containing 3 or 4 images. The dimensions of each image were set to 4mm x 4mm using a reference image with a precise marker which was also used as the reference image in the image analysis software. The number of bubbles in each image ranged from about 70 to about 120 depending on the conditions at which the sample was obtained.

Viscosity, μ	Density, ρ	Surface Tension, σ	Screw speed	Gate Opening	Air Inlet	Material Flow rate
Pa.s	Kg.m ⁻³	Nm ⁻¹	RPM	m	SCFH at 2PSI	m ³ s ⁻¹
120	1.42×10^3	0.0808	55, 100	0.01	6-8	3.87×10^{-4}

Table 3.1 Material properties and operating parameters for air dispersion during mixing in the Readco® continuous processor.

3.2 FEM simulation of continuous flow and mixing

3.2.1 Construction of the FEM mesh of the Readco mixer for flow simulation

The FEM mesh used in this research for the flow and mixing simulations was developed by Connelly and Kokini (2004) and Ashokan (2008) and is described in detail in Vyakaranam et al. (2012). Figure 3.5a shows an individual paddle element mesh. The XY cross-section of the paddle was meshed with a total of 432 mesh elements and extended in the axial Z direction with three mesh intervals. Due to a limitation in the Polyflow software that allows for only ten moving parts, three pairs of the individually meshed paddle elements were fused together with an axial mesh interval of five and used for the non-staggered regions at the beginning (P1, P2, P3) and at the end (P7, P8, P9) of the mixing region (Figure 3.3b). The center three paddle element pairs (P4, P5, P6) were not fused in order allow for individual stagger. Figure 3.3c shows the simulation mesh used for the 2D XY cross section of the barrel volume, meshed with a total of 1072 mesh elements using 10 mesh intervals in the radial direction that included 2 intervals for the

boundary layer, while 56 mesh intervals were used in the azimuthal direction. The intermeshing region was further finely meshed to avoid mesh elements being covered by the two paddles at the same time. This included a convex mesh with boundary layers on the inner side where both paddles could enter at the same time and four adjoining quadrants where only one paddle would be present at a given time. The incorporation of the boundary layer into the convex region ensured that there were always two mesh elements in the gap between the paddle elements. The meshed XY cross-section was extended into 3D to cover entire barrel volume. The axial mesh interval of the barrel volume was set equal to coincide with the individual (3) and the fused (5) paddle regions. The gap between individual paddle elements, which is 0.0762 cm as measured in the Readco mixer, was meshed with a two-mesh interval. In order to isolate the paddle elements from entrance and exit effects, the axial length of the barrel volume mesh was extended on both sides to include a two-mesh interval equal to half the length of a single paddle element (0.635 cm).

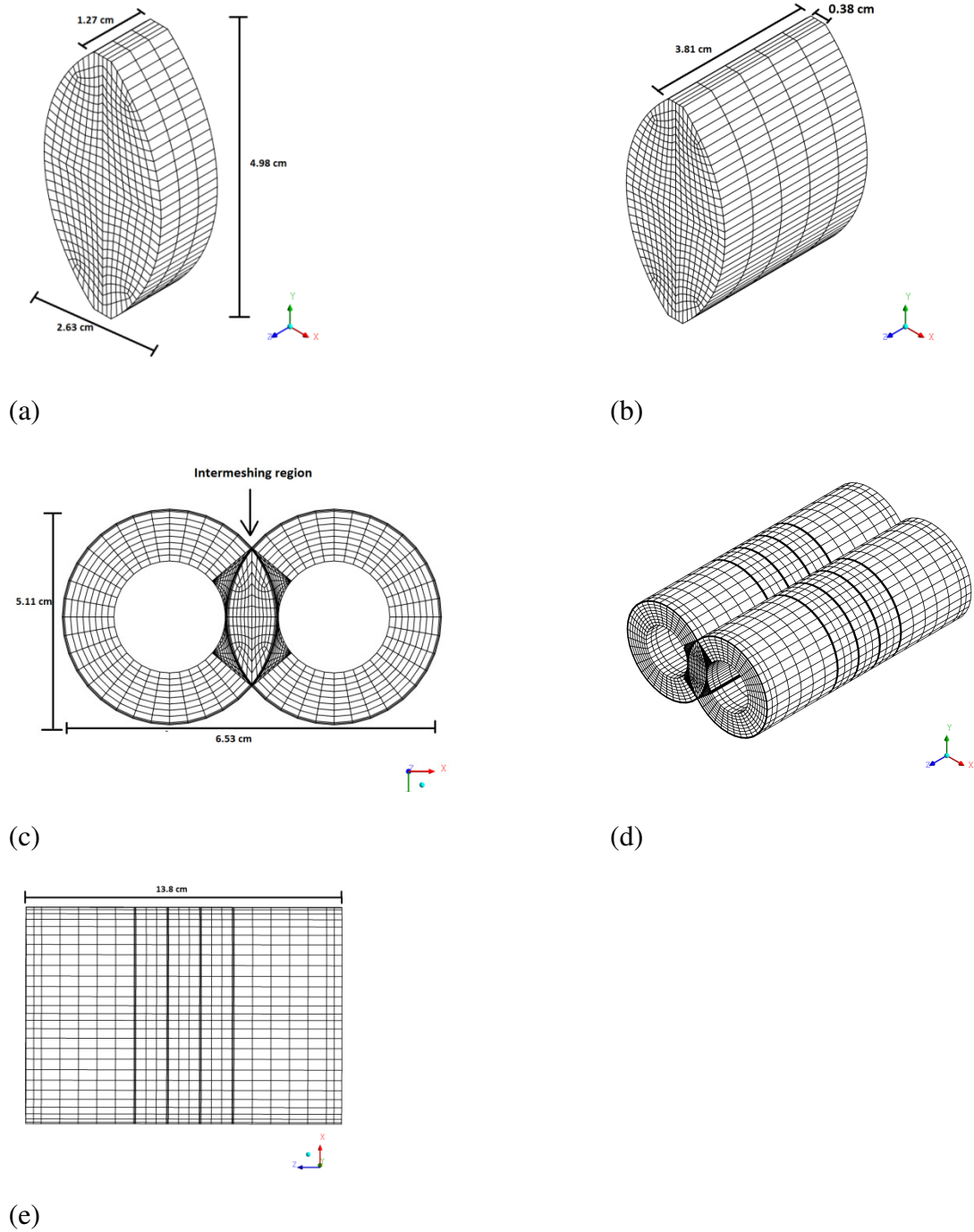


Figure 3.5 (a) 3D single paddle mesh with a total of 432 X 3 mesh elements (b) 3D three paddle mesh with a total of 432 X 5 mesh elements (c) Radial mesh of the XY cross-section of the barrel volume with a total of 1072 elements (d) Barrel volume mesh (e) Axial profile of the barrel volume mesh (Vyakaranamet al., 2012).

3.2.2 FEM flow simulation to obtain flow field and velocities using POLYFLOW

3D finite element method simulations of the twin-screw mixing process were run using the mesh superposition technique of the Polyflow[®] software suite (Fluent Inc., Lebanon, NH) described in section 2.4.3. There are three major steps involved in solving a flow simulation task as shown in Figure 5.6. In the first step an FEM mesh of the mixer geometry is constructed using Gambit[®], the mesh-building software module, as described in the previous section.

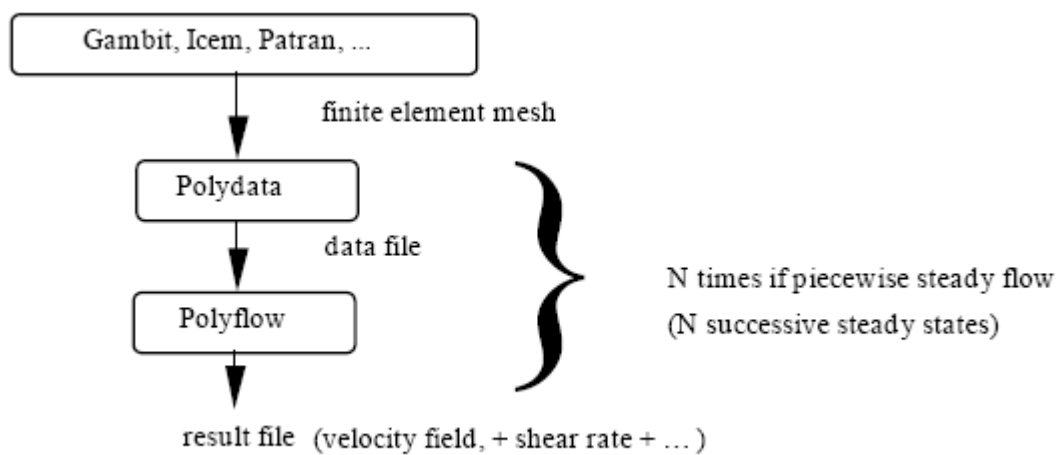


Fig 3.6 Steps involved in solving a flow simulation task (Polyflow[®] User Guide, Fluent Inc., Lebanon, NH).

The individually meshed paddle elements constituting a total of 10 moving parts fused together were superimposed onto the barrel volume mesh in an initial starting orientation. The FEM mesh consists of the mixing paddles and the entire barrel volume with inflow and outflow boundary planes as shown in Figure 3.7. Three different mesh

files are created for the three screw configurations – Flat, 45F and 45R as shown in Figure 3.3.

This fused mesh is imported into Polydata, the GUI interface of Polyflow ® where the simulation data file is built specifying the material and operating parameters, the flow boundary and initial conditions and the numerical parameters. Due to the absence of the conveying screw region in the simulation, liquid flow rate value was experimentally measured for the corn syrup and was used on the inlet boundary plane with a fully developed velocity profile.

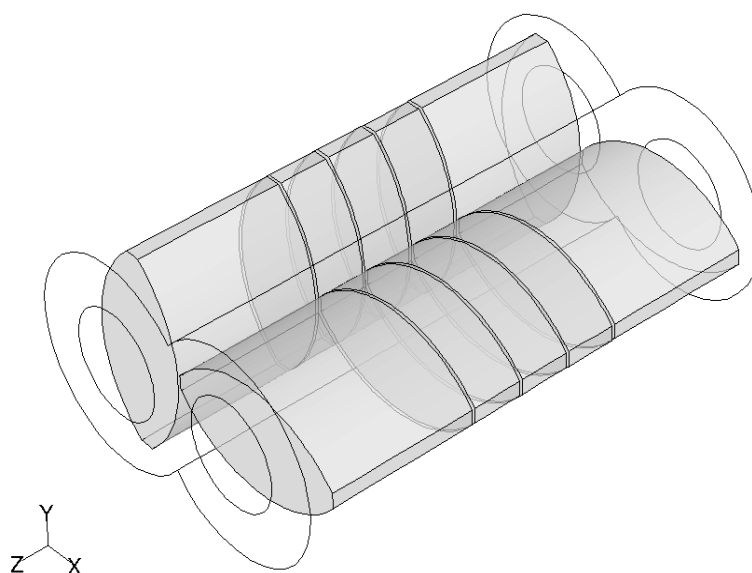


Figure 3.7 FEM simulation mesh of the mixing region showing the inflow and outflow boundary planes.

The simulation was solved for one full revolution of the elements in 36 steps at every 10° movement of the paddles which constitutes a single ‘time step’. Gravitational forces were neglected and the density was equal to the fluid density of corn syrup. The local velocity profiles, flow strength and mixing index data were calculated by solving

the modified Navier-Stokes equations (described in section 2.4.2) using the implicit Euler scheme in the entire mixer and stored for each time step (angular position) of the paddles.

The flow was assumed to be fully developed and the velocity data was calculated at all elements (nodes) of the mesh recognized as fluid element for every 10° angular movement of the rotating paddle. Thus for every revolution of the paddle elements (360°), there were 36 result files containing the flow data at each time step. Figure 4.8 shows three different angular positions of the paddle elements. During each full rotation of the mixer shafts the relative orientation of the paddle elements at a 10° rotation (time step 1) was equivalent to the relative orientation at rotation of 100° (time step 10), owing to the symmetry of the mixer geometry. Hence for the purpose of this study comparing the effect of paddle element configuration on the local flow profile, investigation of the flow in the first nine time steps was deemed sufficient and was consistent with the method used by Yao and Manas-Zloczower, (1998). The mean velocity, flow strength and mixing index data were calculated over three different cross-sectional planes along the mixer length, P1 ($z = 1.27$ cm), P4 ($z = 5.15$ cm) and P9 ($z = 10.46$ cm) using data from all the 9 time steps in one revolution. However, graphical comparison of the XY distribution of velocity profiles and mixing index data at the different cross-sectional planes for each paddle configuration are presented at time steps 1, 4 and 9 (rotation of 10° , 40° and 90°) in order to simplify the analysis while at the same time include velocity profile information after a significant rotation of the paddle elements.

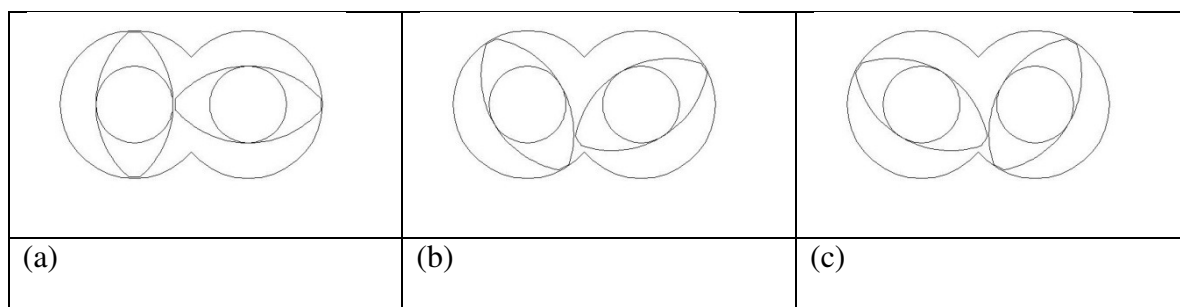


Figure 3.8 Angular positions of the mixer paddle elements after, a) 0° rotation, b) 30° rotation, c) 60° rotation.

Using the velocity result files from the flow simulation, a ‘mixing simulation’ was constructed in Polyflow to calculate the paths (trajectories) of mass less particles as they travel along the mixer and also the corresponding shear rates and mixing indices at each point on the trajectories. For each set of mixer operating conditions a statistically significant number of such material trajectories (100) were computed in order to best represent the actual paths of the bubbles in the mixing experiments.

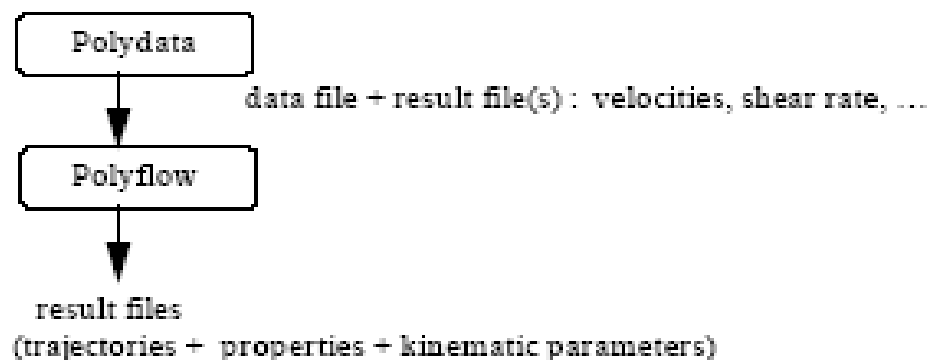


Fig 3.9 Steps involved in solving a mixing simulation task (Polyflow ® User Guide, Fluent Inc., Lebanon, NH).

3.3 Calculation of dispersion parameters

3.3.1 Capillary Numbers (Ca and Ca_{cr})

The mean capillary numbers (Ca) for a range of bubble diameters from 100 μ m to 1200 μ m were calculated from equation 2.24, at the three paddle element locations P1, P4 and P8, using the simulated mean shear rate (G_{mean}) over the XY cross-sectional planes at these locations, for the three paddle element configurations. The mean Ca envelopes were used to test the limits of the Ca values prevalent in the mixer against the critical Capillary number (Ca_{cr}) for breakup in simple shear, pure elongation and intermediate flows.

For the corn syrup- air system of viscosity ratio 1.42×10^{-7} , for simple shear flow ($\lambda_{MZ} = 0.5$), Ca_{cr} for drops were calculated using the correlation of Hinch and Acrivos (1980) given equation 2.42. Additionally, the Ca_{cr} for bubbles in simple shear flow was also calculated from equation 2.47 (Muller-Fischer et al, 2008). For flows with $\lambda_{MZ} \geq 0.6$, the correlation from Bentley and Leal (1986) for flow types between simple shear and pure elongation (equation 2.43) and the relation between α and λ_{MZ} (equation 2.64) were combined to obtain the Ca_{cr} as follows:

$$Ca_{cr} = 1.9174 \cdot (\lambda_{MZ})^{(-1.555)} \quad (3.1)$$

3.3.2 Maximum stable bubble diameters (d_{max})

For all the points in the mixer at each cross-sectional plane, the theoretical maximum stable diameter, d_{max} was evaluated for simple shear flow using equation 2.47 and the mean shear rates evaluated by the simulations. For all the points over the cross-

sections at each location in the mixer where the flow is in between simple shear and pure elongation (i.e., $\lambda_{MZ} \geq 0.6$), d_{max} was evaluated by combining equation 3.1 with the definition of Ca_{cr} (equation 1.1) and using the local shear rate, G , and dispersive mixing index, λ_{MZ} , evaluated by the simulations at each point, as follows:

$$d_{max} = (73.082) \cdot \left(\frac{\sigma}{\mu_{cont} \cdot G} \right), \lambda_{mz} = 0.5 \quad (3.2)$$

$$d_{max} = (3.83) \cdot \left(\frac{\sigma}{\mu_{cont} \cdot G} \right) \cdot (\lambda_{MZ})^{(-1.555)}, \lambda_{MZ} \geq 0.6$$

While local dispersive mixing index and shear rate data gives valuable information on dispersive mixing efficiency in general, equation (3.2) for $\lambda_{MZ} \geq 0.6$ can be used to evaluate the maximum stable bubble diameter distributions across cross-sections in the mixer volume with varying paddle configurations. The maximum stable diameter represents the combined effect of flow strength (local shear rate, G) and the flow type (dispersive mixing index, λ_{MZ}) for mixed flows between simple shear and pure elongation. The maximum stable diameters, d_{max} , were also compared with the experimentally measured mean bubble diameters, d_{mean} .

3.3.2 Effective shear rate for dispersion (G_{eff})

Additionally, for the measured mean diameters (d_{mean}) of the bubble size distribution in the mixer, an effective shear rate, G_{eff} , was estimated from equation 2.51 using the d_{mean} and was compared with the mean shear rate values (G_{mean}) over XY cross-sections at the

beginning and the end of the mixing region (P1 and P8) predicted by the simulation for screw speeds of 55 and 100 RPM. The effective shear rates for dispersion were calculated assuming Ca_{cr} for simple shear ($\lambda_{MZ} = 0.5$), pure elongation ($\lambda_{MZ} = 1.0$) and an intermediate flow at $\lambda_{MZ} = 0.6$, as follows:

$$G_{eff} = \frac{2 \cdot Ca_{cr} \cdot \sigma}{\mu \cdot d_{mean}} \quad (3.3)$$

4. RESULTS AND DISCUSSION

4.1 PART I. Evaluation of flow profiles in the Readco continuous mixer

Figure 4.1 shows a comparison of experimentally measured material flow rates for the three paddle configurations as a function of the screw speed. The flow rate was clearly dependent on the screw speed but was independent of the paddle element configuration. This is due to the fact that the barrel volume was always maintained fully filled and then the flow is purely conveying and is not driven by a net pressure gradient as would be the case in a static mixer. Thus, with a constant inlet flow rate and discharge die opening, the overall flow rate through the mixer is strongly controlled by the conveying screws and is not significantly affected by the stagger angle in the paddle elements. The measured average value of the volumetric flow rate at 100 RPM was used as the imposed inlet boundary condition in the numerical simulation to understand the local distribution of velocities.

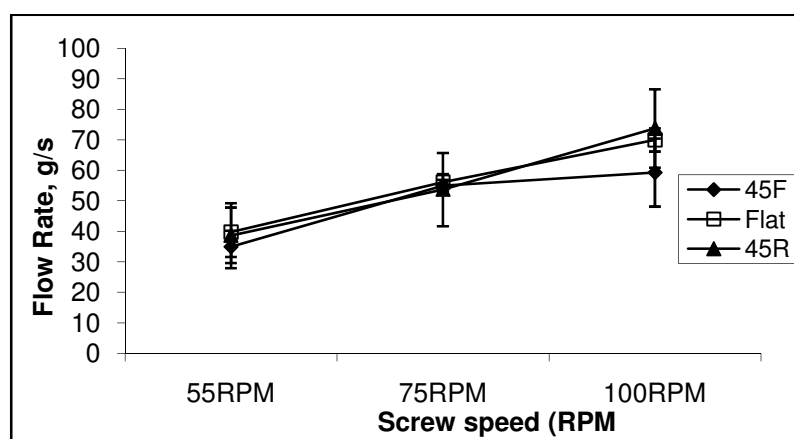


Figure 4.1 Experimental mass flow rate of Globe ® Corn Syrup 042110 measured in the Readco® 2” continuous processor as a function of screw speed and paddle element configuration.

For each of the time steps (1, 4, and 9) we present here comparison of velocity profiles using velocity vector maps throughout the mixer volume, axial velocity contour maps at various XY cross-sections along the mixer axis, and axial velocity magnitudes along a line running through the nip region of the paddle elements along the length of the mixer.

4.1.1 Comparison of velocity magnitudes throughout the whole mixer

Table 4.1 shows the comparison of the range of velocity magnitudes found in the entire mixer volume over one complete revolution of the screw. The FLAT configuration showed highest total velocity magnitudes followed by the 45F and the 45R configurations. The range of magnitudes of X, Y and Z components of velocity were also higher for the FLAT configuration compared to the staggered configurations, with the reverse 45R configuration showing the smallest ranges. This is thought to be due to the unobstructed channel flow in the FLAT configuration allowing for local regions with the highest velocity magnitudes.

Paddle Configuration	V	V _x	V _y	V _z
	Max/min	Max/min	Max/min	Max/min
FLAT	106.3/0	42.1/-70.61	105/-41.22.8	77.5/-83.76
45F	71.89/0	47.97/-58.29	71.50/-37.03	66.7/-62.14
45R	37.23/0	35.35/-33.52	31.04/-31.28	27.52/-33.88

Velocity units, cm/s

Table 4.1 Maximum and minimum values of total velocity magnitude (V) and V_x, V_y and V_z calculated at all points in the entire mixer volume for one complete revolution of the three paddle elements (FLAT, 45F and 45R).

A visualization of the velocity vector maps is presented in figures 4.2 to 4.4 for the three screw configurations, each at time steps 1, 4 and 9. The vectors are color coded from dark blue to dark red corresponding to the global range of overall velocity magnitudes with a range from 0 to 120 cm/s combining the three paddle element configurations. The distribution of the velocity vectors shows that the flow generally follows the paddle surface with additional axial flow occurring in the intermeshing region between the paddles. In the FLAT configuration with no stagger, at the first time step a significant forward flow is seen in the first half of the mixing region (P1 to P4) caused by the imposed inflow boundary condition while in the latter half (P5 to P9), a significant backward flow is observed. This is probably due to the material flowing back from the gap between the last paddle pair (P9) and the outflow plane. Figure 4.5 shows the pressure profile over the $x = 0$ and $y = 0$ planes at time steps 1, 4, 9 and 10 for the FLAT configuration and at time step 4 for the 45F and 45R configurations. While the overall pressure levels are lower than typical extrusion processes (mainly due to the greater

barrel volume and absence of constricted die as discussed earlier), the FLAT configuration shows increased pressure zones in the intermeshing region. This suggests that the flow mechanism involves the material being squeezed into and out of the intermeshing region causing increased axial flow. Figure 4.5 also shows the pressure profiles at time step 10 (100° rotation) which is symmetric to the profile at time step 1 (10° rotation) showing that the flow profile is cyclic with a period of 90° .

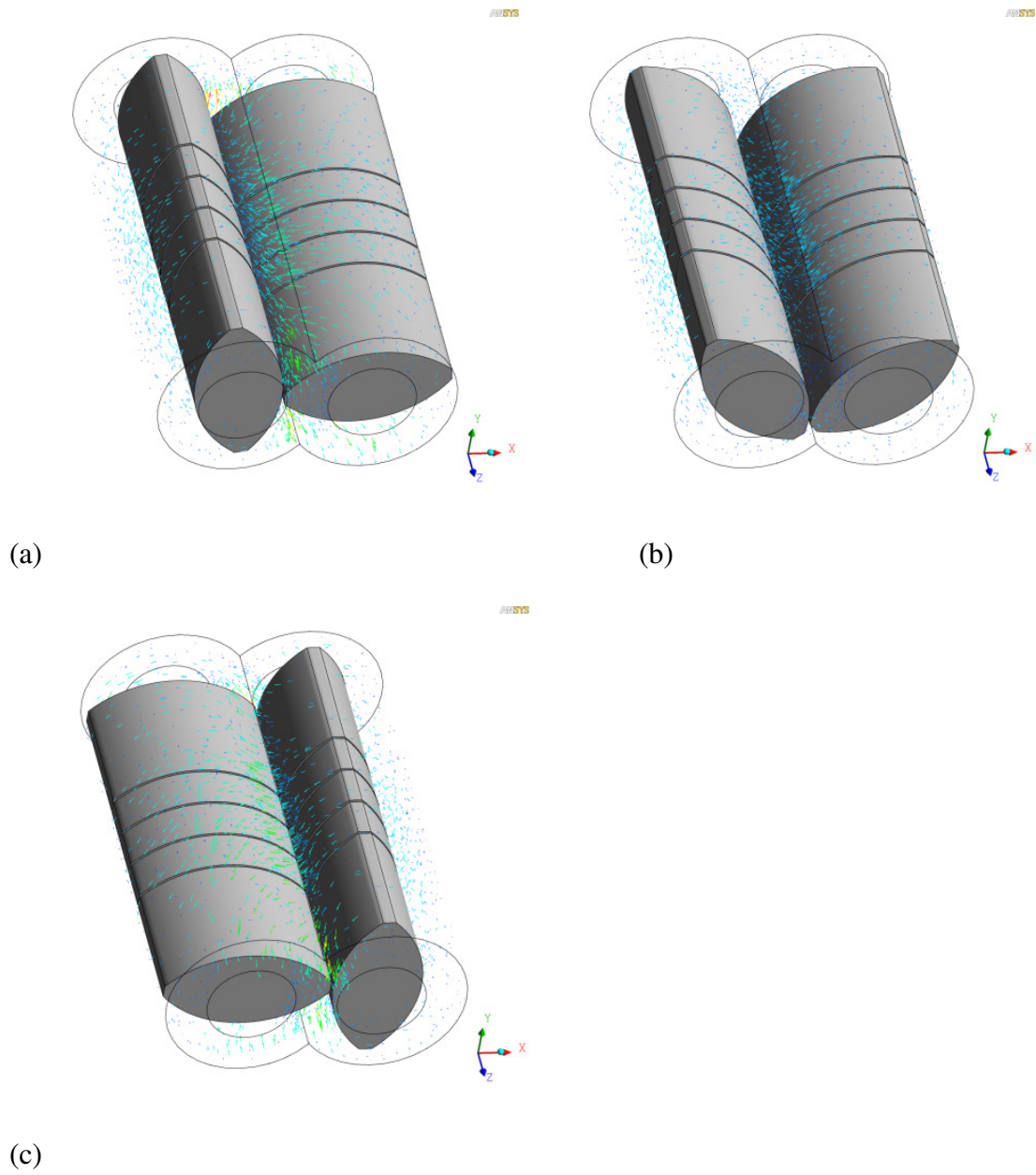


Figure 4.2 Velocity vector maps for the FLAT configuration at (a) time step 1, 10° rotation (b) time step 4, 40° rotation and (c) time step 9, 90° rotation.

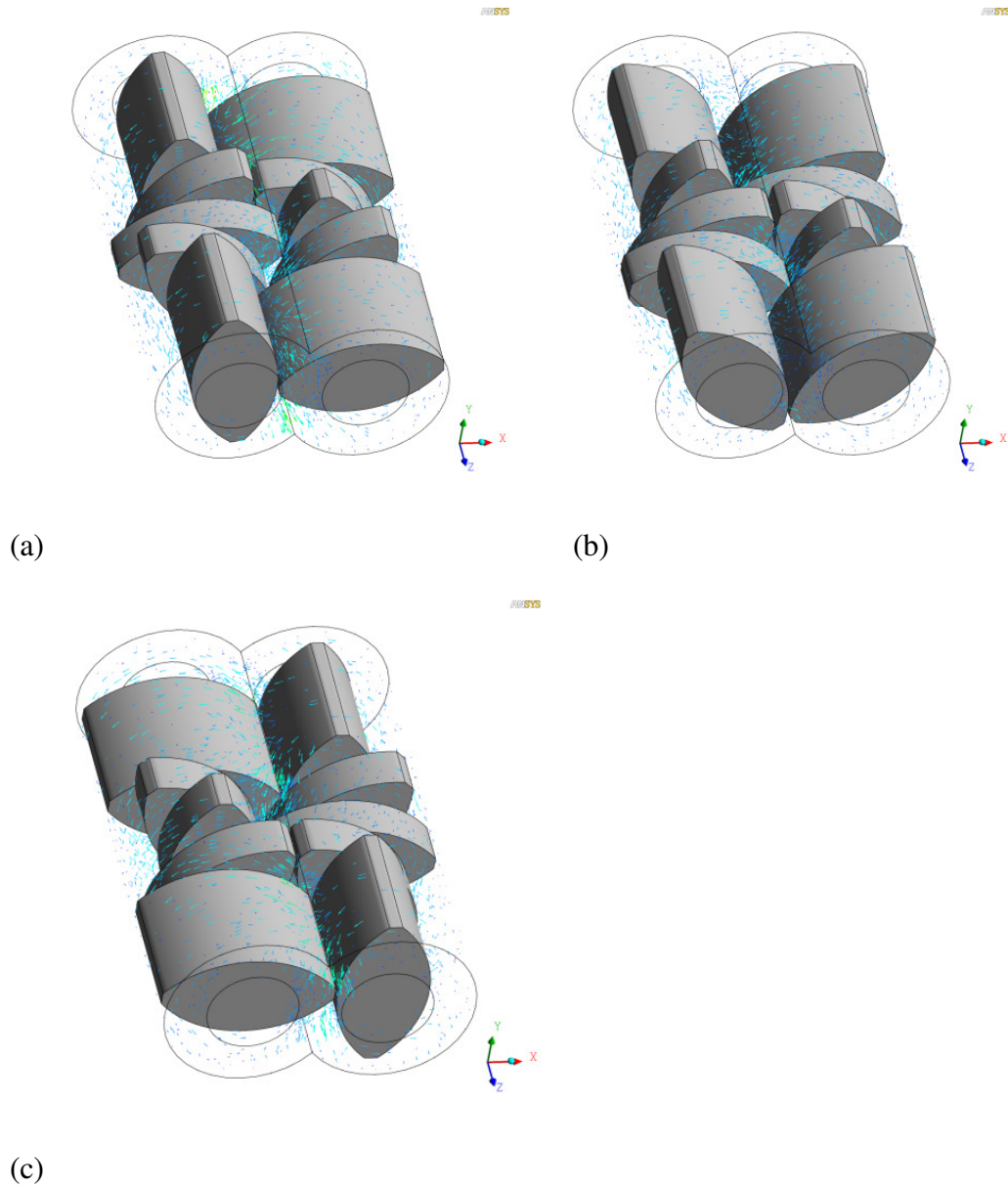


Figure 4.3 Velocity vector maps for the 45F configuration at (a) time step 1, 10° rotation
(b) time step 4, 40° rotation and (c) time step 9, 90° rotation

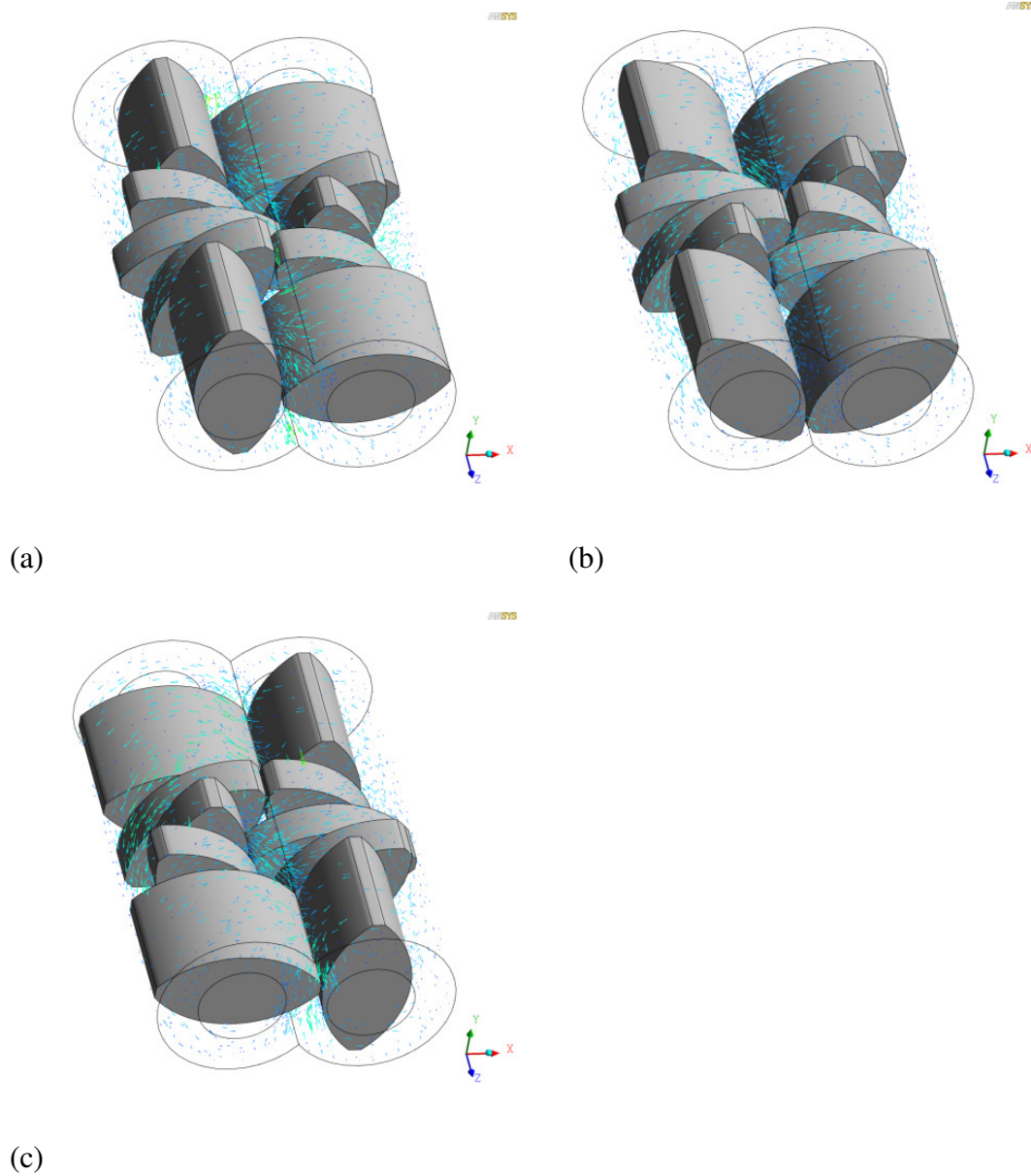


Figure 4.4 Velocity vector maps for the 45R configuration at (a) time step 1, 10° rotation (b) time step 4, 40° rotation and (c) time step 9, 90° rotation.

In the forward 45° stagger configuration (45F), significant regions of increased forward flow are seen in the ‘intermeshing region’ between the paddle elements at all the three time steps, especially in the middle of the mixing region right after P4 where the stagger angle is introduced. In contrast, regions of backflow can be seen in the reverse 45° stagger configuration (45R) at the beginning and towards the end of the staggered region

(P4 and P7). The pressure profiles over the $x = 0$ and $y = 0$ cross-sectional planes for 45F and 45R configurations from Figure 4.5 show that there is little variation in the pressure for both the configurations. While the pressure profiles shown here are only for time step 4, the trend was similar at all time steps. This suggests that the local axial forward and backflow in the staggered regions seems to be caused by gaps that appear in the intermeshing region between two consecutive staggered paddles.

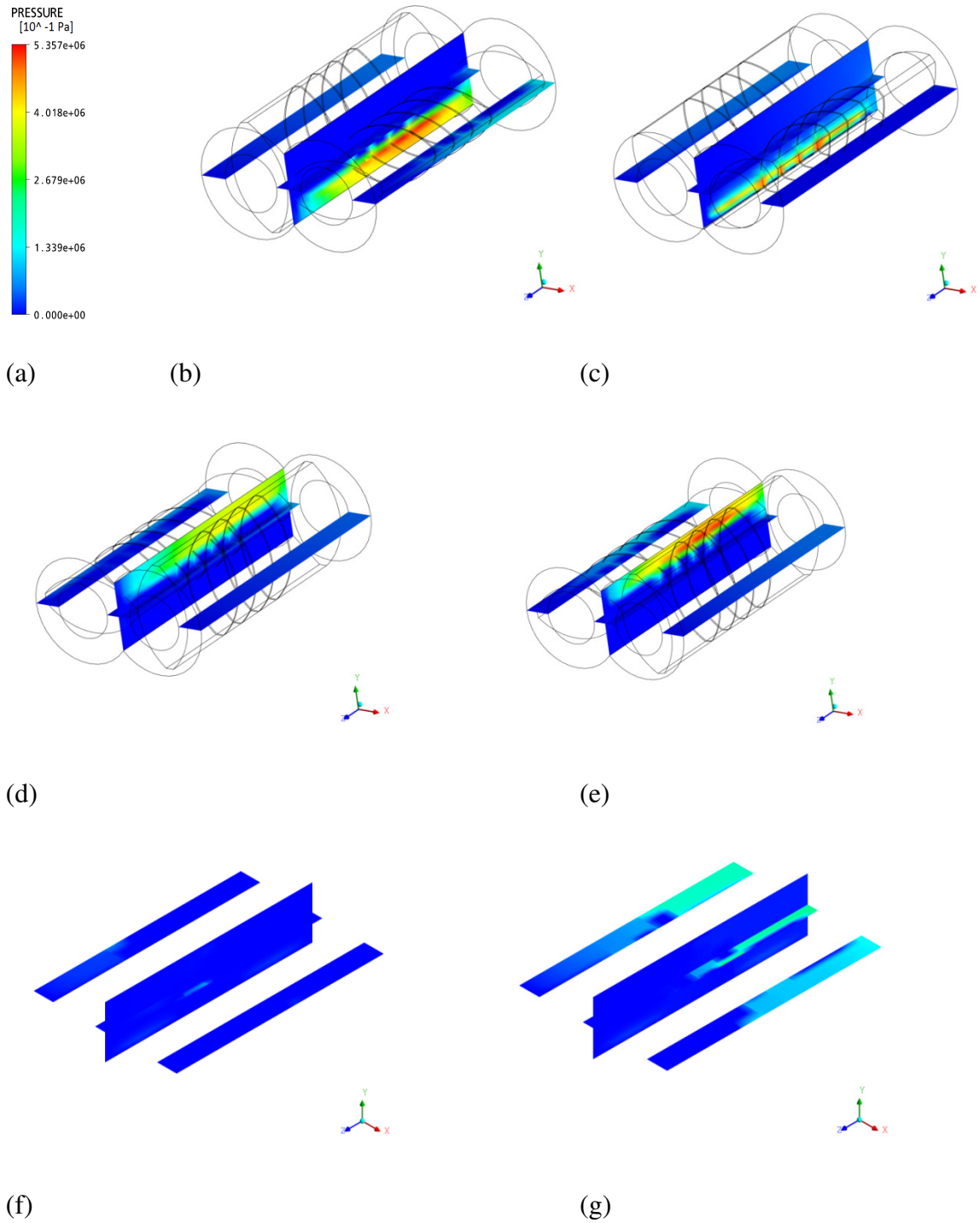


Figure 4.5: Pressure contours over $x=0$ and $y=0$ cross-sectional planes in the FLAT configuration at (a) Legend (b) time step 1, (c) time step 4, (d) time step 9, (e) time step 10, (f) 45F configuration at time step 4 and (g) 45R configuration at time step 4.

4.1.2 Comparison of local velocity magnitudes over XY planar cross-sections

XY planar cross-sections of the mixing region were analyzed for the distribution of local X, Y and Z velocities (V_x, V_y, V_z). Figures 4.6 and 4.7 show the contour maps of magnitudes of the X and Y velocity components (V_x and V_y) at the 4th paddle element (P4) after a rotation of 40° (time step 4). The cross-section can be divided into three broad regions of flow activity – the ‘C’ shaped region between the paddle element and the barrel wall, the ‘intermeshing region’ between the co-rotating paddle elements and the ‘nip’ regions which is the narrow, constricted gap between the paddle tips and the barrel surface. While the distribution of both V_x and V_y was as expected in relation to the rotating paddle elements, there was also no significant variation of the range of local velocity magnitudes among the three configurations. The highest magnitudes of positive and negative V_x were just above the average values in all the three configurations while magnitudes of V_y significantly greater than the average values were seen around the leading and trailing edges of the paddle elements.

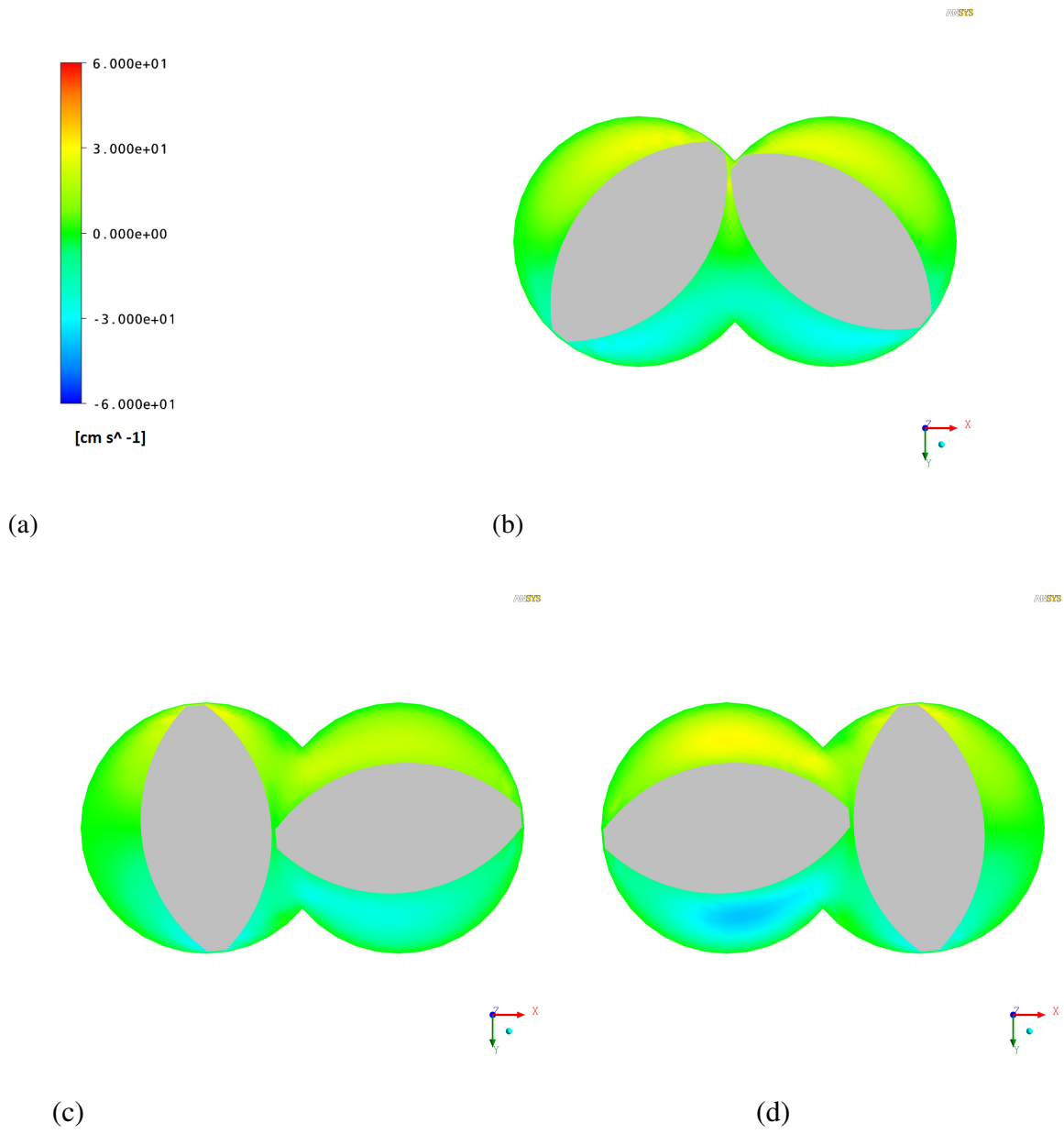


Figure 4.6 Contour maps of V_x at P4 and time step 4 (a) Legend (b) FLAT (c) 45F and (d) 45R configurations.

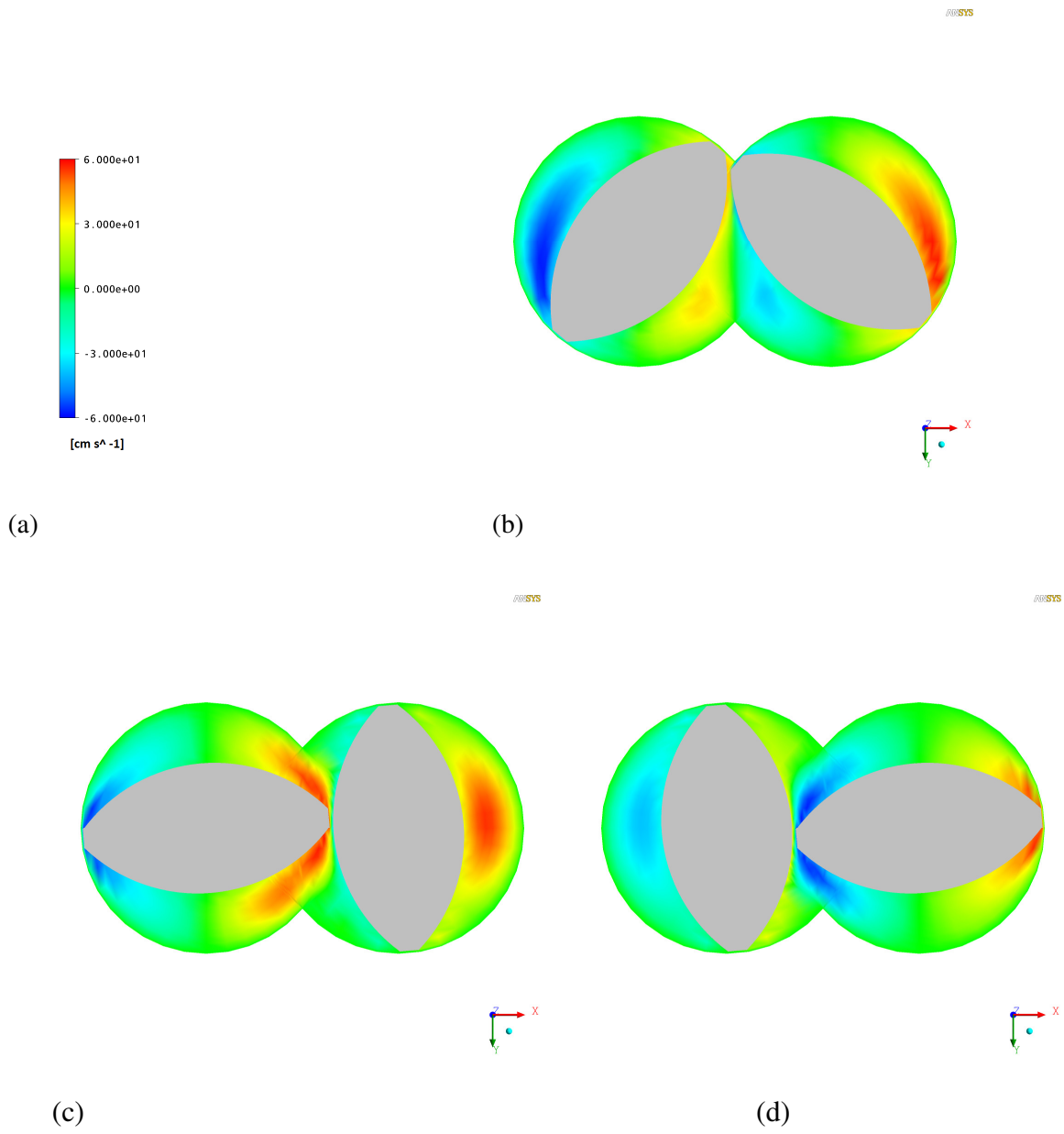


Figure 4.7 Contour maps of V_y at P4 and time step 4 for (b) FLAT (c) 45F and (d) 45R configurations.

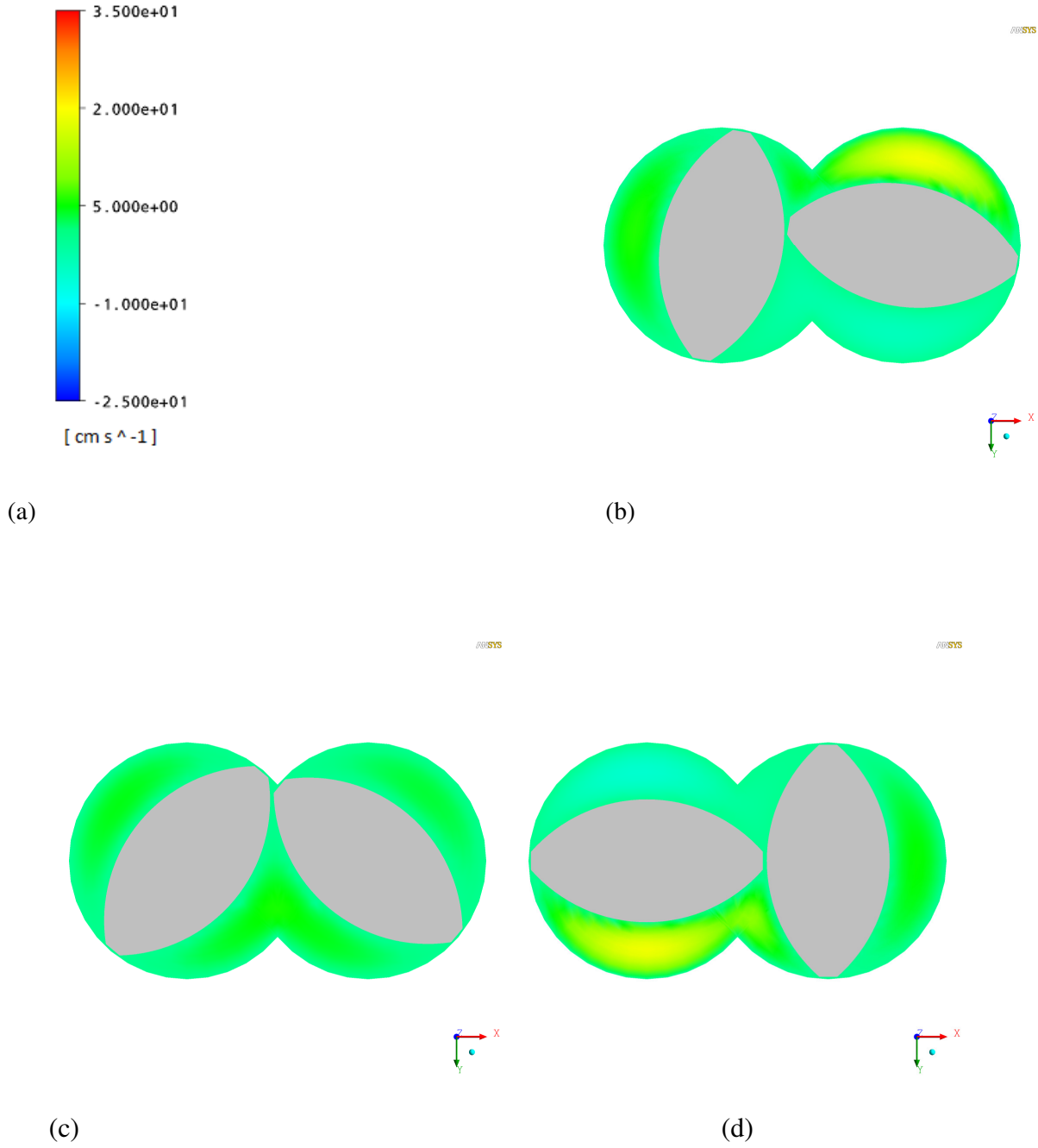


Figure 4.8: Contour maps of axial velocity (V_z) at P4 in the FLAT configuration (a) time step 1, 10° rotation (b) time step 4, 40° rotation and (c) time step 9, 90° rotation.

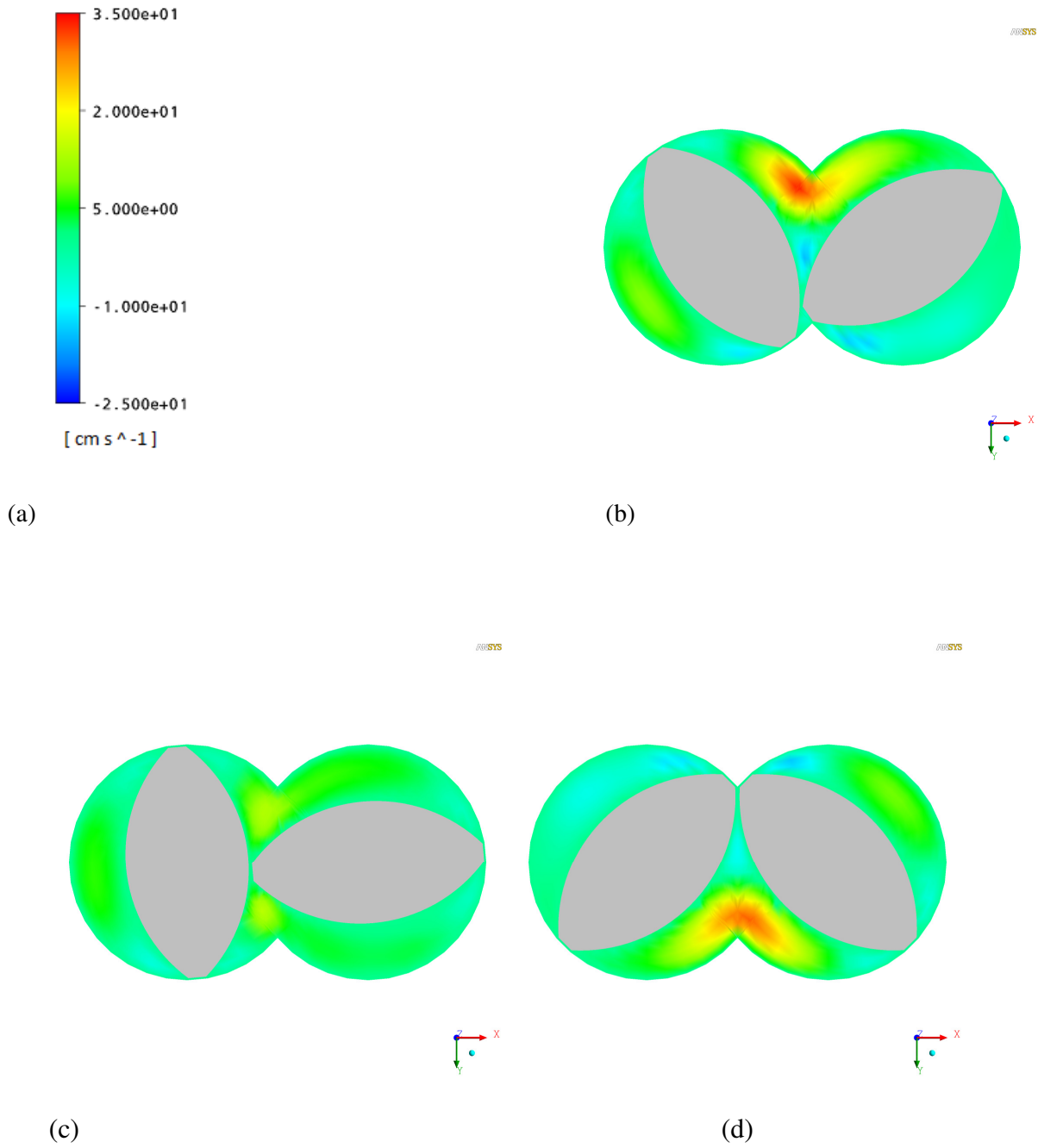


Figure 4.9: Contour maps of axial velocity (V_z) at P4 in the 45F configuration (a) time step 1, 10° rotation (b) time step 4, 40° rotation and (c) time step 9, 90° rotation.

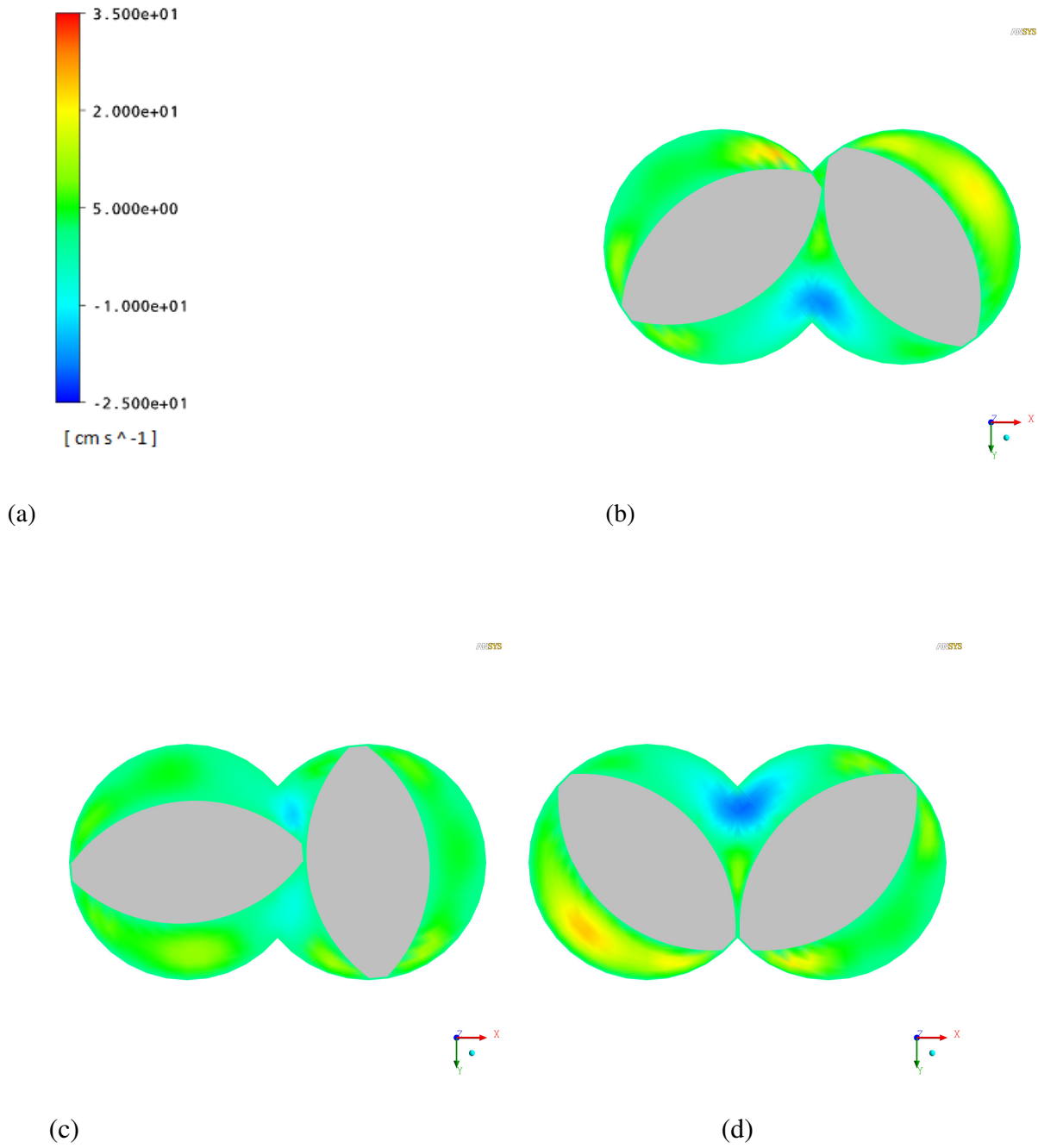
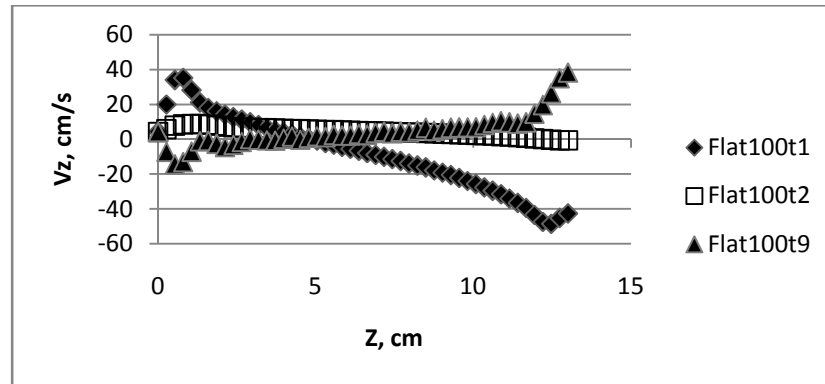


Figure 4.10: Contour maps of axial velocity (V_z) at P4 in the 45R configuration (a) time step 1, 10° rotation (b) time step 4, 40° rotation and (c) time step 9, 90° rotation.

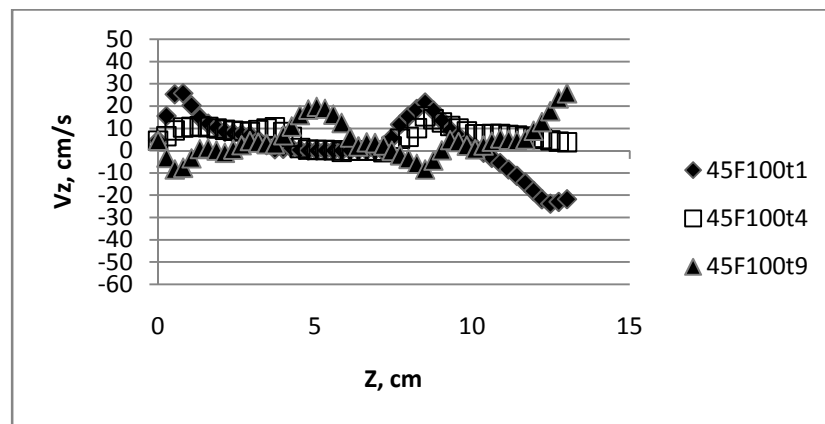
Figures 4.8 to 4.10 show contour maps of the local axial velocity flow (V_z) on the XY cross-sectional plane at the 4th paddle pair location at times steps 1, 4 and 9. In the FLAT configuration, only a slight increase in the axial velocities is seen in the 'C' shaped region between the paddle elements and the barrel wall and no significant regions of increased forward or backward flow are seen in the intermeshing regions between the paddle elements over all the times steps. This confirms that most of the axial flow in the FLAT configurations happens through the 'C' shaped region between the paddle elements and the barrel wall in comparison to the intermeshing region. In the 45F configuration, at the P4 region, which is the beginning of the staggered region, high values of forward axial flow are concentrated in the intermeshing region between the paddle elements at all the three time steps. A similar distribution of backward flow is seen in the intermeshing region for the reverse 45R configuration at all the time steps. This result again points to the increased local forward flow and backflow channels created in the intermeshing region due to the stagger in the paddles. The amount of local backflow in the reverse stagger configuration is somewhat lesser than the amount of increased local forward flow regions found in the same regions for the forward stagger configuration due to the net axial flow imposed in the +Z direction that acts on reducing the backflow intensity. As a direct result of this, there is significantly greater axial flow in the C-shaped region between the paddle element and the barrel wall compared to the forward 45F.

The local axial velocities in the intermeshing region throughout the barrel volume were computed along a line running through the nip region in the Z direction for the three time steps. Figure 4.11 show the evolution of V_z along this line from time step 1 through

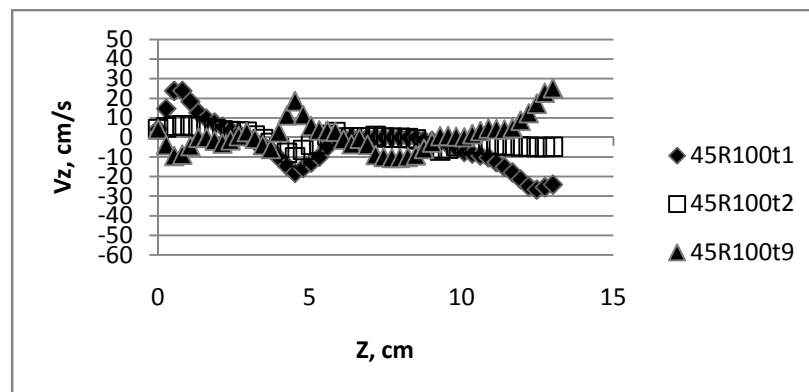
9 for the three configurations. In all the three configurations, the axial velocity went from positive at time step 1 to neutral at time step 4 to negative values at time step 4 at the beginning of the mixing region ($z = 0$ to 4 cm; inlet boundary plane to P3). A converse common trend towards the end of the mixing region ($z = 9$ to 13.8 cm; P8 to outlet boundary plane) where the axial velocity magnitudes increased from negative to positive. This shows the pumping action of the non-staggered region involving periodic cycles of forward and backward flow. Significant influence of the stagger can be seen in middle of the mixing region ($z = 4$ to 9 cm; P4 to P7). While the FLAT configuration showed continuous transition of the axial velocity along the axial length, the forward 45F showed increased local forward flow and the reverse 45R configuration showed increased backward flow at all the time steps.



(a)



(b)



(c)

Figure 4.11: Axial velocity (V_z) along a line running through the nip region of the mixer

(a) FLAT (b) 45F and (c) 45R configuration.

4.2 PART II. Evaluation of dispersive mixing in the Readco continuous mixer

The flow data was recorded at each time step for the 3,000 points in the barrel volume mesh. The average values of shear rate and dispersive mixing were calculated from the cumulative data at these points in the barrel for the first 9 time steps as earlier. Hence this data is inclusive of all the variations in the flow in the mixer barrel volume that can possibly be encountered by bubbles or drops traversing the volume of the mixer in several rotations of the paddle elements. Of specific interest to us is the variation in the density of these points which show a ‘dispersive mixing’ character. One criterion for dispersive mixing is for the flow type (dispersive mixing index, λ_{MZ}) to be greater than 0.6, where the flow has a greater elongation component favorable for breakup of drops and bubbles (Grace, 1982; Bentley and Leal, 1986; Meijer and Janssen, 1994). In order to determine the local areas in the mixer which contribute to dispersion, shear rate and dispersive mixing index (λ_{MZ}) were evaluated over XY planar cross-sections along the axial length of the mixer. The XY cross-sections (perpendicular to the axial flow axis, Z) were centred at the 1st, 4th and the 8th paddle elements (P1, P4 and P8), representing the beginning, middle and the end of the mixing region respectively. The flow information on each cross-section is representative of the flow in the immediate local volume surrounding the cross-sectional plane (+/- one paddle element). Likewise to the global analysis, the flow information over cross-sectional planes was collected for 9 time steps and average values of the cumulative data are reported.

Paddle Configuration	Shear Rate, $\dot{\gamma}$ (all points)	Dispersive Mixing Index, λ_{MZ} (all points)	Shear Rate, $\dot{\gamma}$ (points with $\lambda_{MZ} > 0.6$)	Dispersive Mixing Index, λ_{MZ} (points with $\lambda_{MZ} > 0.6$)
FLAT	88.90	0.51	74.75	0.69
45F	76.88	0.49	51.79	0.67
45R	81.46	0.49	56.31	0.68
FLAT P1	78.21	0.46	50.96	0.70
45F P1	73.64	0.46	50.63	0.70
45R P1	73.13	0.46	50.47	0.70
FLAT P4	87.69	0.50	74.70	0.72
45F P4	73.97	0.50	50.63	0.70
45R P4	82.01	0.50	63.68	0.67
FLAT P8	93.60	0.49	64.58	0.69
45F P8	77.25	0.50	56.50	0.70
45R P8	79.07	0.50	57.44	0.71

Shear Rate units, 1/s; Dispersive Mixing Index, dimensionless

Table 4.2 Average values of shear rate and dispersive mixing index λ_{MZ} , cumulated over nine time steps for the entire mixer volume and specific X-Y cross sectional planes for a screw speed of 100 RPM.

Table 4.2 shows a comparison of the average values of the shear rate and the dispersive mixing index λ_{MZ} , as a function of the paddle configuration at 100 RPM, over the entire mixer volume and over the three specific X-Y cross-sectional planes, P1, P4 and P8. The average values were calculated first including all the points in the respective domains and a second time including only those points which show an elongation flow

character and are likely to influence dispersive mixing ($\lambda_{MZ} > 0.6$). The overall average shear rate value was highest for the FLAT configuration and lowest for the forward staggered 45F configuration. The overall average values of λ_{MZ} were close to 0.5 indicating a simple shear type of flow for a bulk of the material during one rotation of the paddles. This result is in agreement with previously reported average values of the dispersive mixing index close to 0.5 in the kneading block region of a twin-screw extruder, independent of the kneading block design. It was also reported previously that the average value of stress and dispersive mixing index did not vary from one time step to another (Yang and Manas-Zloczower, 1992; Cheng and Manas-Zloczower, 1997). For points in the elongation flow regions, while the average value of the dispersive mixing index did not vary significantly with the paddle configuration, the FLAT configuration showed significantly higher average shear rate compared to the staggered configurations. This indicates better dispersive mixing of the FLAT configuration caused by more points in the mixing volume with favourable values of *both* the flow strength and the flow type. A look at the specific axial locations shows the higher shear rate values for the FLAT configuration in the middle (P4) and the end (P8) of the mixing region.

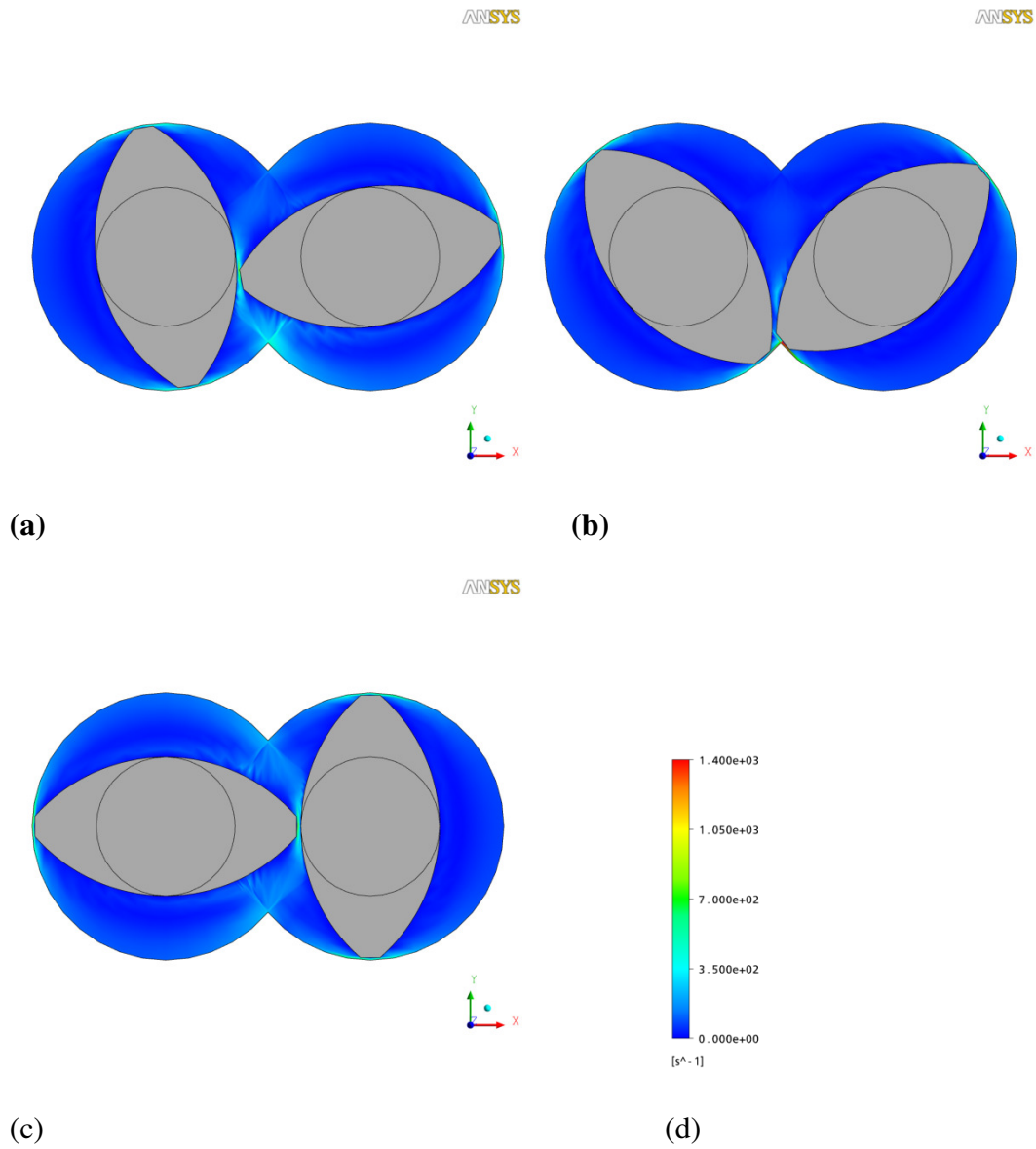


Figure 4.12 Contour maps of shear rate over XY cross-sectional planes at the 4th paddle element (P4) for FLAT configuration at 100 RPM (a) time step 1 (b) time step 4 (c) time step 9 (d) Legend.

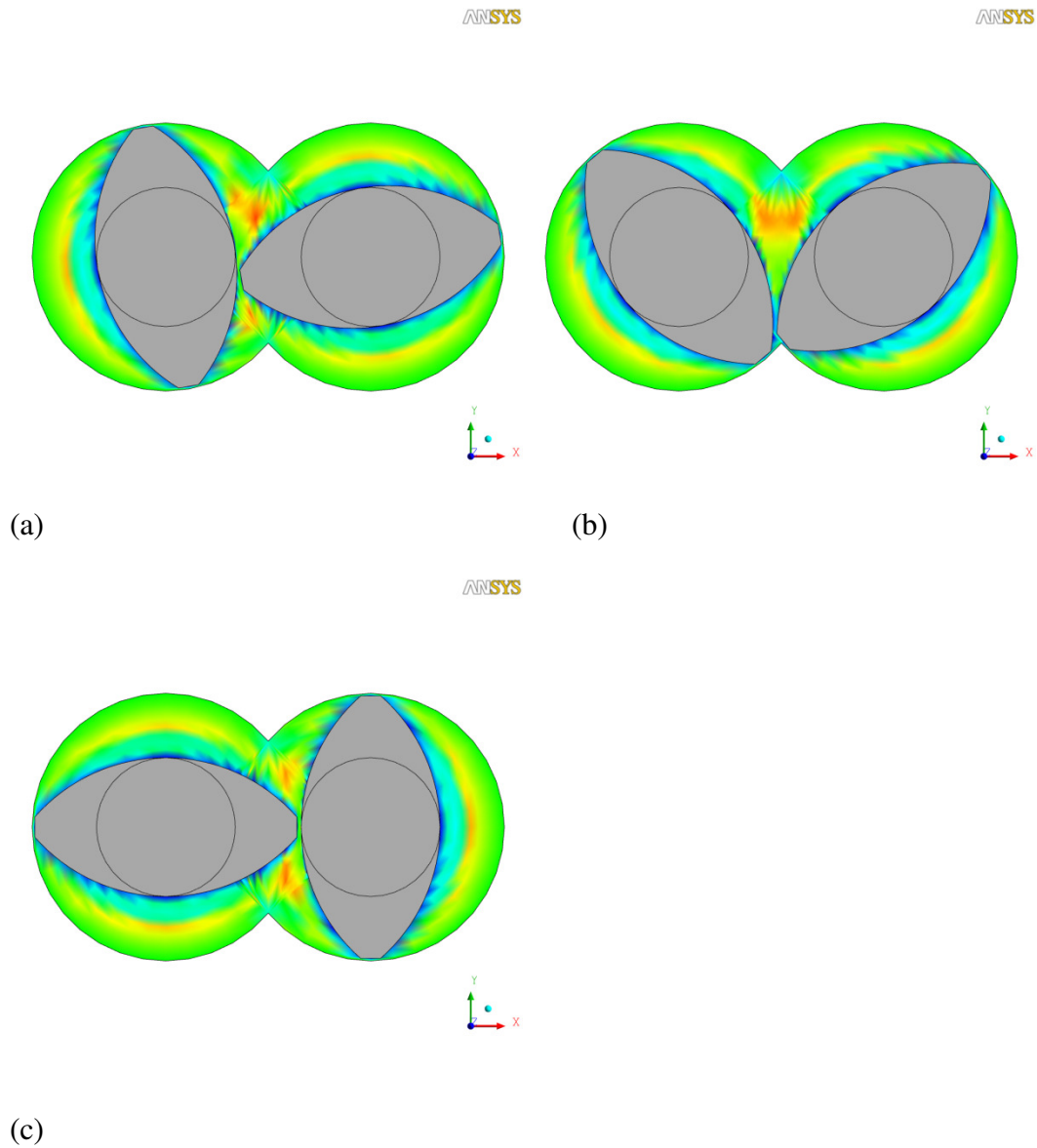


Figure 4.13 Contour maps of dispersive mixing index λ_{MZ} , over XY cross-sectional planes at the 4th paddle element (P4) for FLAT configuration at 100 RPM (a) time step 1 (b) time step 4 (c) time step 9. Legend – yellow to red shades show predominantly elongation flow, green shades are predominantly shear and blue shades are predominantly rotation.

Figure 4.12 shows the contour maps of shear rate over the XY cross-sectional planes at the 4th paddle element (P4) for FLAT configuration at 100 RPM. The shear rate gradient seen can be broadly categorized into three areas with the average value of the shear rate covering the majority of the entire volume (blue shades). The highest values of shear rate (red shades) are seen in nip the regions between the paddle tip and the barrel surface. The next level of high shear rate values (green shades) can be seen in the intermeshing region between just above and below the paddle surface and in the nip region between the two paddle elements (at time step 4). Figure 4.13 shows the corresponding X-Y contour maps of the dispersive mixing index at the 4th paddle element location for the three time steps.

The flow type can be broadly categorized into three regions with the majority of the volume showing a simple shear character (green shades). The highest values of λ_{MZ} (red shades) can be seen in the intermeshing regions above and below the paddle element surfaces and in the middle of the C-shaped region between the barrel surface and the paddle elements. It is interesting to note that these regions of elongation flow are not seen in the nip regions between the paddle tips and the barrel surface, which showed the highest shear rates values as seen earlier in figure 4.12. A third region of rotation flow (blue shades) is seen in regions immediately around the rotating paddle surfaces. While the pattern of these regions is similar to that reported by Connelly and Kokini (2007), the plug-flow or rotation-flow region reported by them was much larger, clearly due to the absence of axial flow and the low screw speed of 1 RPM. It was reported previously that the *average* value of stress and dispersive mixing index did not vary from one time step to another (Yang and Manas-Zloczower, 1992; Cheng and Manas-Zloczower, 1997).

However, a look at the contour maps shows the specific regions in the mixer volume with favourable dispersive mixing conditions. Particularly, the incidence of elongation flow in the intermeshing region will be a critical factor for the dispersive mixing ability given the corresponding high shear rates in this region.

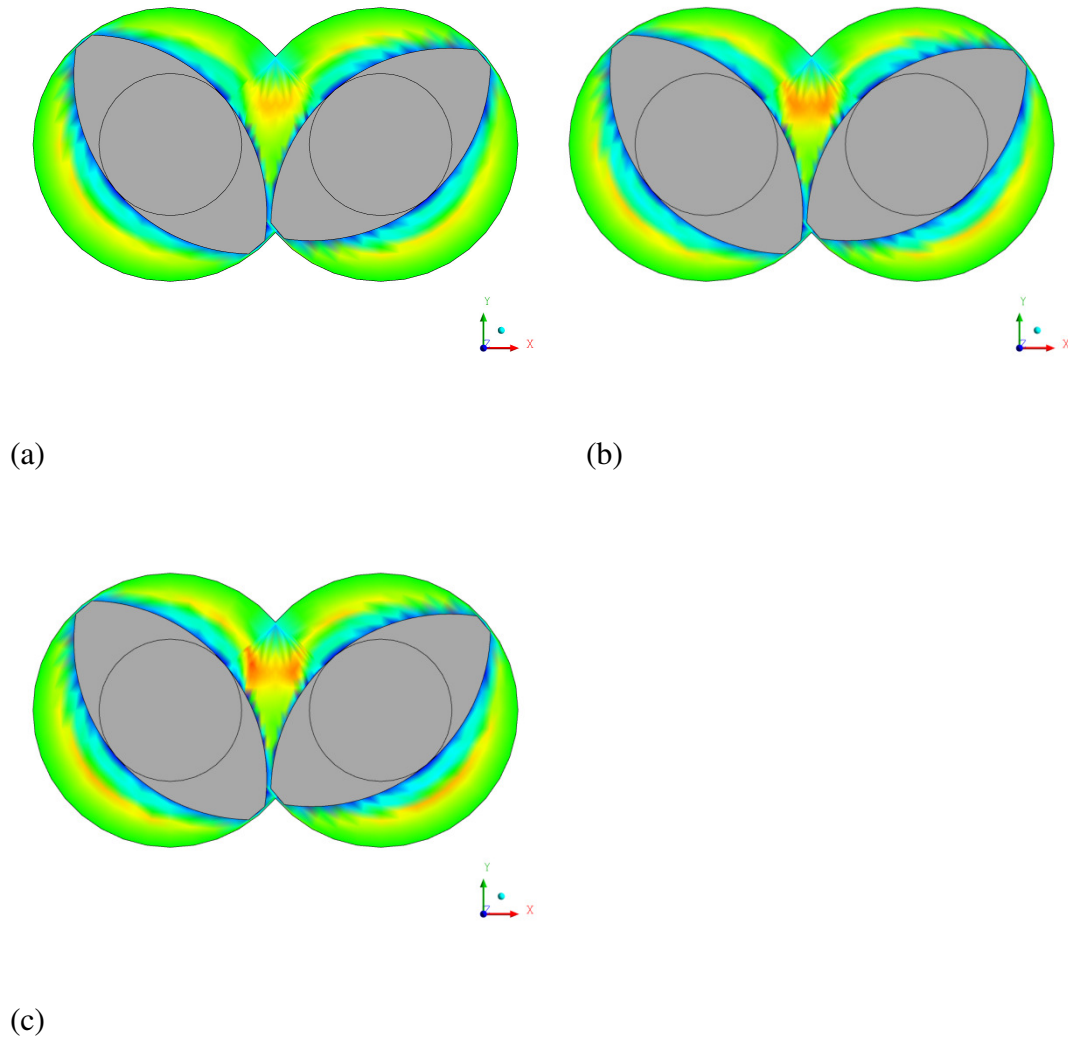


Figure 4.14 Contour maps of dispersive mixing index λ_{MZ} , over three XY cross-sectional planes at time step 4 for FLAT configuration at 100 RPM (a) P1(b) P4 (c) P8 . Legend – yellow to red shades show predominantly elongation flow, green shades are predominantly shear and blue shades are predominantly rotation.

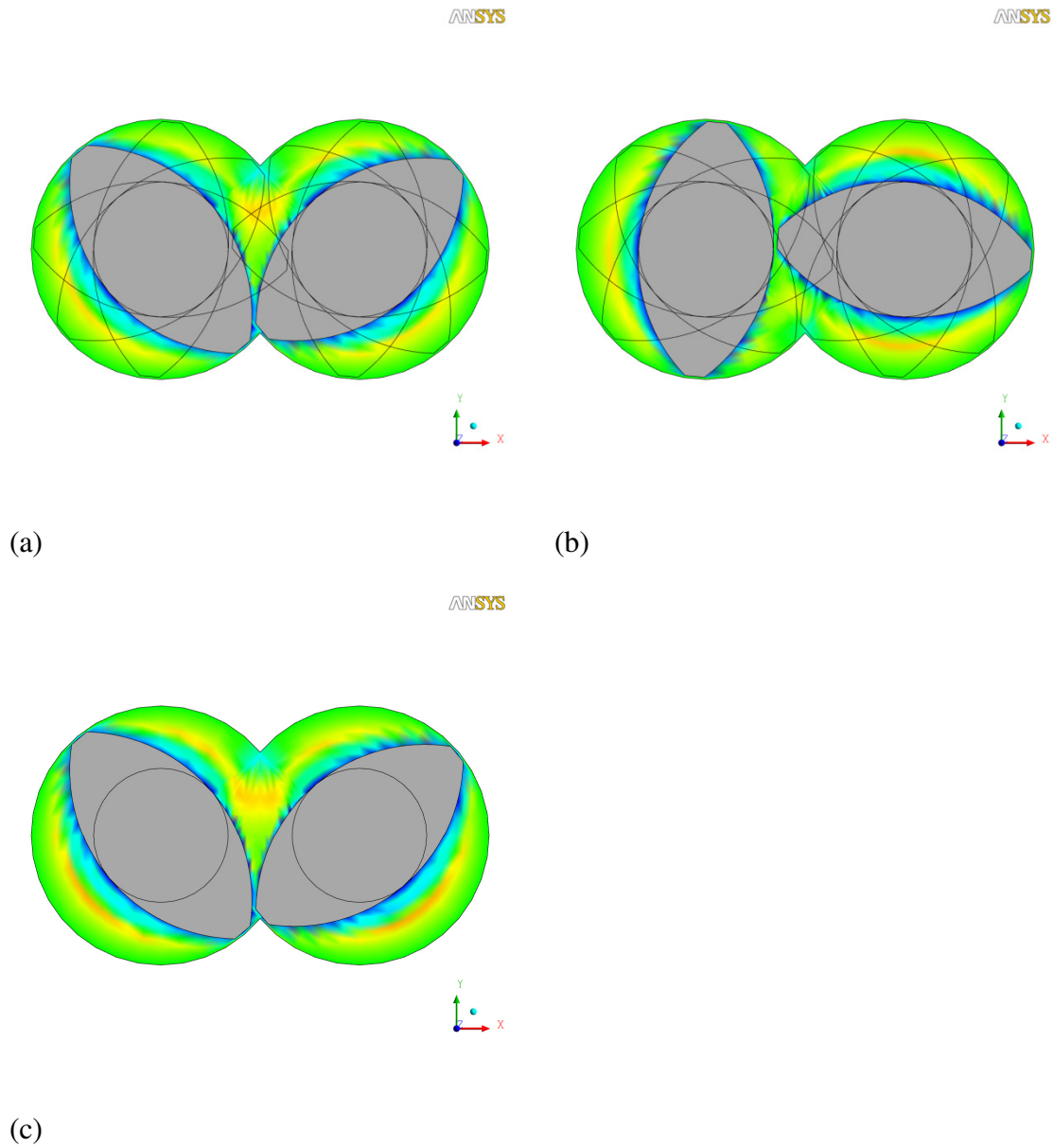


Figure 4.15 Contour maps of dispersive mixing index λ_{MZ} , over three XY cross-sectional planes at time step 4 for 45F configuration at 100 RPM (a) P1(b) P4 (c) P8 . Legend – yellow to red shades show predominantly elongation flow, green shades are predominantly shear and blue shades are predominantly rotation.

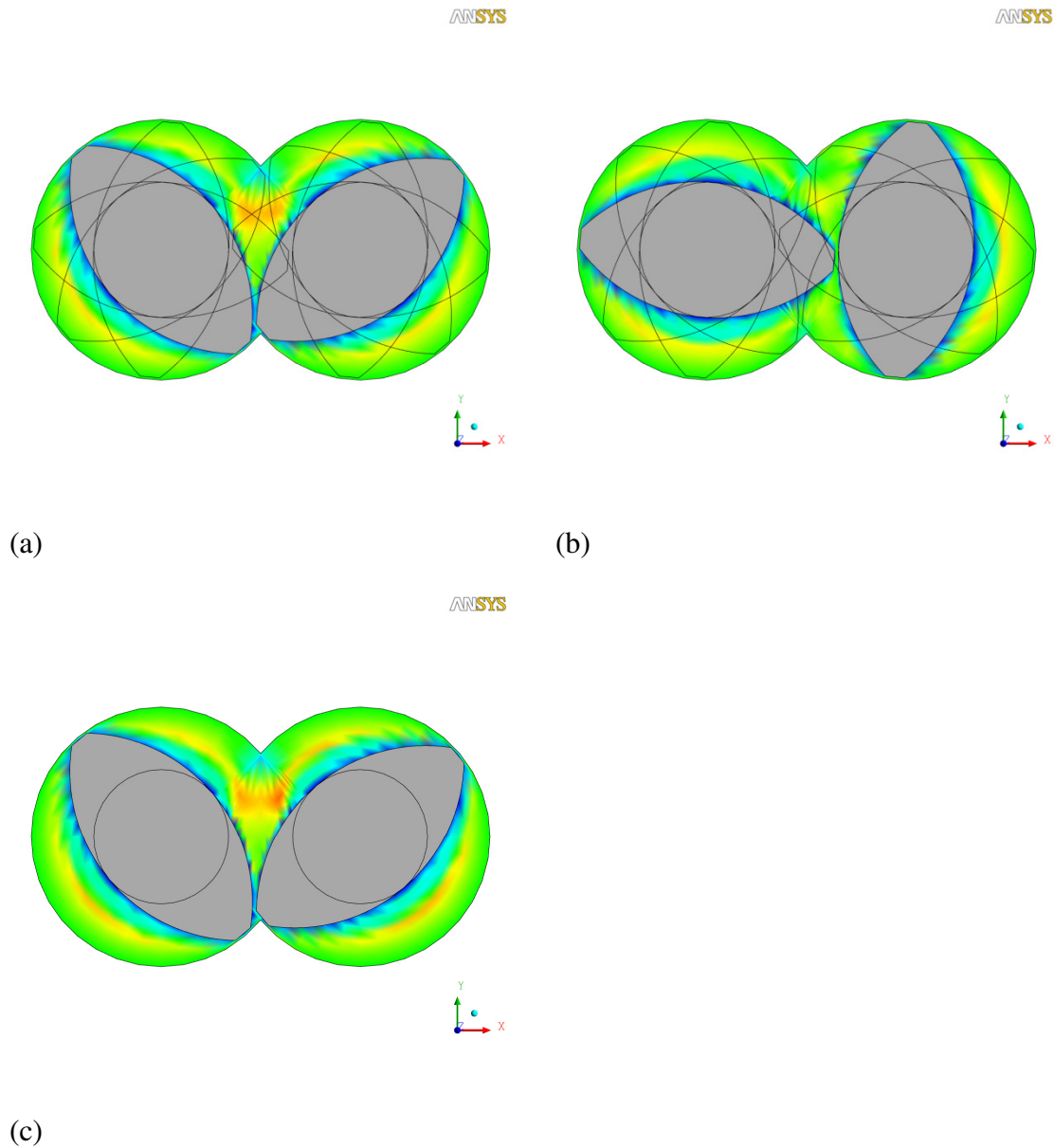


Figure 4.16 Contour maps of dispersive mixing index λ_{MZ} , over three XY cross-sectional planes at time step 4 for 45R configuration at 100 RPM (a) P1(b) P4 (c) P8 .Legend – yellow to red shades show predominantly elongation flow, green shades are predominantly shear and blue shades are predominantly rotation.

A comparison of the flow type distribution at time step 4 over the three axial locations in the mixer for the three paddle element configuration at is shown in figures

4.14 to 4.16. For the FLAT configuration, the intensity of elongation flow is high in the intermeshing region at all the axial locations, with the P4 and P8 locations showing slightly higher intensity compared to the P1 location. The difference in the elongation flow intensity in the intermeshing region is significant for both the staggered configurations, where almost no elongation flow is seen in the intermeshing region at the P4 location, which is the first paddle element in the staggered section of the configuration. The intensity of elongation flow at P1 and P8 for 45F forward stagger configuration was significantly lower compared to FLAT configuration had, while the 45R reverse stagger configuration had higher intensity of elongation flow at P1 and similar intensity at P8 compared to the FLAT configuration.

This shows that the introduction of stagger, causing a disruption in the continuity of axial flow, decreased the intensity of elongation flow in the region of stagger. The flow in the intermeshing region of the FLAT configuration can be thought of as a 'squeeze flow' caused by paddle surfaces moving in opposing directions. As the right paddle element pushes the material upwards the left paddle element pushes it down, the combined action causes the material to be squeezed out of the intermeshing gap. This is similar to flow created in the region between the rollers of a four-roll mill that was previously used in drop breakup studies to create pure elongation flow (Grace, 1982; Bentley and Leal, 1986). The stationary barrel wall surfaces directly above the intermeshing region act as the remaining two rolls. This effect is aided in the FLAT configuration due to the absence of stagger creating an effective length of the 'roller' like surfaces equal to thickness of 9 paddle elements (Figure 4.17). With the introduction of stagger, this effect is reduced to a 3 element length region at the beginning and the end of

the mixing region where P1 and P8 are located and still show elongation flow. However, a single paddle element length in the region of stagger (P4) does not seem to be sufficient to create a squeeze flow between the elements. This effect is illustrated in figure 4.18 which shows the velocity vectors in the three paddle element configurations at time step 4, colour coded with the magnitude of the dispersive mixing index, λ_{MZ} . Figure 4.19 shows the evolution of flow over the three time steps along a hypothetical Z axial line passing through the intermeshing region. The values of dispersive mixing index along the line are plotted for the three time steps 1, 4 and 9. It can be seen that for the FLAT configuration, the values of λ_{MZ} vary only with the relative position of the paddle elements and are independent of the axial location. The highest value of λ_{MZ} (~ 0.8) is seen at time step 4 where the paddles are positioned to cause a predominantly elongation flow, as noted earlier. For the staggered configuration, the trend in the first three and the last three non-staggered paddle regions was similar to that of FLAT while the trend was disrupted in the region of stagger.

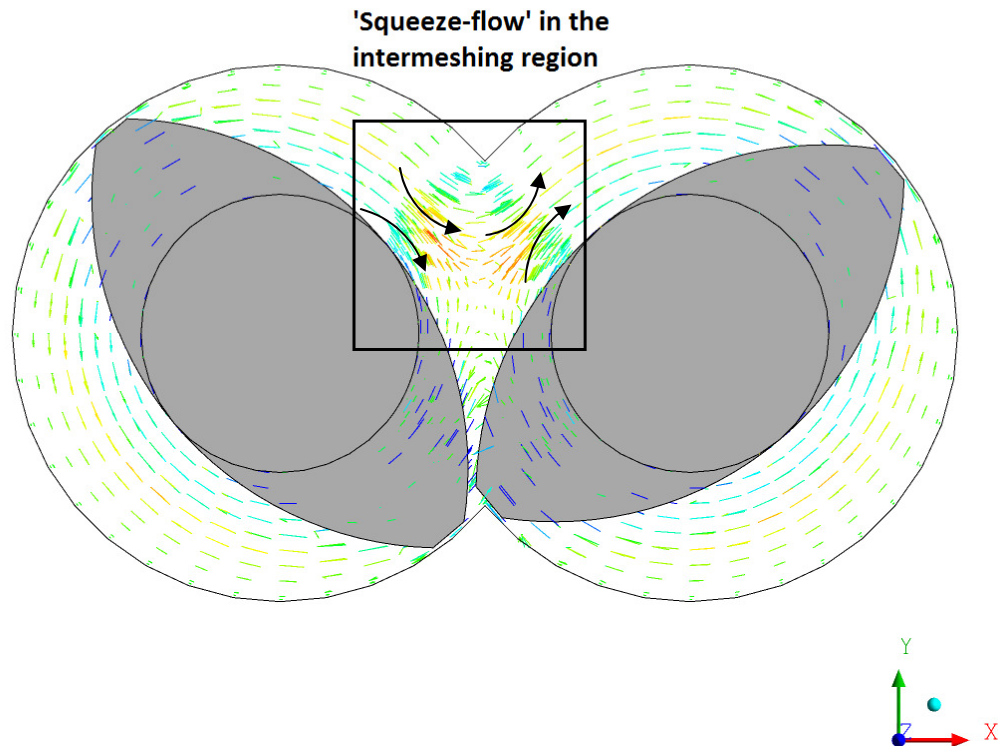


Figure 4.17 Illustration of 'Squeeze flow' in the intermeshing region between the paddle element surfaces and barrel wall surfaces causing a predominantly elongation flow.

Legend – yellow to red shades show predominantly elongation flow, green shades are predominantly shear and blue shades are predominantly rotation.

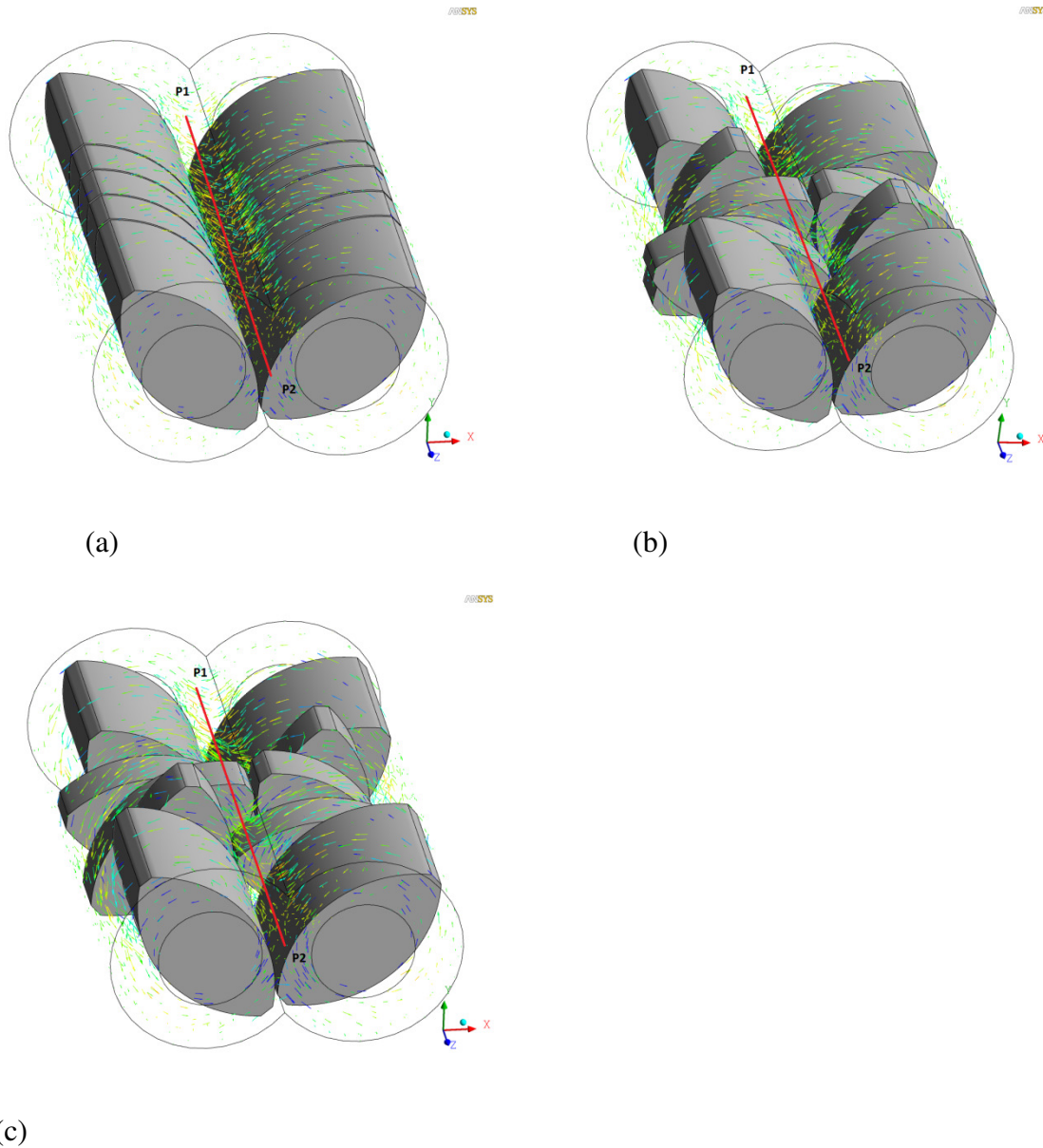
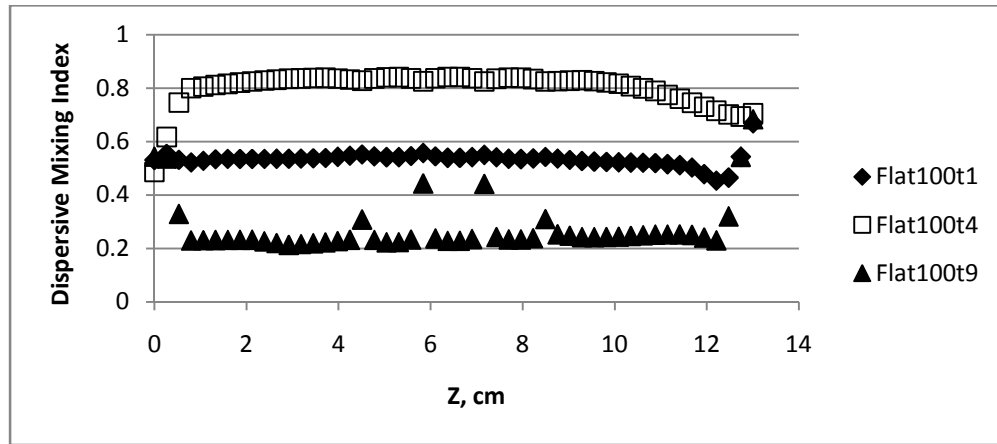
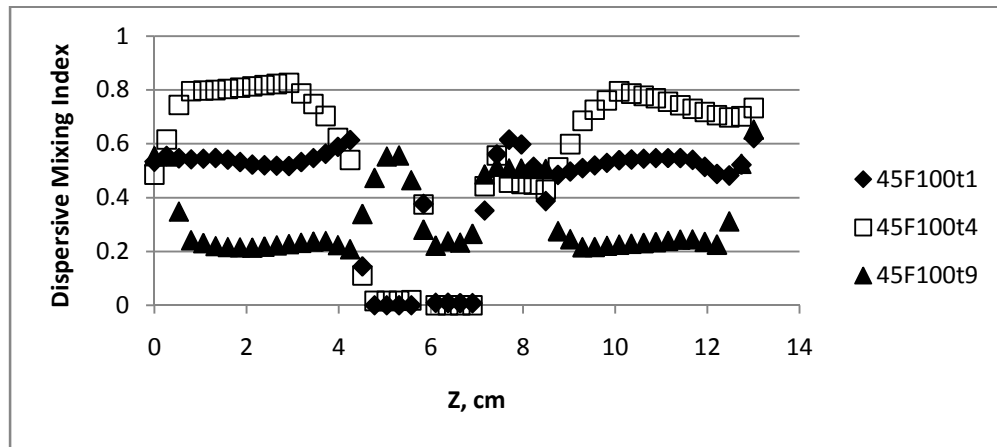


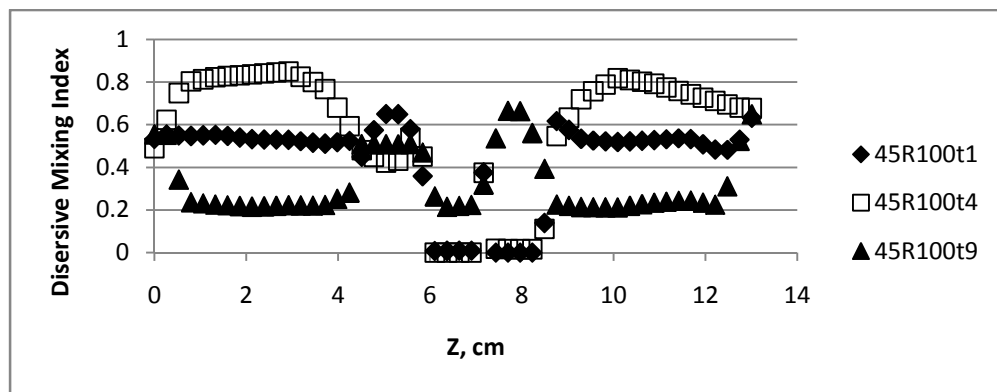
Figure 4.18 Dispersive mixing in the mixer volume at time step 4 shown by colour coding the velocity vectors with the magnitude of dispersive mixing index λ_{MZ} , at 100 RPM (a) FLAT (b) 45F (c) 45R (d) Legend – yellow to red shades show predominantly elongation flow, green shades are predominantly shear and blue shades are predominantly rotation.



(a)



(b)



(c)

Figure 4.19 Magnitudes of dispersive mixing index λ_{MZ} , along a line connecting P1 (0, 0.8, 0) to P2 (0, 0.8, 13.8) at 100 RPM (a) FLAT (b) 45F (c) 45R

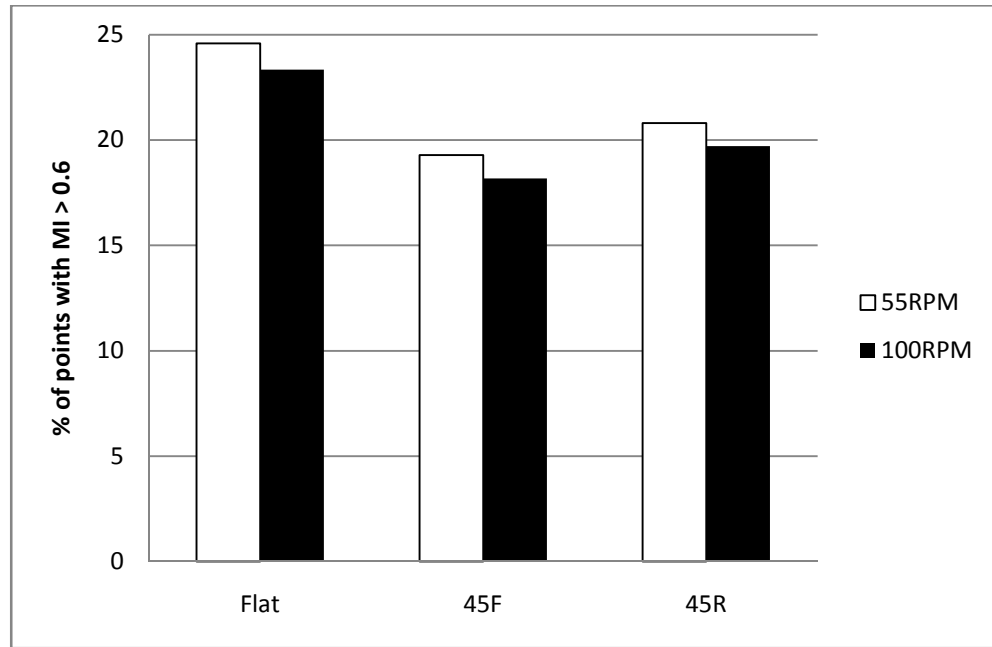


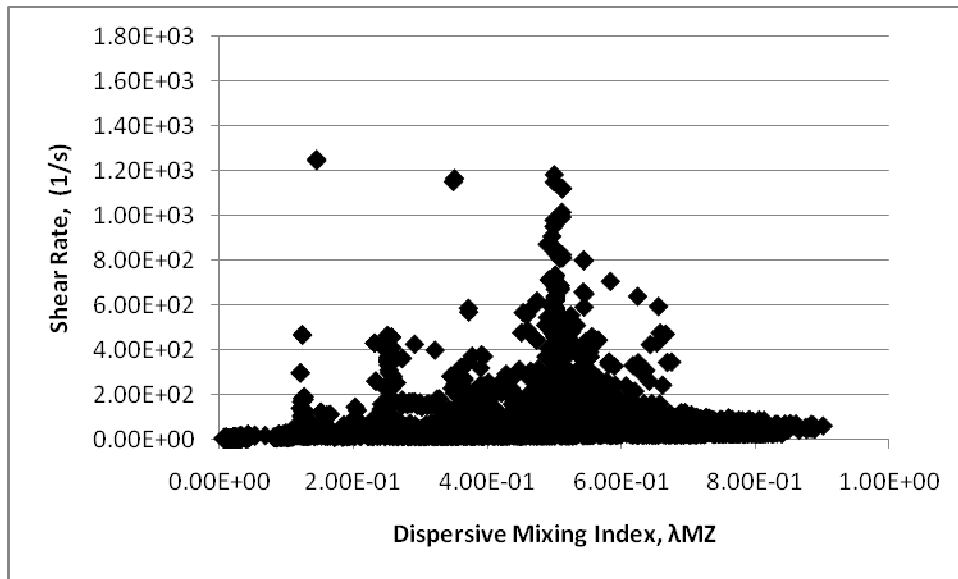
Figure 4.20 Density of elongation flow in the mixer volume as a function of paddle configuration and screw speed.

Figure 4.20 shows the variation of density of all points with the dispersive mixing index $\lambda_{MZ} > 0.6$ as a function of screw speed and paddle element configuration. The FLAT paddle configuration shows the highest percentage of points with elongation character while a stagger in the paddle elements (45F and 45R) considerably lowered the incidence of such points and for each given paddle configuration, the screw speed seems to have negligible effect on the incidence of elongation flow type.

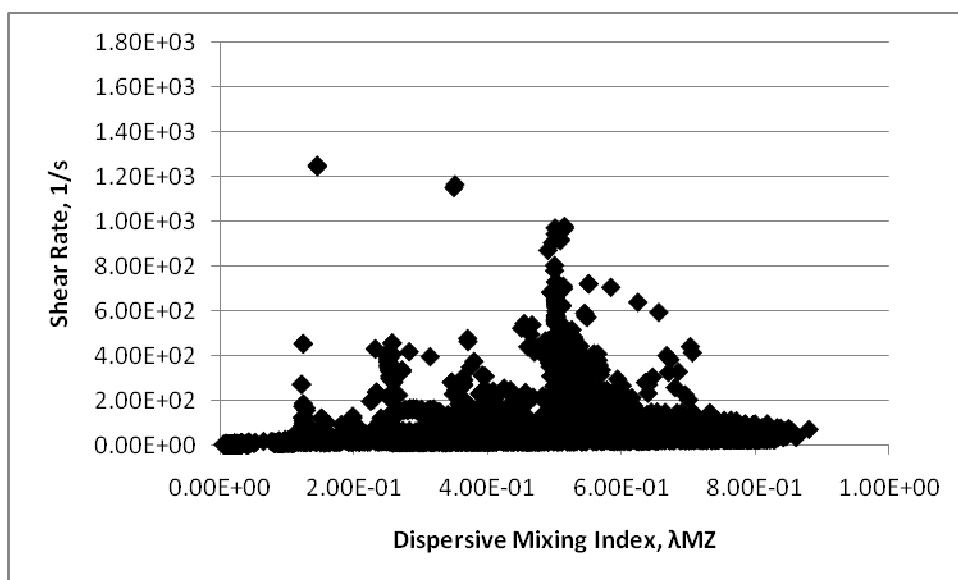
4.3 PART III. Evaluation of air bubble dispersion in the Readco continuous mixer

4.3.1. Evaluation of local shear rates and capillary number distributions

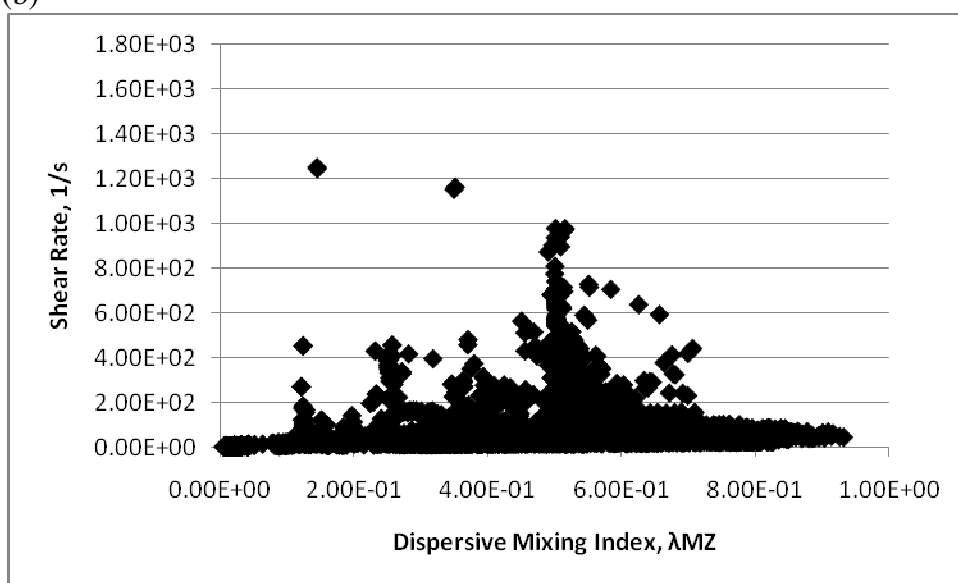
Figure 4.21 shows the typical distribution of local shear rate and dispersive mixing index (λ_{MZ}) over an XY cross section at the beginning of the mixing region (P1) for the three screw configurations cumulated over nine consecutive time steps. This distribution pattern is typical of all cross-sectional locations in the mixer with only the density of points in elongation flow and the magnitudes of local shear rate varying across the XY plane. The highest shear rate values are found in the simple shear flow region ($\lambda_{MZ} = 0.5$) while the shear rate values are much lower in the regions where elongation flow is predominant ($\lambda_{MZ} > 0.6$), closer to the average over the cross-sectional plane.



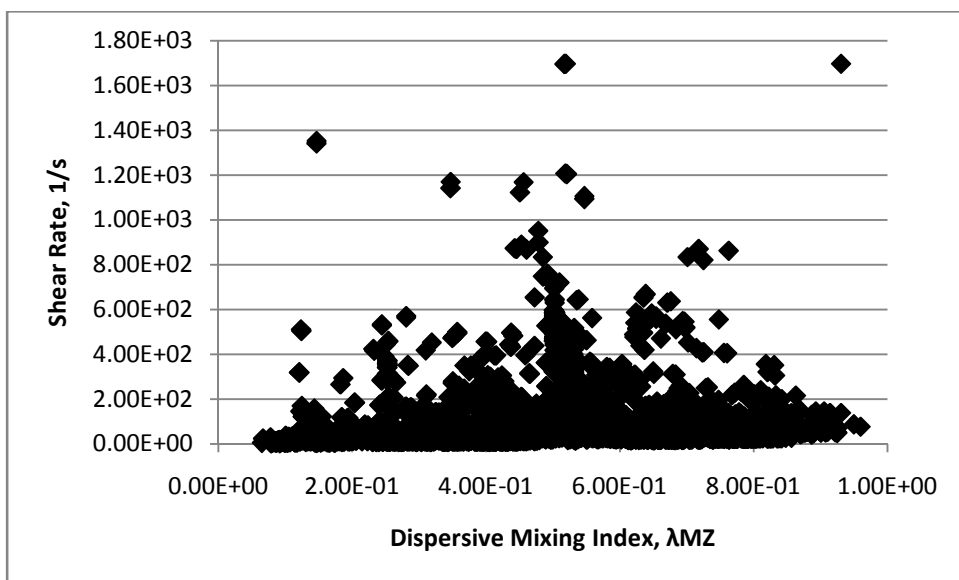
(a)



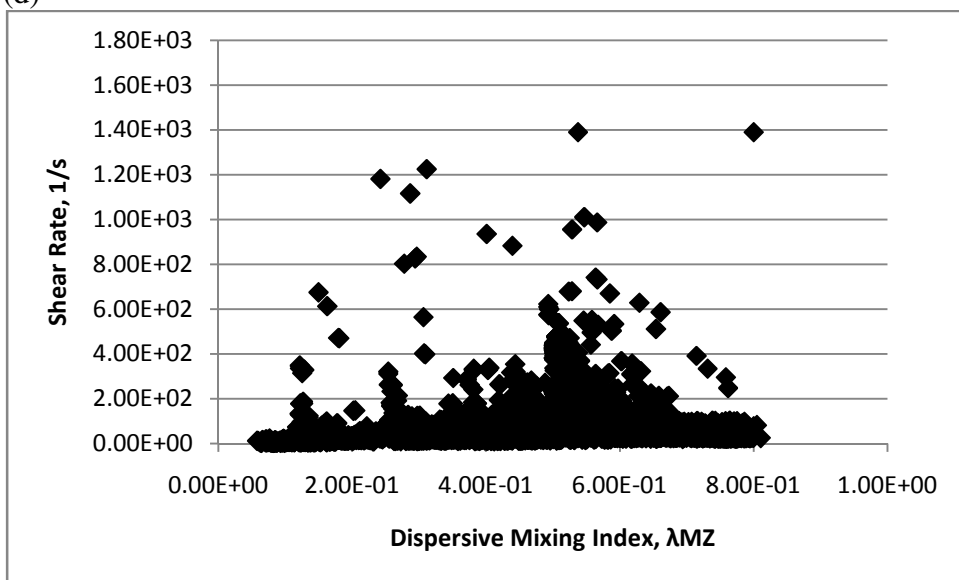
(b)



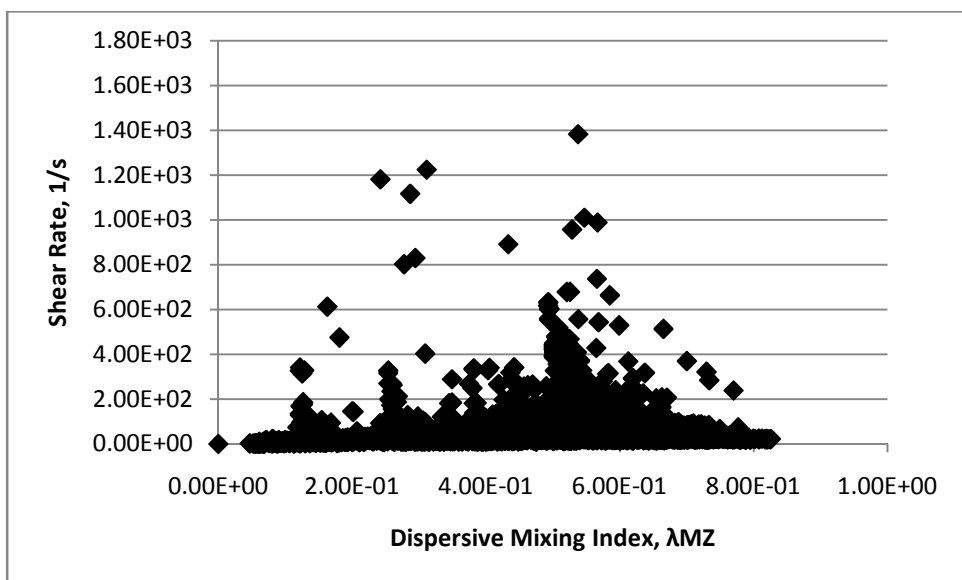
(c)



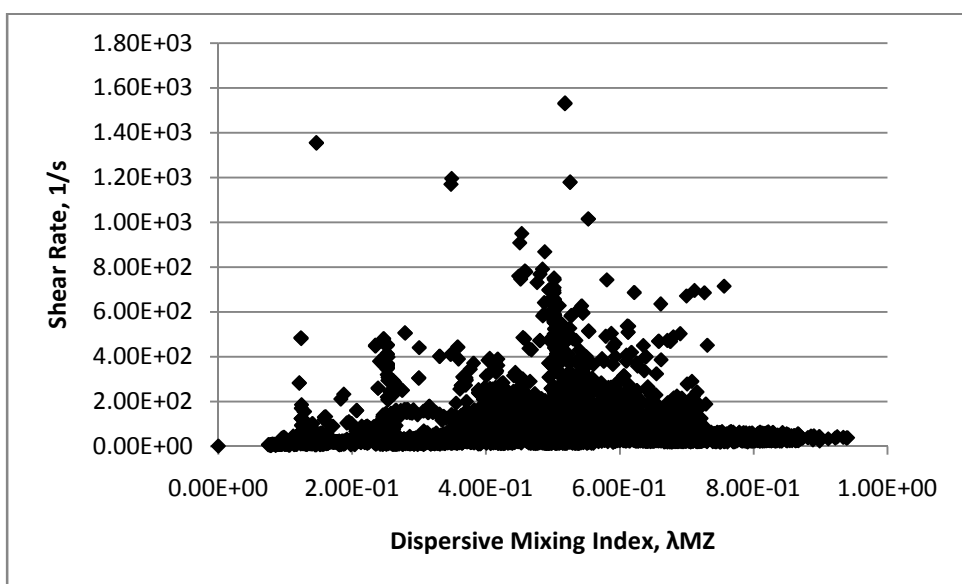
(d)



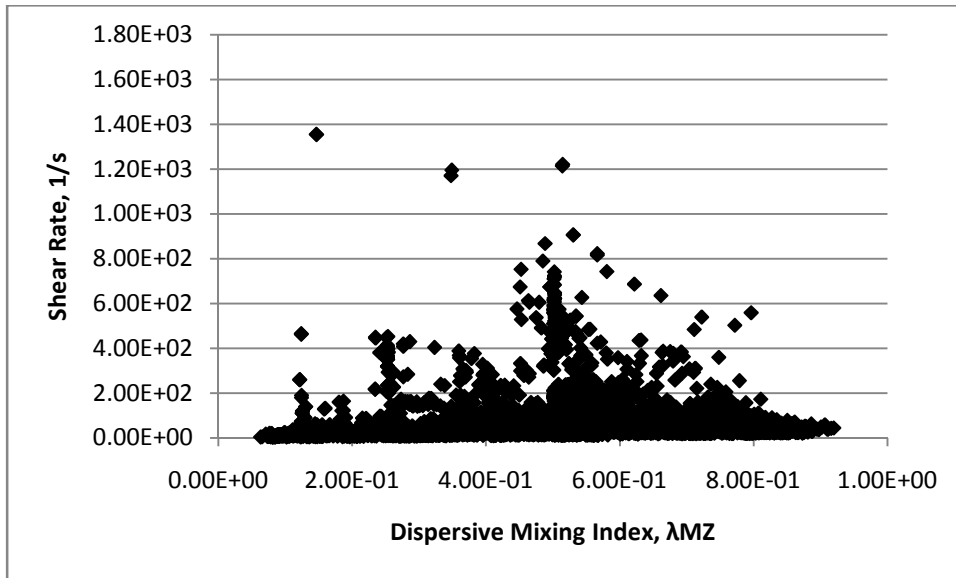
(e)



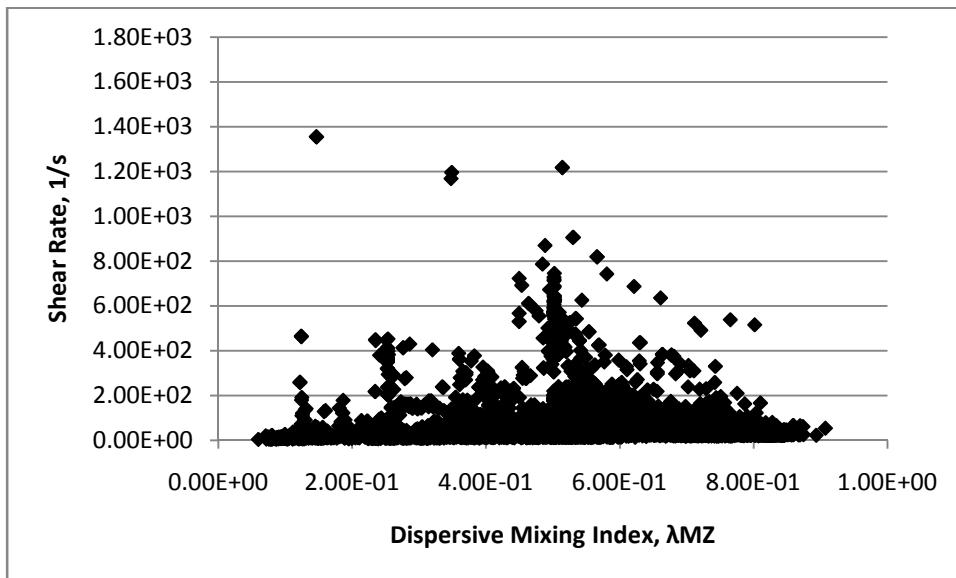
(f)



(g)



(h)



(i)

Figure 4.21 Distribution of local shear rate and dispersive mixing index for the three screw configurations at 100 RPM cumulated over 9 time steps over XY cross-sections (a) FLAT P1 (b) 45F P1 (c) 45R P1 (d) FLAT P4 (e) 45F P4 (f) 45R P4 (g) FLAT P8 (h) 45F P8 (i) 45R P8.

Table 4.3 shows the average shear rate values at the different paddle element locations in the mixing region calculated from all points on the different cross-sectional planes at screw speeds of 55 RPM and 100 RPM. As expected, increasing the screw speed from 55 to 100 RPM resulted in higher average shear rates at all locations in the mixer for all the paddle element configurations. As described in Figure 5.21, the average shear rate values for the points with an elongation flow character ($\lambda_{MZ} > 0.6$) are lower than the overall shear rate values. Apart from the effect of screw speed on the local average shear rates, the paddle element configuration and location in the mixer did not significantly affect the average shear rate values. For example, the range of the average local shear rates at 55 RPM was between 30.36 s^{-1} and 40.09 s^{-1} for all the paddle element configurations over all the locations, suggesting that the paddle element configuration has little effect on the flow strength. Thus while tracking bubble breakup in of a group of bubbles via changes in size distributions, it is critical to identify the density of the elongation flow that is responsible for bubble breakup within the range of shear rates encountered.

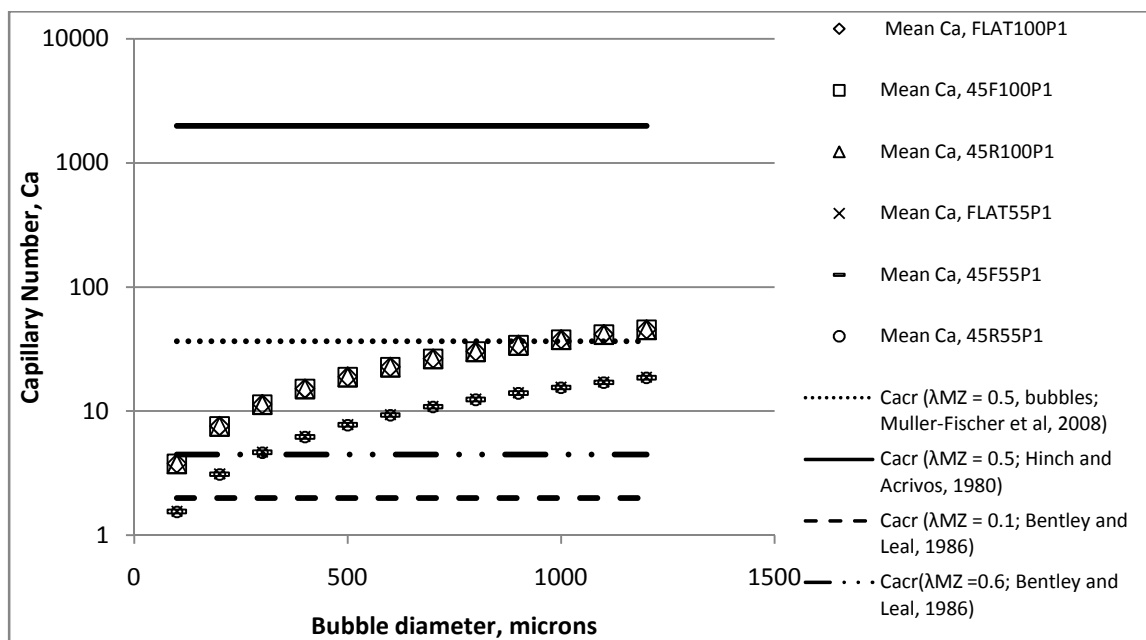
Paddle Configuration/ Location in the Mixer	Shear Rate from Cross-Sectional Planes at 100RPM, G_{mean} (all points)	Shear Rate from Cross-Sectional Planes at 100RPM, G_{mean} (points with $\lambda_{MZ} > 0.6$)	Shear Rate from Cross-Sectional Planes at 55RPM, G_{mean} (all points)	Shear Rate from Cross-Sectional Planes at 55RPM, G_{mean} (points with $\lambda_{MZ} > 0.6$)
FLAT P1	78.21	50.96	35.55	21.02
45F P1	73.64	50.63	39.77	30.81
45R P1	73.13	50.47	40.09	26.64
FLAT P4	87.69	74.70	32.46	20.88
45F P4	73.97	50.63	34.42	23.40
45R P4	82.01	63.68	38.18	23.30
FLAT P8	93.60	64.58	30.36	20.82
45F P8	77.25	56.50	34.77	26.27
45R P8	79.07	57.44	36.28	23.70

Shear Rate units, 1/s; Dispersive Mixing Index, dimensionless

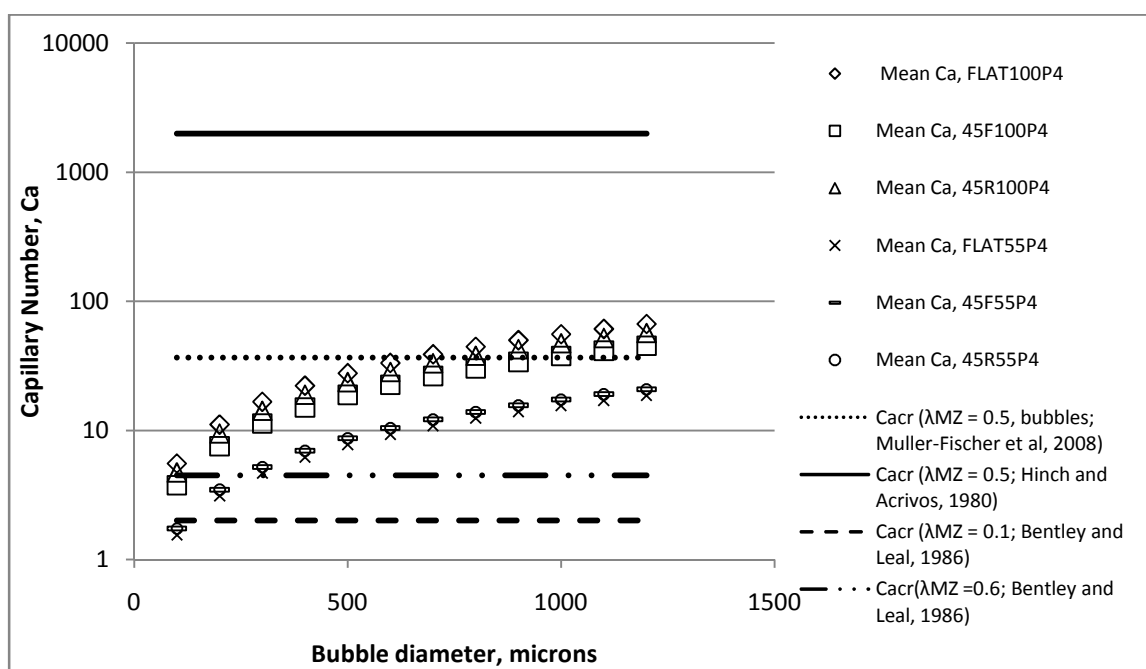
Table 4.3 Mean shear rate values calculated over cross-sectional planes at different locations in the mixer for the three paddle element configurations at 100RPM and 55RPM.

Figure 4.22 shows the comparison of Ca_{cr} from the different correlations with the actual Ca in the mixer calculated from the average shear rate values from Table 3.1 for bubbles between 100 and 1200 μm . The mean Ca for all the bubble diameters and paddle element configurations lie approximately in between the critical limits for bubble breakup in shear predominant and elongation predominant flows. At 100 RPM, the Ca values for

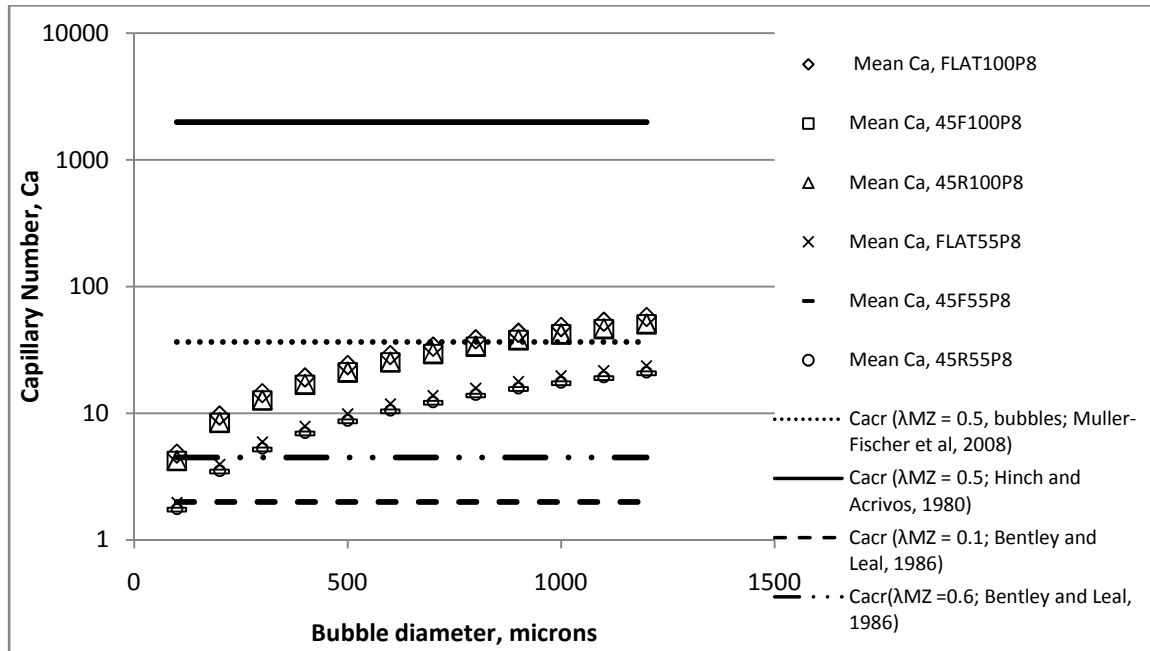
all the bubble diameters are higher than the Ca_{cr} for pure elongation flow while larger bubble diameters ($> 100\mu\text{m}$) have Ca values bordering the limit for Ca_{cr} in simple shear flow. At 55 RPM, the smallest bubbles have Ca values bordering the Ca_{cr} limit for predominantly elongation flow while all bubble diameters are below the Ca_{cr} limits for simple shear flow. Given that the limits of Ca_{cr} are approximate, it is clear from Figure 3.2 that flow type with $\lambda_{MZ} > 0.6$ (mixed and predominantly elongation) is the dominant flow type for bubble breakup at both screw speeds, with the possibility of the smallest bubbles ($< 300\ \mu\text{m}$) not breaking up at the lower 55 RPM screw speed even in predominantly elongation flow type.



(a)



(b)

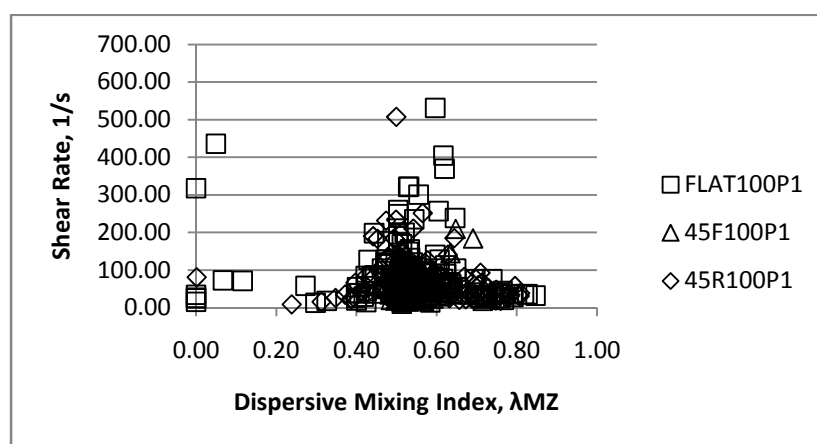


(c)

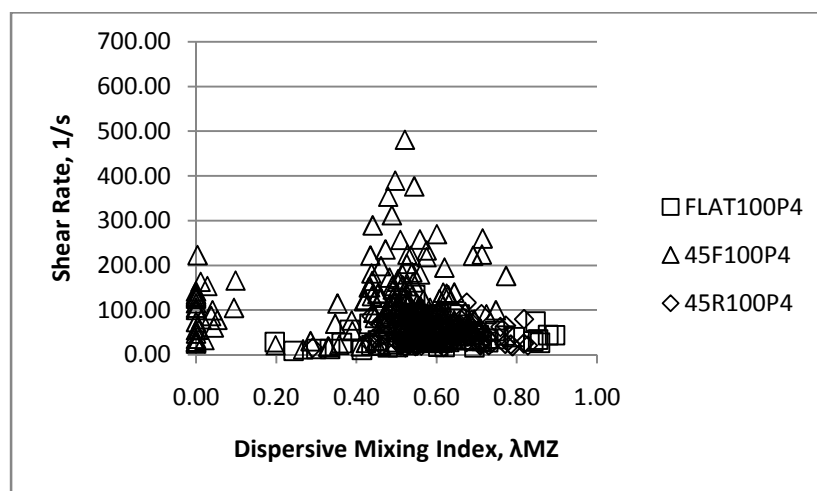
Figure 4.22 Mean Ca calculated for bubble diameters ranging from 100 μm to 1200 μm for the three paddle element configurations compared with the Ca_{cr} values for predominantly shear, predominantly elongation and mixed flows from literature at (a) P1 ($z = 1.27\text{cm}$) (b) P4 ($z = 5.15\text{ cm}$) and (c) P8 ($z = 10.46\text{ cm}$).

The dispersive mixing index (λ_{MZ}) was evaluated over points on 100 randomly generated trajectories falling on XY cross-sections at P1, P4 and P8. Figure 4.23 shows the density of elongational flow in terms of a % of the points with $\lambda_{MZ} > 0.6$. The overall elongational flow density was greater in the FLAT and 45R configurations compared to the 45F configuration. Regions of higher elongation flow in the twin screw mixer flow are seen when the material is pushed in between the paddle surfaces moving in opposite directions and the barrel wall causing an apparent ‘squeeze flow’. This effect is enhanced

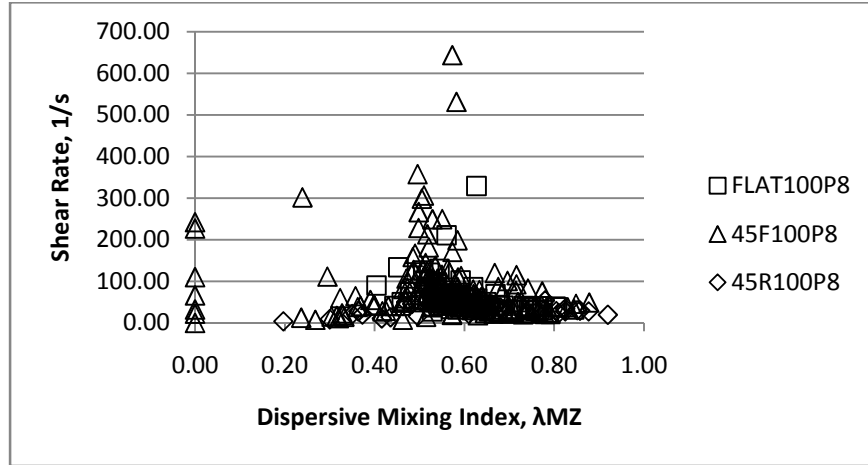
due to the absence of stagger in the FLAT configuration resulting in an increase in the length of the paddle surfaces moving in opposite direction (Vyakaranam and Kokini, 2012). In the 45R configuration the trajectory analysis shows that the presence of local reverse flow seems to cause some particles to be pushed back into the apparent squeeze flow domain between the paddle surfaces, while in the 45F configuration increased local forward flow results in most particles escaping the squeeze flow between the paddle surfaces, while in the 45F configuration increased local forward flow results in most particles escaping the squeeze flow between the paddle surfaces. Increased forward flow is especially seen in the P1 and P4 regions in the 45F configuration (Vyakaranam, et al., 2012).



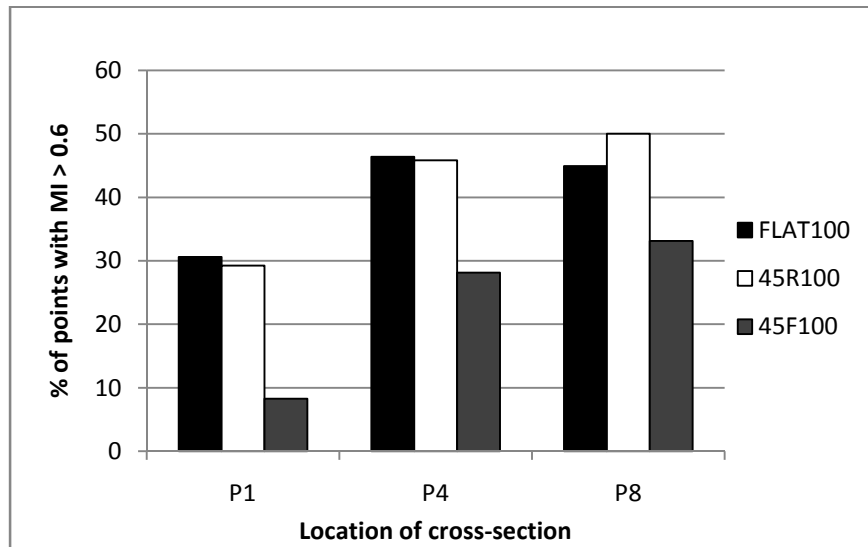
(a)



(b)



(c)



(d)

Figure 4.23: Distribution of local shear rate and dispersive mixing index for the three screw configurations at 100RPM calculated for points on 100 random particle trajectories at XY cross-sectional planes at P1, P4 and P8 (a) FLAT P1 (b) 45F P1 (c) 45R P1 (d) Distribution of density of points $\lambda_{MZ} > 0.6$ in the three paddle element configurations at 100RPM for points on 100 random particle trajectories at XY cross-sectional planes at P1, P4 and P8.

4.3.2 Experimental investigation of bubble breakup

In the first part of the preliminary experiments we used high speed images captured at a frame rate of 1000 frames/sec to demonstrate the elongation and breakup of bubbles in the twin screw mixer flow. Figures 4.24 (a) to (d) are images of bubbles at various positions during mixing of the corn syrup. It can be seen that the deformation (L/a) for the larger bubbles is quite large consistent with the slender body shapes needed for breakup in low viscosity ratio flows. The apparent deformation decreases for smaller bubble sizes whose shapes are near ellipsoidal thus suggesting the existence of a stable deformation for bubbles below a critical diameter.

\

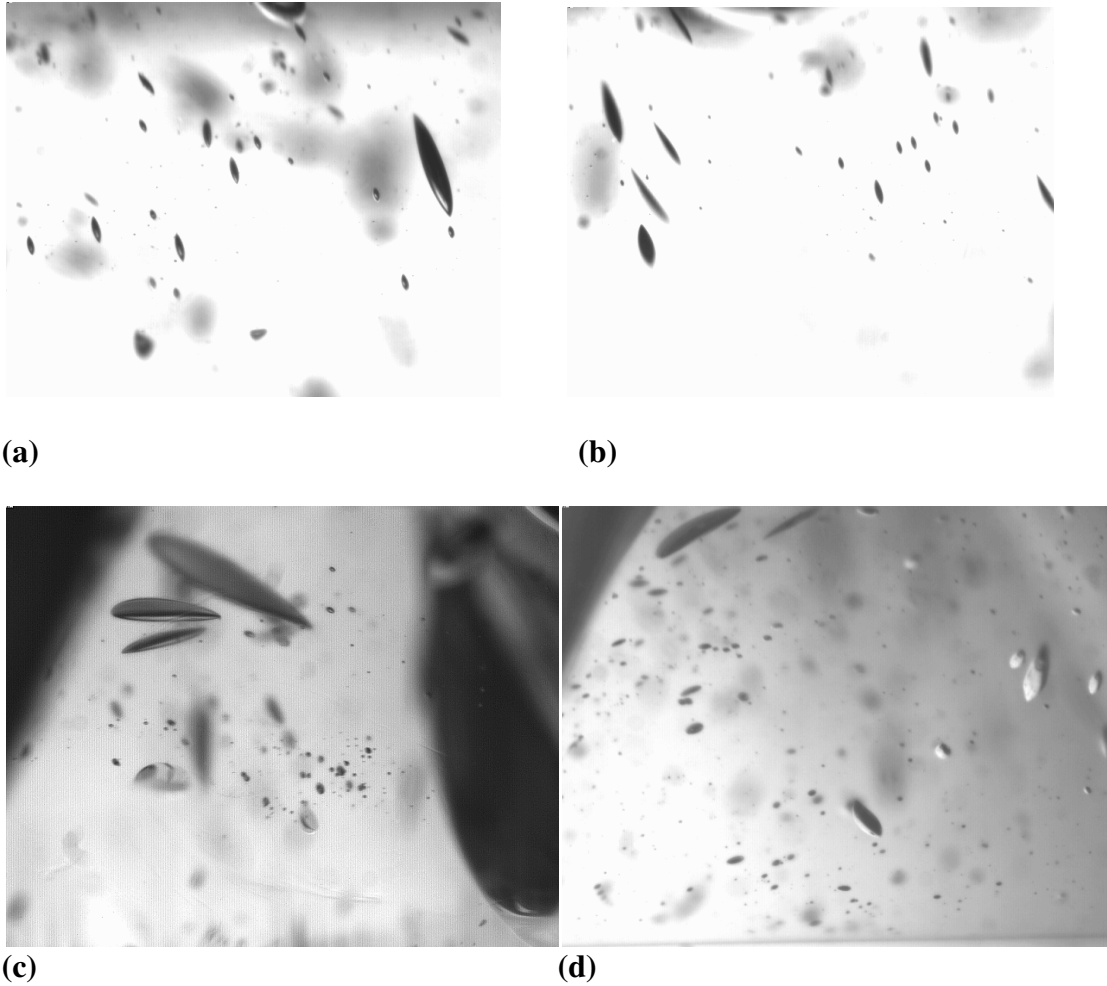
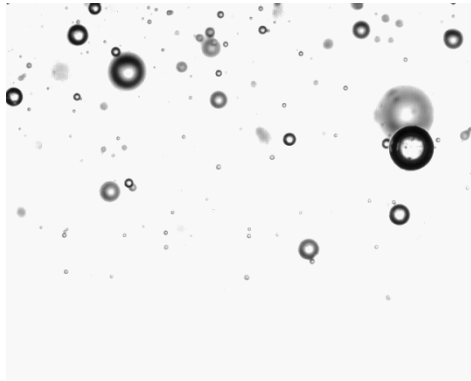


Figure 4.24 High speed images of bubbles at various locations in the mixer during mixing at (a), (b) 100 RPM and (c), (d) 55 RPM at the P4 and feed screw locations.

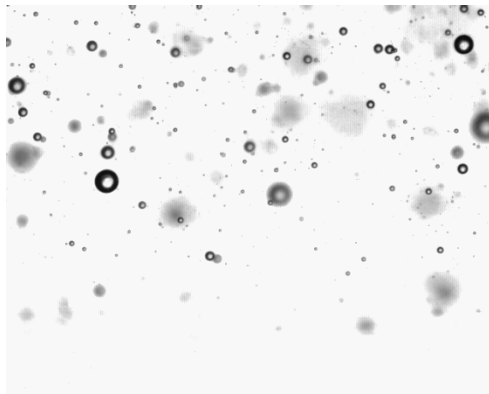
Figure 4.25 shows images of the bubbles soon after the rotation of the mixer was stopped. We can see chains of broken bubbles resulting from capillary breakup of unsteadily deformed larger bubbles while those below a maximum stable diameter show relax back to a spherical shape.



(a)



(b)



(c)

Figure 4.25 Bubble images taken along the mixer length for FLAT configuration (a) P4 at 100 RPM (b) P4 at 55 RPM taken while the mixer was running and (c) P1 at 100 RPM (b) P4 at 100 RPM and (c) P8 at 100 RPM taken after the mixer was stopped.

Figure 4.26a shows a comparison of the measured bubble size distribution curves for the three paddle element configurations at 100 RPM. The bubble size data was fit to normal distribution for FLAT, 45F and 45R configurations using the statistics tool box in MATLAB. The distribution parameters are given in Table 4.4 and show the mean of means and the standard deviation of the means for each set of distributions and show

good reproducibility, except for one data set (45F), which could have been due to experimental error. Figure 9 shows the confidence bounds for the cumulative distribution functions at 95% confidence level are at an acceptable range for the distributions obtained on different days. The distributions obtained on different days showed good reproducibility with the FLAT and 45R configurations showing narrower distributions (increased breakup) compared to the 45F configuration. The lower breakup observed in the 45F configuration could be due to the lower density of elongation flow experienced by particles travelling long the mixer length as shown in figure 4.23. In the 45R and 45F configurations, the stagger in the middle of the mixing region disrupts the squeeze flow effect (Vyakaranam and Kokini, 2012). Bubble size distributions were also measured inside the mixer at screw speeds of 55 and 100 RPM. Figures 4.26b and 4.26c show the size distributions at the beginning (location P1) and end (location P8) of the mixing region for the FLAT configuration at 55 and 100 RPM respectively. At 100 RPM, the size distributions narrowed significantly going from location P1 to location P8 due to breakup of the larger bubbles with a diameter $> 300 \mu\text{m}$. At the lower screw speed of 55 RPM bubble breakup was not significant going from location P1 to location P8. This could be due to the fact that the Ca values for the smallest bubbles ($< 300 \mu\text{m}$) are not high enough to reach the critical value in the mixed to predominantly elongation flows as shown in figure 4.22.

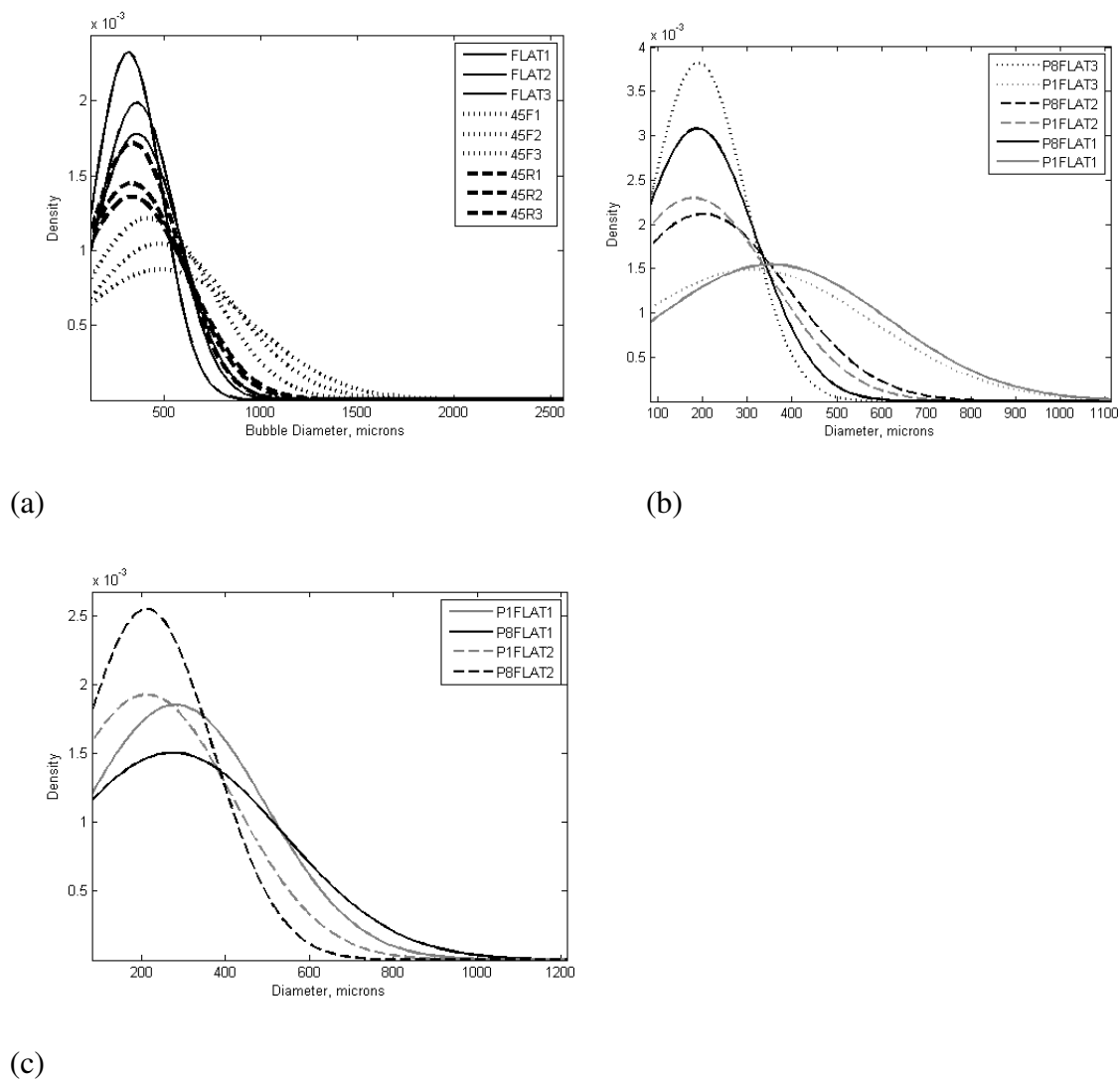


Figure 4.26 Bubble size distributions taken (a) outside the mixer for the three paddle element configurations at 100 RPM; (b) at P1 and P8 inside the mixer at 100 RPM; (c) at P1 and P8 inside the mixer at 55 RPM.

Inside Mixer			Outside Mixer		
	P1	P8	FLAT	45F	45R
Mean	281.261	193.539		461.869	336.649
	3	3	347.171	7	3
	90.6238		25.1438	36.2645	4.05333
St. Dev.	7	6.27207	1	9	7
%	32.2205	3.24072	7.24248	7.85169	1.20402
St.Dev.	2	1	4	4	4

Table 4.4 Distribution parameters for normal distribution fits in Figure 4.26.

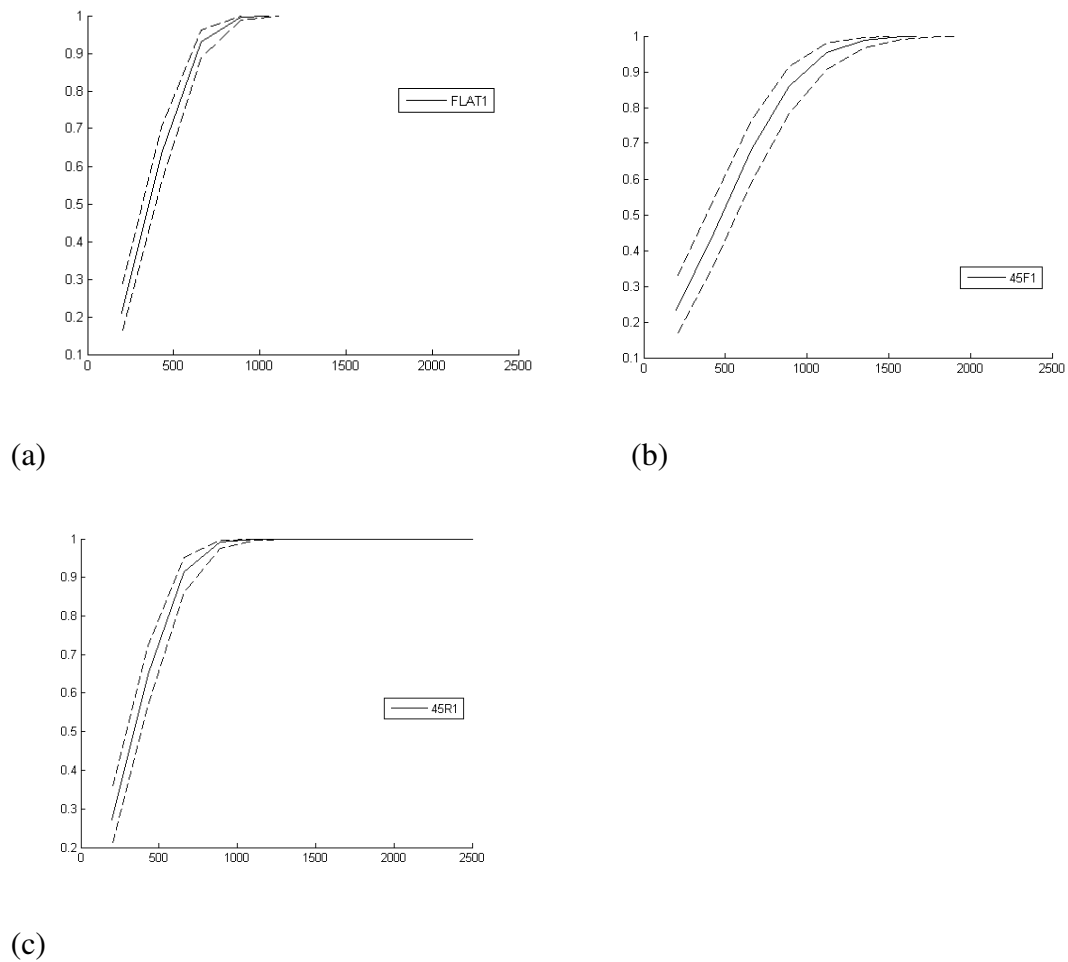


Figure 4.27 Confidence bounds at 95% level for the normal distribution fits outside the mixer for (a) FLAT (b) 45F and (c) 45R paddle element configurations.

4.3.3 Evaluation of maximum stable diameter and effective shear rate for dispersion

Figure 4.28 shows the distribution of d_{max} at 100 RPM over XY cross-sections at three different locations in the mixer – P1, P4 and P8. For all the locations and paddle configurations the distributions show an approximate maximum limit at 300 μm implying all bubbles over this limit will be subject to breakup. The FLAT and 45R configurations showed similar distributions at all locations. The distributions of bubbles in the 45F configuration had significantly larger spread, indicating an increased area with larger stable bubble diameters compared to the FLAT and 45R configurations.

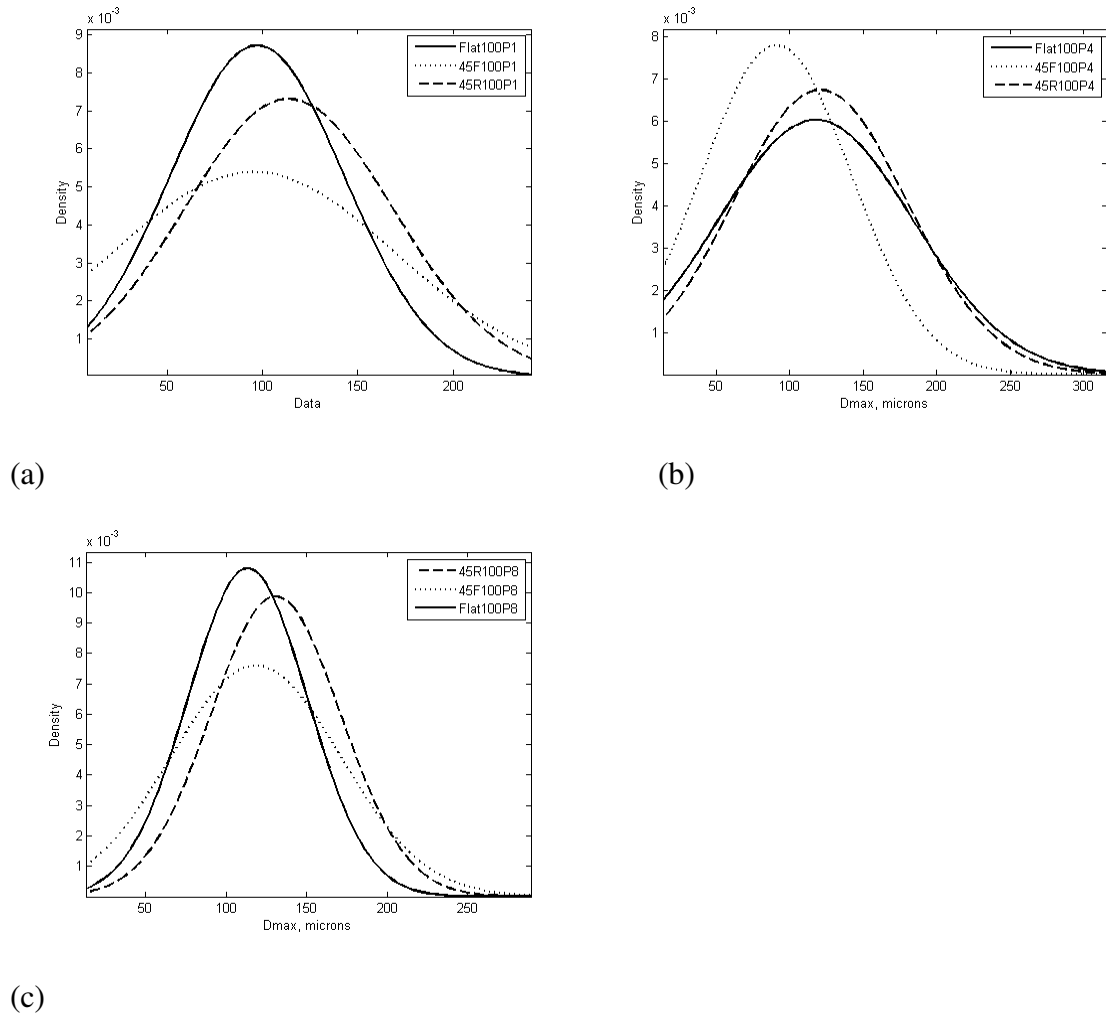


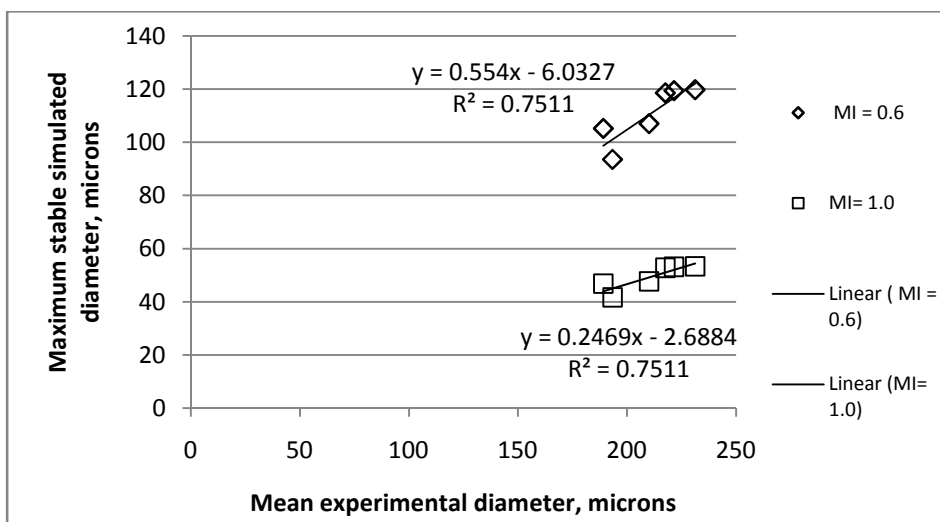
Figure 4.28 Distribution of theoretical maximum stable diameter, d_{max} over points on trajectories on XY cross-sectional planes at the beginning (P1) and end (P8) of the mixing region for three paddle configurations at 100 RPM

Figure 4.29 shows the mean bubble diameters (d_{mean}) measured at the beginning and the end of the mixing region for the three configurations plotted against the maximum stable diameters (d_{max}) predicted by the FEM simulations at a screw speed of 100 RPM. The maximum stable diameters were calculated from equation 3.2 using the simulated average values of the shear rate at beginning (P1) and the end (P8) of the

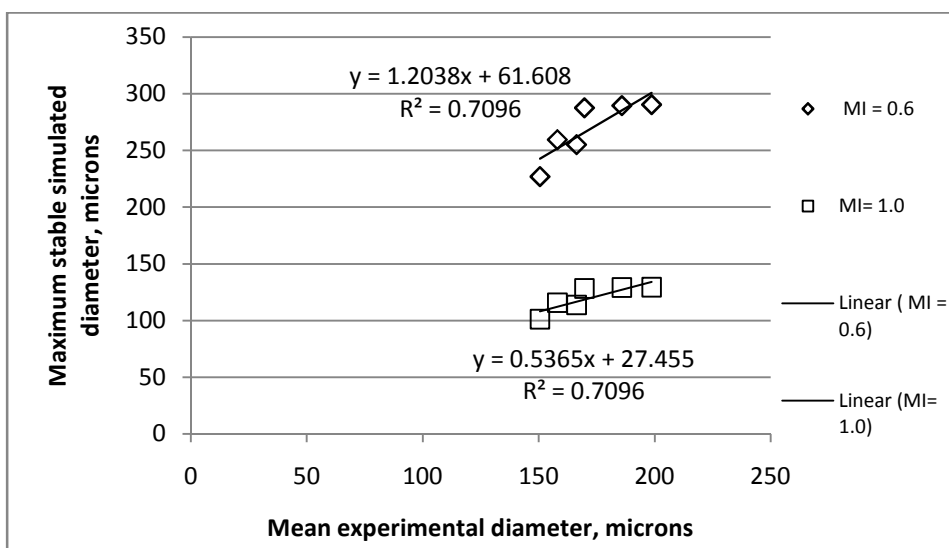
mixing region for the three paddle configurations. The maximum stable diameters were estimated for two flow types, with λ_{MZ} of 1.0 (predominantly elongation) and 0.6 (mixed shear and elongation). The predicted maximum stable diameters were approximately half of the experimentally measured mean diameters assuming a λ_{MZ} of 0.6 while an assumption of predominantly elongation flow ($\lambda_{MZ} = 1.0$) predicted even lower diameters than those observed. It should be noted that the simulation predicts the ‘maximum’ stable diameters while the experimentally measured diameters are the mean of the size distributions at each location in the mixer. Hence the gap in the magnitudes is likely a result of the fact that at the right conditions (flow type and flow strength) the breakup process is dynamic and while the average diameter of the distribution is a good indicator of the changing distributions, it is not an exact representation of the maximum stable diameter in magnitude.

Additionally, for the measured mean diameters (d_{mean}) of the bubble size distribution in the mixer, an effective shear rate G_{eff} was estimated from equation 1.6. Figure 4.30 shows the effective shear rate for breakup calculated at the various locations in the mixer using the experimentally measured bubble diameters plotted against the mean shear rate values (G_{mean}) over XY cross-sections (P1 and P8) predicted by the simulation for screw speeds of 55 and 100 RPM. The effective shear rates were calculated based on a dispersive mixing index of 0.6 and the corresponding value of the Ca_{cr} obtained from equation 3.1. Average shear rates calculated over the entire length of three random particle trajectories are also shown for comparison. The effective shear rate for breakup was proportional to the local mean shear rates predicted by the simulation at both the screw speeds. The magnitudes of the effective shear rates were approximately

half the magnitude of the simulated mean shear rates for 100 RPM and approximately double the simulated shear rates for 55 RPM. This result explains the increased dispersion at 100 RPM where the breakup of larger bubbles in the distribution is caused by the additional shear rate that is in excess to that required to achieve the mean diameter of the distribution where as at 55 RPM, the shear rate is not high enough to break up the larger bubbles. The mean shear rates calculated over the lengths of three particle trajectories were closer to the effective shear rate values, although enough trajectories could not be evaluated for a correlation due to the time required to evaluate individual data points.

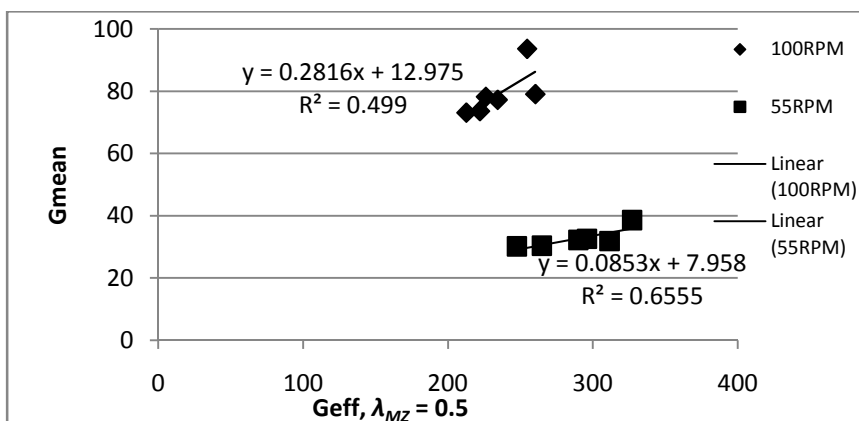


(a)

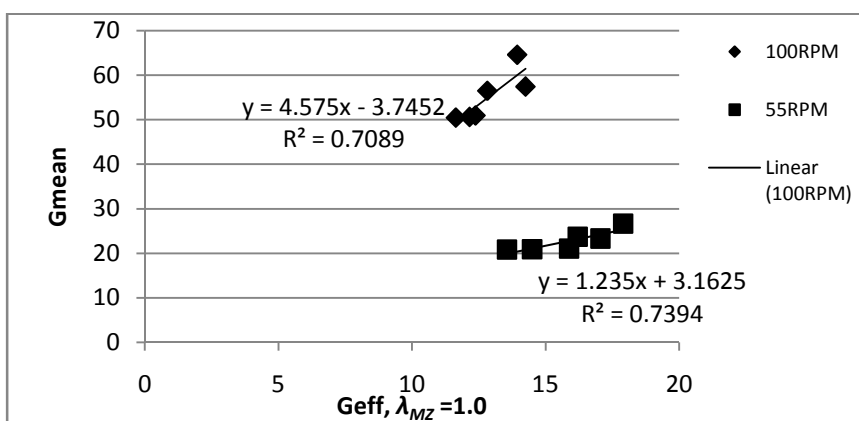


(b)

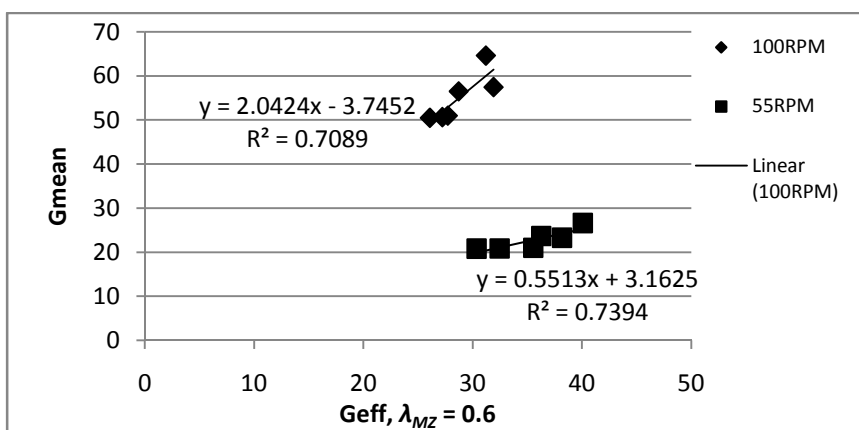
Figure 4.29 Comparison of mean experimental bubble diameters vs. simulated maximum stable bubble diameters for all the paddle configurations as a function of dispersive mixing index.(a) 100 RPM (b) 55 RPM



(a)



(b)



(c)

Figure 4.30 Comparison of effective shear rate vs. simulated mean shear rates for all the paddle configurations as a function of screw speed.

5. CONCLUSIONS

3D FEM simulations were used to study the effect of stagger angle on the flow profile in a Readco 2" continuous processor. The analysis of velocity profiles shows that an introduction of stagger (forward or reverse) in a limited region of the mixing region can only create local disruptions in overall flow and not enough to create an overall forward or reverse flow. This is especially owing to the fact that a constant flow is imposed at the inlet boundary plane of the mixing region in the simulation.

Paddle element stagger primarily caused variations in the local axial velocity (V_z) values while local V_x and V_y remained largely unaffected. The local variations in velocities also depend on the specific time step (or paddle rotation) implying that flow information must be analyzed at all dissimilar angular positions of the paddle elements after accounting for geometrical symmetry. The material flow in the FLAT configuration is mostly unobstructed and hence shows a greater axial velocity increase along the axis whereas the stagger causes obstruction to the axial flow in specific regions, depending on the type and location of the stagger.

Local pressure profiles showed greater pressure values in the intermeshing region of the FLAT configuration, suggesting the material is squeezed into and out of the region. The overall axial transport in the FLAT configuration happened through the C-shaped region between the paddle elements and the barrel wall while in the forward 45F configuration, the axial transport of the material was mostly through the intermeshing region between the co-rotating paddle elements. In case of the reverse 45R configuration, significant local backflow regions were seen in the intermeshing region which also

resulted in the axial flow happening through the C-shaped region between the paddle elements and the barrel wall. There was no significant variation of for pressure in the axial direction for both the staggered configurations suggesting a conveying/leakage mechanism for axial transport. The specific location of the local variations in axial flow is of significance to further analysis of local and overall dispersive and distributive mixing indices. The location and length of the staggered region could affect the distribution and intensity of increased local forward and backward flow. In our simulation, the staggered region constituted only 1/3 of the entire mixing region and additionally was in the middle of two equal length non-staggered regions. It would be interesting to see the effect of the length of the staggered region and also the location in relation to presence of non-staggered regions.

3D Finite Element Method simulations were used to investigate dispersive mixing flow of a viscous Newtonian model fluid in the kneading block region of the Readco® continuous twin-screw mixer. The variation in the local shear rate and dispersive mixing index values were studied as a function of paddle element stagger, radial and axial locations in the mixer barrel. The average values of the shear rate and the dispersive mixing index λ_{MZ} calculated over all points in the barrel volume were found to be independent of the paddle configuration. The flow in the barrel volume was found to be predominantly simple shear flow with an average value of λ_{MZ} around 0.5 as reported in previous studies of twin-screw extruders. Average value of shear rate calculated for points with an elongation flow character ($\lambda_{MZ} > 0.6$) was significantly higher for the FLAT configuration compared to the staggered configurations indicating better dispersive mixing. Contour maps of shear rate over local X-Y cross-sections revealed

three regions of shear rate distribution with the majority of the fluid being in the average shear rate range. The highest shear rates were found in the nip regions between the tip of the paddle elements and the barrel surface consistent with other studies (Bakalis and Karwe, 2002), while the intermeshing region between the two paddle elements above and below the nip region of the tips also showed high values of shear rate. This trend was largely independent of the paddle element stagger. A three region categorization was also evident in the distribution of dispersive mixing index, with the highest values occurring in the intermeshing region. The majority of the fluid showed a predominantly simple shear type of flow, pure rotation or plug flow was limited to the regions lining the rotating paddle element surfaces. The combined higher values of shear rate and dispersive mixing index suggested the importance of the intermeshing region for dispersive mixing ability.

The elongational flow in the intermeshing region occurred as a result of an apparent squeeze flow created between the moving paddle element surfaces and the barrel surface, similar to that between counter rotating four roll mills causing a predominantly elongational flow. The introduction of stagger disrupted this effect in the region of the stagger where elongational flow intensity was minimal in the intermeshing region. The overall elongation flow intensity was lower in the 45F configuration compared to the FLAT and 45R configurations. The axial transport in the FLAT and 45R configurations appears to have happened predominantly through the C-shaped region between the paddle elements and the barrel wall while in the forward 45F configuration, the axial transport of the material was mostly through the intermeshing region between the co-rotating paddle elements, as shown previously.

The specific location of the local variations in shear rates and flow type is of significance to designing mixers with better dispersive mixing ability. The location and extent of the staggered region affects the distribution and intensity of dispersive mixing flow. Bubble dispersion during mixing of a viscous Newtonian liquid was studied using experimentally measurements and 3D FEM simulations of dispersive mixing in a Readco[®] twin-screw continuous processor. Critical capillary numbers calculated from previously established correlations for flow types between simple shear and pure elongation flows for the Newtonian fluid- air system showed that at the shear rates present in mixer, bubble breakup was possible only in flows with a higher elongation character than shear i.e., flows with a dispersive mixing index (or flow type), $\lambda_{MZ} > 0.6$. Experimentally measured bubble size distributions showed a variation with both paddle element stagger and screw speed. The density of dispersive mixing index (or flow type) that is conducive for bubble breakup varied with the paddle element stagger, with the no-stagger FLAT configuration showing the highest density of elongation flow ($\lambda_{MZ} > 0.6$) and the forward conveying 45F configuration showing the least. The measured bubble size distributions showed highest breakup for the FLAT configuration, due to higher incidence of elongation flow in this configuration while the reverse was true for the 45F configuration. A maximum stable bubble diameter predicted from local shear rates calculated from the FEM simulations in the mixer correlated well with the experimental mean bubble diameters, however with a difference in magnitude. Effective shear rates back calculated from measured mean bubble diameters were proportional to the mean shear rates calculated by the FEM simulations at various locations in the mixer for the three paddle element configurations. At 100 RPM, the mean shear rates were found to be

double of what was required to achieve the mean diameters, while at 55 RPM, the mean shear rates were lower than what was required to achieve the mean diameters. In this study we have developed a method to predict the effective shear rate for dispersion of air during continuous mixing of a Newtonian liquid.

6. REFERENCES

- A. Acrivos, "The breakup of small drops and bubbles in shear flows", *Annals of New York Acadamey of Sciences* **404** (1983) (1).
- A. Acrivos and T.S. Lo, "Deformation and breakup of a single slender drop in an extensional flow", *Journal of Fluid Mechanics* **86** (1978) (4), p. 641.
- M.M., Alvarez-Hernández, T. Shinbrot, J.Zalc., F.J.Muzzio "Practical chaotic mixing." *Chemical Engineering Science* **57** (2002) (17) p 3749-3753.
- B.K.Ashokan, "Developing methods for design and analysis of continuous mixers through 3D numerical simulation of flow and mixing". *PhD Thesis*, Rutgers University. (2008).
- S.Bakalis and M.V.Karwe "Velocity distributions and volume flow rates in the nip and translational regions of a co-rotating, self-wiping, twin-screw extruder" *Journal of Food Engineering* **51** (2002) 4 p. 273-282.
- F.Barailler, M. Heniche, and P.A. Tanguy "CFD analysis of a rotor-stator mixer with viscous fluids." *Chemical Engineering Science* **61**(2006) (9) p 2888-2894.
- A.H. Barrett and M. Peleg, "Extrudate cell structure - texture relationships", *Journal of Food Science* **57** (1992) (5), p. 1253.
- D. Barthes-Biesel and A. Acrivos, "Deformation and burst of a liquid droplet freely suspended in a linear shear field", *Journal of Fluid Mechanics* **61** (1973) (1), p. 1.
- B.J. Bentley and L.G. Leal, "An experimental investigation of drop deformation in steady, two-dimensional linear flows", *Journal of Fluid Mechanics* **167** (1986), p. 241.
- M. Blander and J.L. Katz, "Bubble nucleation in liquids", *AIChE Journal* **21** (1975) (5), p. 833.
- A.H. Bloksma, "Rheology of the breadmaking process", *Cereal Foods World* **35** (1990) (2), p. 228.
- A. Borhan and J.Pallinti, 'Breakup of drops and bubbles translating through cylindrical capillaries', *Physics of Fluids*, **11** (1999) (10). p. 2846
- G.M. Campbell, C.D. Reilly, P.J. Fryer and P.A. Sadd, "Aeration of bread dough during mixing: effect of mixing dough at reduced pressure", *Cereal Foods World* **43** (1998) (3), p. 163.
- G.M. Campbell and P. Shah, In: G.M. Campbell, C. Webb, S.S. Pandiela and K. Niranjana, Editors, *Bubbles in Food*, AACC Press, St.Paul (1998), pp. 11-20.

E.L. Canedo, M. Favelukis, Z. Tadmor and Y. Talmon, "An experimental study of bubble deformation in viscous liquids in simple shear flow", *AIChE Journal* **39** (1993) (4), p. 553.

C.N. Chang, Study of the mechanism of starchy biopolymer extrudate, *Department of Food Science*, Rutgers University, New Brunswick (1992), p. 291.

H. Cheng and I. Manas - Zloczower, "Chaotic Features of Flow in Polymer Processing Equipment-Relevance to Distributive Mixing", *International Polymer Processing* **12** (1997) (2), p. 83.

F.H. Cisneros, Air bubble nucleation during starch extrusion, *Department of Food Science*, Rutgers University, New Brunswick (1998), p. 298.

F.H. Cisneros and J.L. Kokini, "Effect of extrusion operating parameters on air bubble entrapment", *Journal of Food Process Engineering* **25** (2002) (4), p. 251.

F.H. Cisneros and J.L. Kokini, "A generalized theory linking barrel fill length and air bubble entrapment during extrusion of starch", *Journal of Food Engineering* **51** (2002) (2), p. 139.

J.S. Colton and N.P. Suh, "Nucleation of microcellular foam: theory and practice", *Polymer Engineering and Science* **27** (1987) (7), p. 500.

R.K. Connelly and J.L. Kokini, "2-D numerical simulation of differential viscoelastic fluids in a single-screw continuous mixer: Application of viscoelastic finite element methods", *Advances in Polymer Technology* **22** (2003) (1), p. 22.

R.K. Connelly and J.L. Kokini, "3D numerical simulation of the flow of viscous Newtonian and shear thinning fluids in a twin sigma blade mixer", *Advances in Polymer Technology* **25** (2006) (3), p. 182.

R.K. Connelly and J.L. Kokini, "The effect of shear thinning and differential viscoelasticity on mixing in a model 2D mixer as determined using FEM with particle tracking", *Journal of Non-Newtonian Fluid Mechanics* **123** (2004) (1), p. 1.

R.K. Connelly and J.L. Kokini, "Examination of the mixing ability of single and twin screw mixers using 2D finite element method simulation with particle tracking", *Journal of Food Engineering* **79** (2007) (3), p. 956.

R.K. Connelly and J.L. Kokini, "Mixing simulation of a viscous newtonian liquid in a twin sigma blade mixer", *AIChE Journal* **52** (2006) (10), p. 3383.

P.K. Das, J. Legrand, P. Morancais and G. Carnelle, "Drop breakage model in static mixers at low and intermediate Reynolds number", *Chemical Engineering Science* **60** (2005) (1), p. 231.

M. Dhanasekharan and J.L. Kokini, "Design and scaling of wheat dough extrusion by numerical simulation of flow and heat transfer", *Journal of Food Engineering* **60** (2003) (4), p. 421.

M. Dhanasekharan and J.L. Kokini, "Viscoelastic flow modeling in the extrusion of a dough-like fluid", *Journal of Food Process Engineering* **23** (2000) (3), p. 237.

H. Dogan and J.L. Kokini, "Psychophysical markers for crispness and influence of phase behavior and structure", *Journal of Texture Studies* **38** (2006) (3), p. 324.

A.-C. Eliasson and K. Larsson, *Cereals in breadmaking: a molecular colloidal approach*, Marcel Dekker, Inc., New York (1993).

M. Favelukis, O.M. Lavrenteva and A. Nir, "Deformation and breakup of a non-Newtonian slender drop in an extensional flow", *Journal on Non-Newtonian Fluid Mechanics* **125** (2005) (1), p. 49.

R.W. Foster and J.T. Lindt, "Twin screw extrusion devolatilization: from foam to bubble free mass transfer", *Polymer Engineering and Science* **30** (1990) (11), p. 621.

H.P. Grace, "Dispersion phenomena in high viscosity immiscible fluid systems and application of static mixers as dispersion devices in such systems", *Chemical Engineering Communications* **14** (1982), p. 225.

R.C.E. Guy and A.W. Horne, In: J.M.V. Blanshard and J.R. Mitchell, Editors, *Food structure - its creation and evaluation*, Butterworth, London (1988), pp. 331-350.

E.J. Hinch and A. Acrivos, "Long slender drops in a simple shear flow", *Journal of Fluid Mechanics* **98** (1980) (2), p. 305.

E.J. Hinch and A.A. Acrivos, "Steady long slender droplets in two-dimensional straining motion", *Journal of Fluid Mechanics* **91** (1979) (3), p. 401.

R.C. Hosney, "The mixing phenomena", *Cereal Foods World* **30** (1985) (7), p. 453.

H. Huang and J.L. Kokini, In: G.M. Campbell, C. Webb, S.S. Pandiela and K. Niranjan, Editors, *Bubbles in Food*, AACC Press, St. Paul (1998), pp. 113-120.

M. Heniche and P.A. Tanguy "Finite Element Modeling of Viscous Mixing: A Review." *Chemical Product and Process Modeling* **3** (2008) (1) p 1934-2659.

M. Heniche, P. A. Tanguy, M.F. Reeder, and J.B. Fasano "Numerical investigation of blade shape in static mixing." *AIChE Journal* **51** (2005) (1) p 44-58.

- A.Iranshahi, C. Devals, M.Heniche, L.Fradette, P.A.Tanguy, K.Takenaka "Hydrodynamics characterization of the Maxblend impeller" *Chemical Engineering Science* **62**(2007) (14) p 3641-3653.
- A.Iranshahi, M. Heniche, F.Bertrand, P.A.Tanguy "Numerical investigation of the mixing efficiency of the Ekato Paravisc impeller" *Chemical Engineering Science* **61**(2006) (8) p 2609-2617.
- T.Ishikawa, S.-I. Kihara, K. Funatsu "3-D non-isothermal flow field analysis and mixing performance evaluation of kneading blocks in a co-rotating twin screw extruder." *Polymer Engineering and Science* **41**(2001) (5)p 840-849.
- D.V. Khakhar and J.M. Ottino,"Deformation and breakup of slender drops in linear flows", *Journal of Fluid Mechanics* **166** (1986), p. 265.
- J.L. Kokini, C.N. Chang and L.S. Lai, In: J.L. Kokini, C.T. Ho and M. Karwe, Editors, *Food extrusion science and technology*, Marcel Dekker, Inc., New York (1992), pp. 631-652.
- T. Li and I. Manas - Zloczower,"Flow field analysis of an intermeshing counterrotating twin screw extruder", *Polymer Engineering and Science* **34** (1994) (7), p. 551.
- T. Li and I. Manas - Zloczower,"Temporal distributions: The basis for the development of mixing indexes for scale-up of polymer processing equipment", *Chemical Engineering Communications* **139** (1995), p. 223.
- F. MacRitchie, In: J.M.V. Blanshard, P.J. Frazier and T. Gaillard, Editors, *Chemistry and physics of baking: materials, processes and products*, Royal Society of Chemistry, London (1986), pp. 132-146.
- M.E.H. Meijer and J.M.H. Janssen, In: I. Manas - Zloczower and Z. Tadmor, Editors, *Mixing and compounding of polymers: theory and practice*, Carl Hanser Verlag, New York (1994).
- F. J.Muzzio, M. M. Alvarez, S.Cerbelli, M.Giona, and A.Adrover "The intermaterial area density generated by time- and spatially periodic 2D chaotic flows" *Chemical Engineering Science* **55**(2000) (8):1497-1508.
- J.M.Ottino "The kinematics of mixing:stretching,chaos and transport"(1989) .Cambridge, Press Syndicate of University of Cambridge.
- S. Prakash, Characterization of shear rate distribution in a model mixer using laser doppler anemometry, *Department of Food Science*, Rutgers University, New Brunswick (1996), p. 315.

- S. Prakash, M. Karwe and J.L. Kokini, "Measurement of velocity distribution in the Brabender Farinograph as a model mixer, using Laser-Doppler Anemometry", *Journal of Food Process Engineering* **22** (1999) (6), p. 435.
- S. Prakash and J.L. Kokini, "Determination of mixing efficiency in a model food mixer", *Advances in Polymer Technology* **18** (1999) (3), p. 209.
- S. Prakash and J.L. Kokini, "Estimation and prediction of shear rate distribution as a model mixer", *Journal of Food Engineering* **44** (2000) (3), p. 135.
- D.Rauline, J. M. Le Blévec, J.Bousquet, and P.A.Tanguy "A comparative assessment of the performance of the Kenics and SMX static mixers" *Chemical Engineering Research and Design* **78** (2000) (3): 389-396.
- C.Rivera, M.Heniche, G.Ascanio, P.Tanguy "A Virtual Finite Element Model for Centered and Eccentric Mixer Configurations" *Computers & Chemical Engineering*, **28** (2004) (12), p. 2459-2468.
- C.Rivera, S. Foucault, M.Heniche, T.Espinosa-Solares, and P.A.Tanguy "Mixing analysis in a coaxial mixer." *Chemical Engineering Science* **61** (2006) (9) p 2895-2907.
- J.N.Reddy "An introduction to the finite element method." (2006). .New Delhi, Tata McGraw-Hill..Jongen, T "Characterization of batch mixers using numerical flow simulations" *AIChE Journal* **46** (2000) (11)p 2140-2150.
- T. R. G. Jongen, M. V. Bruschke, and J.G.Dekker "Analysis of dough kneaders using numerical flow simulations" *Cereal Chemistry* **80** (2003) (4)p 383-389.
- F. Risso, "The mechanisms of deformation and breakup of drops and bubbles", *Multiphase Science and Technology* **12** (2000), p. 1.
- A.C. Rust and M. Manga, "Bubble shapes and orientations on low Re simple shear flow", *Journal of Colloid and Interface Science* **249** (2002), p. 476.
- G.I. Taylor, "Disintegration of water drops in an electric field", *Proceedings of The Royal Society of London A* **280** (1964) (1382), p. 383.
- G.I. Taylor, "The formation of emulsions in definable fields of flow", *Proceedings of The Royal Society of London. Series A, Containing Papers of a Mathematical and Physical Character* **146** (1934) (858), p. 501.
- G.I. Taylor, "The viscosity of a fluid containing small drops of another fluid", *Proceedings of The Royal Society of London. Series A, Containing Papers of a Mathematical and Physical Character* **138** (1932) (834), p. 41.

K.V.Vyakaranam, B.K.Ashokan, and Kokini, J.L. Evaluation of effect of paddle element stagger angle on the local velocity profiles in a twin-screw continuous mixer with viscous flow using Finite Element Method simulations, *Journal of Food Engineering*, **108** (2012) (4) P. 585-599

K.V.Vyakaranam and Kokini, J.L. "Advances in 3D numerical simulation of viscous and viscoelastic flows for mixing", in *Food Engineering Interfaces*, Aguilera, J.M.; Simpson, R.; Welti-Chanes, J.; Bermudez-Aguirre, D.; Barbosa-Canovas, G. (Eds.), Springer, 2011.

W. Wang and I. Manas - Zloczower, "Temporal distributions: The basis for the development of mixing indexes for scale-up of polymer processing equipment", *Polymer Engineering and Science* **41** (2001) (6), p. 1068-1077.

H.H. Yang and I. Manas - Zloczower, Flow simulations in the kneading discs region of a co-rotating twin screw extruder, Science and Engineering on Supercomputers. Proceedings of the Fifth International Conference (1990), pp. 273-284.

H.H. Yang and I. Manas - Zloczower, "3d Flow field analysis of a Banbury mixer", *Proceedings of the International Congress on Rheology* (1992), p. 408.

M.Yoshinaga, S.Katsuki, M.Miyazaki, L.Liu, S-I Kihara, and K.Funatsu "Mixing mechanism of three-tip kneading block in twin screw extruders." *Polymer Engineering and Science* **40** (2000) (1): 168-178.

J.M. Zalc, M. M. Alvarez, F.J.Muzzio, and B.E. Arik "Extensive validation of computed laminar flow in a stirred tank with three Rushton turbines" *AIChE Journal* **47**(2001)(10) p. 2144-2154.

J.M. Zalc, E. S. Szalai, M. M. Alvarez, and F.J.Muzzio "Using CFD to understand chaotic mixing in laminar stirred tanks" *AIChE Journal* **48** (2002) (10) p. 2124-2134.

J.M. Zalc, E. S. Szalai, and F.J.Muzzio. "Mixing dynamics in the SMX static mixer as a function of injection location and flow ratio" *Polymer Engineering and Science* **43** (2003) (4) p 875-890.

J.M. Zalc, E. S. Szalai, F.J.Muzzio and S.Jaffer. "Characterization of flow and mixing in an SMX static mixer" *AIChE Journal* **48** (2002) (3) p. 427-436.

APPENDIX

SUPPLEMENTAL DATA FILES

Data file 1: Viscosity and density of Corn Syrup

Data file 2: Mass flow rate measurements (Figure 4.1)

Data file 3: Experimental Bubble Size Data – Outside Mixer (Figure 4.26)

Data file 4: Experimental Bubble Size Data – Inside Mixer (Figure 4.26)

Data file 5: Mixing Index and Shear Rate Data – XY Cross-Sections (Figure 4.21)

Data file 6: Mixing Index and Shear Rate Data – Trajectory Slices (Figure 4.23)

Data file 7: Mean bubble diameters and Effective Shear Rate Data (Figure 4.28, 4.29)

VITA

KIRAN V. VYAKARANAM

EDUCATION

- | | |
|-----------|--|
| 1999-2003 | Bachelors of Technology, Food Technology
College of Technology, Osmania University, India |
| 2003-2012 | Ph.D., Food Science
Rutgers University, NJ, USA |

EXPERIENCE

- | | |
|--------------|---|
| 2004-2006 | Graduate Research Assistant, Department of Food Science
Rutgers University, NJ, USA |
| 2009 | Intern, Gum Innovation Product Development
Cadbury Adams USA, Whippany, NJ, USA |
| 2009-2010 | Senior Associate Scientist, Ingredient Technology
Cadbury Adams USA, Whippany, NJ, USA |
| 2011-current | Associate Scientist II, Ingredient Technology
Kraft Foods Inc., Whippany, NJ, USA |

PUBLICATIONS

Vyakaranam, K.V. and Kokini, J.L. Prediction of air bubble dispersion in a viscous fluid in twin screw continuous mixer using FEM simulations of dispersive mixing, 2012. Chemical Engineering Science (under review)

Vyakaranam, K.V., Ashokan, B.K., and Kokini, J.L. Evaluation of effect of paddle element stagger angle on the local velocity profiles in a twin-screw continuous mixer with viscous flow using Finite Element Method simulations, Journal of Food Engineering, 2012. 108 (4): 585-599

Vyakaranam, K.V., and Kokini, J.L. Advances in 3D numerical simulation of viscous and viscoelastic flows for mixing, in *Food Engineering Interfaces*, Aguilera, J.M.; Simpson, R.; Welti-Chanes, J.; Bermudez-Aguirre, D.; Barbosa-Canovas, G. (Eds.), Springer, 2011

Vyakaranam, K.V., Evans, M.E., Ashokan, B.K. and Kokini, J.L. Evaluation of mixing and air bubble dispersion in viscous liquids using numerical simulations, in *Food Mixing: Principles and Applications*, Cullen, P.J. (Ed.), Blackwell Publishing, 2009

Vyakaranam, K.V. and Kokini, J.L. Study of the dynamics and size distributions of air bubbles during mixing in a continuous food mixer, in *Bubbles in Food 2: Novelty, Health and Luxury*, Campbell, G., Scanlon, M. and Pyle, L. (Eds.), AACC Press, 2008